

APPLICATION OF THE ELECTRON NUCLEAR DYNAMICS
THEORY TO HYDROGEN ABSTRACTION AND EXCHANGE
REACTIONS OF $H + HOD$ AND $D_2 + NH_3^+$

By

MAURÍCIO D. COUTINHO NETO

A DISSERTATION PRESENTED TO THE GRADUATE SCHOOL
OF THE UNIVERSITY OF FLORIDA IN PARTIAL FULFILLMENT
OF THE REQUIREMENTS FOR THE DEGREE OF
DOCTOR OF PHILOSOPHY

UNIVERSITY OF FLORIDA

2001

ACKNOWLEDGMENTS

I would like to thank Drs. Y Öhrn and E. Deumens for their guidance, patience and relentless support over the many years I spend at QTP. I certainly enjoyed my time and developed an even greater appreciation for good science. I would also like to thank Prof. J. Broeckhove for helping with the calculations performed on *LiH* and *HF*.

During the time I spent at QTP I had the privilege to share time and office space with some wonderful and intelligent people. I would like to give special thanks to Anatol Blass, Magnus Hedström, Jorge Morales and Benny Mogensen for their friendship and support. I would also like to thank past and present members of the Öhrn/Deumens group for their camaraderie, friendship and help: Juan Oreiro, Denis Jacquemin, Remigio Cabrera-Trujillo, Ben Killian, David Masiello and Svetlana Malinovskaya. I also would like to thank several people outside the END group who made the environment at QTP such an enjoyable one, particularly staff members Judy Parker, Coralu Clements, Arlene Rodriguez and Cindy Leprell. I would like to thank past and present members of the Brazilian community in Gainesville that helped to create the Brazilian Student Association (BRASA): Fabiano Toni and Daniela Lopes, Uilson Lopes and Karina Gramacho, Dirceu and Patricia Mattos, Ricardo Matos, Eliana Kampf, Carlos da Costa, Ilka Vasconcelos, Francisco and Cleisa Cartaxo. I thoroughly enjoyed my extracurricular experiences with these people.

Life would not be the same without its little pleasures: I would like to thank Fabela, Vandinha and Juliet for their affection.

I can truly say that I would not be in science if not for the support, guidance and encouragement of my parents: Marício D. Coutinho Filho and Maria da Conceição D. P. de Lyra. I thank them sincerely. I would like to thank my dearest wife Fabíola for her love, support, caring and encouragement.

TABLE OF CONTENTS

	<u>page</u>
ACKNOWLEDGMENTS	ii
ABSTRACT	vii
CHAPTERS	
1 INTRODUCTION	1
1.1 Background Theory	5
1.1.1 Second Quantization	5
1.1.2 Diabatic, Adiabatic and END Representation	6
1.2 Solutions to the Time-Dependent Schrödinger Equation	15
1.2.1 Time-Dependent Close Coupling Method	16
1.2.2 Classical Path Method	16
1.2.3 Trajectory Surface Hopping Method	17
1.2.4 Car-Parrinello Method	18
1.2.5 Time-Dependent Hartree-Fock Based Methods	19
1.3 Electron Nuclear Dynamics (END) Method	20
1.3.1 Narrow Wavepacket Limit	24
1.3.2 Molecular Dynamics	24
1.4 Cross Sections Calculations	27
1.4.1 Differential Cross Section	27
1.4.2 Classical Collisions	29
1.4.3 Laboratory-Center of Mass Coordinate Transformation	32
1.4.4 Semiclassical Differential Cross Section	36
1.5 Measurements	40
1.5.1 Total Cross Section Calculation	41
1.5.2 Background on Guided Ion Beam Experiments	43
2 THE $NH_3^+ + D_2$ SYSTEM AT HYPERThERMAL ENERGIES	46
2.1 Introduction	46
2.2 Experimental Results for Reaction $NH_3^+ + D_2$	47
2.3 Computational Details	53
2.3.1 Structures at Extrema Points of the NH_3^+ Potential	53
2.3.2 Collision Grid and Initial Conditions	57
2.4 Results	60

2.4.1	Detailed Results for Collision at 6 eV	63
2.4.2	Detailed Results for Collision at 8 eV	66
2.4.3	Detailed Results for Collision at 12 eV	74
2.4.4	Detailed Results for Collision at 16 eV	78
2.5	Discussion	81
2.6	Conclusions	86
3	H+HOD COLLISION AT 1.575 EV.	89
3.1	Introduction:	89
3.2	Computational Details	92
3.3	Results	95
3.3.1	Results for <i>HOD</i> — Vibrational Ground State	99
3.3.2	Results for <i>HOD</i> (0,0,1) — OH Local Mode Excited	100
3.4	Improving the Basis Description	102
3.5	Conclusions	104
4	<i>LIH</i> AND <i>HF</i> DYNAMICS UNDER INTENSE FIELDS	105
4.1	Introduction	105
4.2	Theory	107
4.2.1	END with External Fields	107
4.2.2	Initial Conditions	109
4.3	Results and Discussion	111
4.3.1	Static Properties	111
4.3.2	Dynamics Results	113
4.3.3	Effect of the Basis Set	123
4.4	Conclusions	123
5	FINAL STATE ANALYSIS	129
5.1	Introduction	129
5.2	Background Theory	130
5.2.1	Unitary Transformations Using Basis Operators	130
5.2.2	Thouless Determinant	132
5.2.3	Basis Set Transformations	135
5.2.4	Final State Analysis	138
5.3	Simple Application	142
5.4	Implementation	144
5.4.1	Design	144
5.4.2	Algorithms	146
5.4.3	Numerical Examples	151
5.5	Conclusions	153

6 CONCLUSION	159
REFERENCES	162
BIOGRAPHICAL SKETCH	168

Abstract of Dissertation Presented to the Graduate School
of the University of Florida in Partial Fulfillment of the
Requirements for the Degree of Doctor of Philosophy

APPLICATION OF THE ELECTRON NUCLEAR DYNAMICS
THEORY TO HYDROGEN ABSTRACTION AND EXCHANGE
REACTIONS OF $H + HOD$ AND $D_2 + NH_3^+$

By

Maurício D. Coutinho Neto

December 2001

Chairman: Y. Öhrn

Major Department: Chemistry

The field of quantum molecular dynamics have flourished in the last 20 years. Methods that propose the solution of the time dependent Schrödinger equation for a molecular reactive process abound in the literature. However the majority of these methods focus on solving the nuclear Schrödinger equation subject to a known electronic potential. The electron nuclear dynamics (END) method proposes a framework of a hierarchy of approximations to the Schrödinger equation based on the time dependent variational Principle (TDVP). A general approach is sought to solve the electronic and nuclear problem simultaneously without making use of the Born-Oppenheimer approximation.

The purpose of this work is to apply the minimal END to areas where its unique qualities can give new insight into the relevant dynamics of a chemical or physical process. Minimal END is a method for direct non-adiabatic dynamics. It describes the electrons with a family of complex determinantal wave-functions in terms of non-orthogonal spin orbitals and treats the nuclei as classical particles.

In the first two studies, we apply the END method to hydrogen abstraction and exchange reactions at hyper-thermal collision energies. We investigate the $D_2 + NH_3^+$ reaction at collision energies ranging from 6 to 16 eV and the $H + HOD$ reaction at a collision energy of 1.575 eV. Collision energies refer to center of mass energies. Emphasis is put on the details of the abstraction and exchange reaction mechanisms for ground state reactants. In a final application we use minimal END to study the interaction of a strong laser field with the diatomic molecules HF and LiH . Effects of the polarization of the electronic potential on the dynamics are investigated.

Emphasis is also placed on the development of a general method for interpreting the final time dependent wave-function of the product fragments. The purpose is to analyze the final state wave-function in terms of charge transfer channels as well as individual contributions pertaining to excited states.

CHAPTER 1 INTRODUCTION

The reaction rate constant is usually understood to be one of the most fundamental quantities in chemistry. However, in order to calculate rate constants from a first principles theory we need to understand reactive processes at the single molecule level. Rate constants are obtained from first principles formalism as weighted averages over all different processes working at the molecular level. To understand the chemical reactions is to understand how molecules evolve and transform in time. Over the last twenty years chemists and physicists have developed experiments that investigate reactions at the single molecule level under well controlled conditions. Experimentalists have been able to select initial states of reactants and to perform molecular collisions at specific energies. The level of control over the experiments has reached the point that theoretical results from first principles calculations can be directly compared to, and aid in the interpretation of experiments. However, a different perspective is needed in order to better understand current cross beam, guided ion beam and photochemical experiments to name a few.

This work lies within the realm of time-dependent phenomena in chemistry and physics. The time evolution of a system is governed by the time-dependent Schrödinger equation. In order to describe the time evolution of a molecular system, approximations to the time-dependent Schrödinger equation have to be developed as analytical solutions are known only to a restricted set of model systems. The field of quantum molecular dynamics has seen unparalleled development over the last two decades. Methods for the solution of the time-dependent Schrödinger

equation for a molecular reactive process abound in the literature. However, the majority of these methods make use of the central dogma in both time-dependent and time-independent calculation of molecular properties and reaction rates: the Born-Oppenheimer (BO) approximation. The BO approximation is invoked to separate the Schrödinger equation for the whole system into two separate ones to be solved independently: one for the electrons and another one for the nuclei.

We are interested in the application of time-dependent methods that solve approximately the Schrödinger equation for the study of reactive collisions processes. Traditionally time-independent approaches have been used to make qualitative and sometimes quantitative predictions about chemical reactions and mechanisms. Simple models have been used to predict rate constants, usually the most desired chemical quantity to be calculated, from time-independent results. Chemists want to know if a reaction can happen and how fast it happens. The first question can be addressed by time-independent methods. The answer to the second question, however, needs to include a time-dependent description in an explicit or implicit form. Simple models, commonly based on transition state theory, can produce very good results when reaction conditions under consideration are “mild”. In the time-independent picture mechanistic interpretation is based on extrema features of the electronic potential energy surface (PES).

Because of the success of the use of time-independent methods for the calculation of reaction rates and the difficulty associated with time-dependent descriptions, explicit time-dependent calculations or reaction processes have not become common practice. However, there is a lot to gain from time-dependent approaches as a much clearer picture of reactions mechanism can be drawn from time-dependent simulations. For example, in reactions involving charge transfer,

following how charge changes with nuclear configuration can offer insight into the reaction mechanism and reveal which are the most important nuclear modes to the reaction. In addition explicit time-dependent descriptions can mimic experimental conditions more closely than time-independent descriptions. With time-dependent methods one can for example

- Consider initial energy distributions that match experimental temperatures.
- Consider pure initial states as in experiments that measure state to state cross sections.
- Consider non-equilibrium initial conditions as in the case of photochemical reactions.

Time-dependent methods can be classified in two groups based on the way that they approximate the molecular time-dependent Schrödinger equation. The first group consists of methods that solve the time-dependent Schrödinger equation for the nuclear degrees of freedom subject to a known PES while the second group consists of direct dynamics methods. Direct dynamics in this context means that the electronic and nuclear degrees of freedom are propagated simultaneously. This is different from finding the solution for the electronic problem along a nuclear trajectory. The electron nuclear dynamics (END) method explored in this work is a direct dynamics method.

The electron nuclear dynamics (END) method provides a framework to build a hierarchy of approximations to the Schrödinger equation based on the time-dependent variational principle (TDVP). A general approach is sought to solve the electronic and nuclear problem simultaneously without invoking the Born-Oppenheimer approximation. The dynamical equations of motion are obtained by using the TDVP with wavefunction parametrized according to coherent states

(CS). Direct dynamics methods and in particular the END method have several advantages when compared to other methods, the most obvious ones being

- No need to use cumbersome coordinate systems, cartesian coordinates are used throughout.
- No need to construct potential surfaces.
- Excited electronic states are considered in an approximate and consistent manner.

Because of its qualities the END method can be applied to a wide range of chemical and physical processes.

In the first two studies, we apply the END method to hydrogen abstraction and exchange reactions at hyper-thermal collision energies. Hydrogen abstraction reactions are relatively simple and yet fundamental in detailed experimental investigations. From a theory perspective these reactions provide a wealth of information for testing methods and facilitating the interpretation of results, when comparisons to experiment are appropriate. We investigate the $D_2 + NH_3^+$ reaction at collision energies ranging from 6 to 16 eV and the $H + HOD$ reaction at a collision energy of 1.575 eV. Collision energies refer to center of mass energies. Emphasis is put on the details of the abstraction and exchange reaction mechanisms for ground state reactants. In a final application we use minimal END to study the interaction of a strong laser field with diatomic molecules, namely HF and LiH . Effects of the polarization of the electronic potential on the dynamics are investigated.

1.1 Background Theory

1.1.1 Second Quantization

In this section we introduce electron field operators expressed in a basis of spin orbitals. Electron field operators obey the anti-commutation relations

$$\begin{aligned} [F(r), F^\dagger(r')]_+ &= \delta(r - r') \\ [F(r), F(r')]_+ &= 0 \\ [F^\dagger(r), F^\dagger(r')]_+ &= 0 \end{aligned} \quad (1.1)$$

and in our case are expanded in a basis of spin orbitals $\{\psi\}$ and basis creation operators $\{\mathbf{b}^\dagger\}$ [1]

$$F^\dagger(\mathbf{r}) = \sum_{\mathbf{i}=1}^{\mathbf{K}} \psi(\mathbf{r}) \mathbf{b}_{\mathbf{i}}^\dagger = \psi \mathbf{b}^\dagger. \quad (1.2)$$

Our convention uses ψ as a row array and \mathbf{b}^\dagger as a column array. The basis creation operators obey the anti-commutation relation

$$[b_r, b_s^\dagger]_+ = \delta_{rs} \quad (1.3)$$

$$[b_r^\dagger, b_s^\dagger]_+ = 0 \quad (1.4)$$

$$[b_r, b_s]_+ = 0 \quad (1.5)$$

A single determinantal state of N electrons can be constructed as an ordered product of the basis creation operators

$$|\Psi_0\rangle = \prod_{h=1}^N b_h^\dagger |vac\rangle. \quad (1.6)$$

where $|vac\rangle$ is the no-particle state, with the following mapping between Slater determinants and products of creation operators being valid

$$|\psi_1 \dots \psi_N\rangle \longleftrightarrow \prod_{h=1}^N b_h^\dagger |vac\rangle \quad (1.7)$$

i.e., there is a one to one correspondence between a Slater determinant and a ordered product of basis creation operators. With this mapping and the commutation relations given in Equations 1.3-1.5 expectation values and matrix elements can be calculated for fermionic states (see for example Linderberg and Öhrn [1]) using second quantization algebra.

1.1.2 Diabatic, Adiabatic and END Representation

The distinction between diabatic and adiabatic parametrization of a product molecular wavefunction is at the core of the approximations to the time-dependent and time-independent Schrödinger equations. The original construction of this particular product form is due to Born and Oppenheimer [2] with generalizations by Born and Huang [3]. We will limit at first our discussion to the time-independent Schrödinger equation.

1.1.2.1 Adiabatic representation

Start with the total molecular Hamiltonian

$$H = H_e(x, X) + T_n \quad (1.8)$$

where $H_e(x, X)$ is the electronic Hamiltonian including electronic kinetic energy, internuclear repulsion and electron-electron repulsion. In Equation 1.8 T_n is the nuclear kinetic energy operator, x corresponds to the electronic degrees of freedom while X corresponds to the nuclear degrees of freedom. The time-independent Schrödinger equation for the whole system is given by

$$(H - E)\Xi(x, X) = 0 \quad (1.9)$$

Consider the following expansion in a product form (the Born-Huang expansion)

$$\Xi(x, X; X_0) = \sum_i^N \psi_i(x, X_0)\chi_i(X) \quad (1.10)$$

where $\psi_i(x, X_0)$ are electronic wavefunctions depending on a parameter X_0 and $\chi_i(X)$ are nuclear wavefunctions. The set given by $\{\psi_i(x, X_0)\}$ is composed by the solutions of the N-electron electronic problem (Equation 1.11) and forms a basis for Expansion 1.10

$$(H_e(x, X_0) - e_i(X_0))\psi_i(x, X_0) = 0, \quad i = 1, \dots, N. \quad (1.11)$$

Substituting the Born-Huang (BH) expansion into the molecular Schrödinger equation we obtain

$$(T_n + H_e(x, X_0) - E) \sum_i^N \psi_i(x, X_0) \chi_i(X) = 0 \quad (1.12)$$

Using the fact that the electronic basis set forms an orthonormal set, we can eliminate the explicit dependence on the electronic degrees of freedom by multiplying from the left by $\psi_j^*(x, X_0)$ and integrate over all electronic variables to obtain

$$\sum_i^N \langle \psi_j(x, X_0) | T_n \chi_i(X) | \psi_i(x, X_0) \rangle + (e_j(X_0) - E) \chi_j(X) = 0 \quad j = 1..N \quad (1.13)$$

Equation 1.13 is a coupled set of second order differential equations and has as solutions the nuclear stationary states of the molecular system. The adiabatic choice for the electronic basis consists of making $X_0 \equiv X$ in Equation 1.13 so that the electronic wavefunction depends parametrically on the nuclear degrees of freedom.

The first term in Equation 1.13 (without loss of generality I will use $-\frac{1}{2m}\nabla^2$ as the nuclear kinetic energy operator) produces the following terms

$$\langle \psi_j(x, X) | T_n \chi_i(X) | \psi_i(x, X) \rangle = \quad (1.14)$$

$$-\frac{1}{2m} \left\{ \begin{array}{l} \delta_{ij} \nabla^2 \chi_i(X) + 2 \langle \psi_j(x, X) | \nabla | \psi_i(x, X) \rangle \cdot \nabla \chi_i(X) \\ + \langle \psi_j(x, X) | \nabla^2 | \psi_i(x, X) \rangle \chi_i(X) \end{array} \right\}.$$

The non-adiabatic coupling elements are defined from Equation 1.14 as

$$\tau_{ij}^{(1)} = \langle \psi_j(x, X) | \nabla | \psi_i(x, X) \rangle \quad (1.15)$$

and

$$\tau_{ij}^{(2)} = \langle \psi_j(x, X) | \nabla^2 | \psi_i(x, X) \rangle \quad (1.16)$$

where Equation 1.15 refers to couplings of the first kind and Equation 1.16 refers to couplings of the second kind.

The non-adiabatic coupling element of the first kind are believed to be the most important [4]. Their effects on the dynamics can be non-negligible when adiabatic electronic states change rapidly with changes in the nuclear configuration (X) as in an avoided crossing situation. As this term is also multiplied by $\nabla \chi_i(X)$, the total coupling also depends on how fast the nuclear wave function changes with X . The Schrödinger equation for the nuclei in the electronic adiabatic basis can now be written as

$$-\frac{1}{2m} \nabla^2 \chi_j(X) + (e_j(X) - E) \chi_j(X) - \frac{1}{2m} \sum_i (2\tau_{ij}^{(1)} \cdot \nabla + \tau_{ij}^{(2)}) \chi_i(X) = 0 \quad (1.17)$$

If one considers only diagonal terms ($i = j$) in Equation 1.14, Equation 1.13 becomes effectively a set of uncoupled equations for the nuclear degrees of freedom. At this level of approximation one can solve for the nuclear wavefunction for a single (adiabatic) potential energy surface.

The Born-Oppenheimer equation for the nuclei (the approximation to Equation 1.17) is obtained if we neglect all coupling term from Equation 1.14, resulting in the uncoupled set of equations

$$-\frac{1}{2m} \nabla^2 \chi_j(X) + (e_j(X_0) - E) \chi_j(X) = 0, \quad j = 1, \dots, N. \quad (1.18)$$

The molecular Schrödinger equation in an adiabatic basis can be written in a more succinct form by considering the relations between the non-adiabatic terms given in Equations 1.15 and 1.16 [5].

Consider the derivative of an overlap matrix element

$$\begin{aligned}\nabla\langle\psi_j(x, X)|\psi_i(x, X)\rangle &= 0 \\ \langle\nabla\psi_j(x, X)|\psi_i(x, X)\rangle &= -\langle\psi_j(x, X)|\nabla\psi_i(x, X)\rangle\end{aligned}\tag{1.19}$$

or

$$\tau_{ij}^{(1)} = -\tau_{ji}^{(1)}.\tag{1.20}$$

For real functions ψ_i , the non-adiabatic coupling elements of the first kind form an antisymmetric matrix with zeros on the diagonal. For complex functions the $\tau^{(1)}$ matrix is anti-hermitian.

We can deduce the relationship between the non-adiabatic coupling elements of the first and second kind by considering

$$\nabla\tau_{ij}^{(1)} = \nabla\langle\psi_j(x, X)|\nabla|\psi_i(x, X)\rangle\tag{1.21}$$

then

$$\begin{aligned}\langle\nabla\psi_j(x, X)|\nabla|\psi_j(x, X)\rangle + \langle\psi_j(x, X)|\nabla^2|\psi_i(x, X)\rangle = \\ \langle\nabla\psi_j(x, X)|\nabla|\psi_i(x, X)\rangle + \tau_{ij}^{(2)}\end{aligned}\tag{1.22}$$

or that

$$\tau_{ij}^{(2)} = -\langle\nabla\psi_j(x, X)|\nabla|\psi_i(x, X)\rangle + \nabla\tau_{ij}^{(1)}\tag{1.23}$$

using the resolution of the identity and the fact that $\tau_{ij}^{(1)}$ is antisymmetric we get

$$\tau_{ij}^{(2)} = (\tau_{ij}^{(1)})^2 + \nabla\tau_{ij}^{(1)}\tag{1.24}$$

The last relation can be used in the nuclear Schrödinger equation in an adiabatic basis to obtain

$$-\frac{1}{2m}\nabla^2\chi_j(X) + (e_j(X) - E)\chi_i(X) - \frac{1}{2m}\sum_i\tau_{ij}^{(1)2}\chi_i(X) - \frac{1}{2m}\sum_i(2\tau_{ij}^{(1)}\cdot\nabla + \nabla\tau_{ij}^{(1)})\chi_i(X) = 0 \quad (1.25)$$

which in matrix form reads

$$-\frac{1}{2m}\nabla^2\chi(X) + (\mathbf{e}(X) - \mathbf{E} - \frac{1}{2m}\tau^{(1)2})\chi(X) - \frac{1}{2m}(2\tau^{(1)}\cdot\nabla + \nabla\tau^{(1)})\chi(X) = 0. \quad (1.26)$$

Equation 1.26 can be reorganized to

$$-\frac{1}{2m}(\nabla + \tau^{(1)})^2\chi(X) + (\mathbf{e}(X) - \mathbf{E})\chi(X) = 0 \quad (1.27)$$

In the matrix notation equations, χ is a vector of dimension N , while \mathbf{e} , \mathbf{E} and $\tau^{(1)}$ are square matrices of dimension N^2 .

The non-adiabatic coupling elements have a direct effect on the momentum of the nuclei. For this reason they are called dynamical coupling elements [5]. To solve the nuclear Schrödinger equation non adiabatically (the full coupled set of differential equations), one needs all nonzero dynamical coupling elements between the relevant electronic states.

1.1.2.2 Diabatic representation

The diabatic construction is obtained if we consider X_0 to be a constant in Equation 1.12. As in the previous case, the electronic functions $\{\psi_j(x, X_0)\}$ form an orthonormal set. Originally the diabatic electronic set was constructed by solving the time-independent electronic Schrödinger equation (Equation 1.11) at an equilibrium geometry X_0 . Approximate solutions to the nuclear Schrödinger equation at positions X were sought using perturbation theory [3]. Later the concept of a diabatic representation was extended to include any electronic basis

set constructed so as to minimize the coupling elements given by Equations 1.15 and 1.16.

The diabatic equivalent to Equation 1.17 can be obtained by a similar procedure. Multiplying Equation 1.13 by $\psi_j^*(x, X_0)$ from the left and integrating over all electronic space and spin we obtain

$$\left(-\frac{1}{2m}\nabla^2 - E\right)\chi_j(X) + \sum_i \langle \psi_j(x, X_0) | H_e(x, X) | \psi_i(x, X_0) \rangle \chi_i(X) = 0 \quad (1.28)$$

Using the identity $H_e(x, X) = H_e(x, X_0) + V(x, X) - V(x, X_0)$ and

$$\begin{aligned} \langle \psi_j(x, X_0) | H_e(x, X) | \psi_i(x, X_0) \rangle = & \quad (1.29) \\ \delta_{ij}e_i + \langle \psi_j(x, X_0) | V(x, X) - V(x, X_0) | \psi_i(x, X_0) \rangle & \end{aligned}$$

we can reorganize the Schrödinger equation in the diabatic representation to be

$$\left(-\frac{1}{2m}\nabla^2 - E\right)\chi_j(X) + \sum_i \nu_{ij}(X, X_0)\chi_i(X) = 0 \quad (1.30)$$

where we use the definition $\nu_{ij} = \delta_{ij}e_i + \langle \psi_j(x, X_0) | V(x, X) - V(x, X_0) | \psi_i(x, X_0) \rangle$.

In matrix form, Equation 1.30 has the form

$$\left(-\frac{1}{2m}\nabla^2\right)\chi(X) + (\mathbf{\Omega}(X, X_0) - \mathbf{E})\chi(X) = 0 \quad (1.31)$$

where the matrices $\mathbf{\Omega}$ (the ν_{ij} matrix) and \mathbf{E} are of dimension N^2 and χ is a vector of dimension N .

The non-adiabatic coupling terms in this case are potential coupling elements. To solve the nuclear Schrödinger equation non adiabatically, we need all nonzero potential coupling elements between electronic states.

1.1.2.3 Adiabatic-diabatic transformation

The dynamical coupling elements of the adiabatic representation have the undesired property of growing markedly near curve crossings. Their analytical behavior with energy can be obtained by considering the expression

$$\begin{aligned}
\nabla \langle \psi_i(x, X) | H_e(x, X) | \psi_j(x, X) \rangle = & \quad (1.32) \\
(\nabla \langle \psi_i(x, X) | H_e(x, X) | \psi_j(x, X) \rangle + \langle \psi_i(x, X) | H_e(x, X) \nabla | \psi_j(x, X) \rangle) & \\
+ \langle \psi_i(x, X) | \nabla H_e(x, X) | \psi_j(x, X) \rangle &
\end{aligned}$$

which with the help of 1.11 and 1.20 can be reduced to

$$\tau_{ij}^{(1)} = \frac{\langle \psi(x, X) | \nabla H_e(x, X) | \psi_j(x, X) \rangle}{(e_i(X) - e_j(X))} \quad (1.33)$$

It is very difficult to construct a good adiabatic basis set at a fixed position X_0 that can be used for a global (all X) solution of the Schrödinger equation. As a result Equation 1.30 in its present form is not very useful.

An alternative solution is to define an adiabatic-to-diabatic representation transformation at all nuclear configurations X . There are formal and empirical ways to introduce such a transformation, see Baer [5] and Sidis [6] for a discussion on the subject. The resulting Schrödinger equation, although closely related to the diabatic representation given by Equation 1.30, is in this case more convenient to solve for arbitrary nuclear configurations. This new construction enables one to define diabatic representations that also have nuclear configuration dependence. The disadvantage is that, as in the adiabatic case, dynamical coupling elements are also present in the Schrödinger equation. However, unlike the diabatic case dynamical coupling elements can be made to be slowly varying with respect to changes in nuclear configuration. Constraints can be imposed on the transformation so that the resulting Schrödinger equation has small or vanishing dynamical coupling elements.

A time-independent Schrödinger equation in terms of a modified adiabatic basis has potential and dynamical coupling elements. In matrix notation it can be written as

$$-\frac{1}{2m}(\nabla^2 + \tau^{(1)})\chi(X) + (W(X, X_0) - E)\chi(X) = 0 \quad (1.34)$$

where

$$W = A^\dagger \nu A \quad (1.35)$$

with A being the diabatic to adiabatic transformation matrix.

1.1.2.4 Time-dependent parametrization

The extension of the BH expansion to a time-dependent form is usually done in a way to leverage on the knowledge gained in solving the time-independent Schrödinger equation. The spatial dependence in the electronic and nuclear variables is kept and all the time dependence is introduced in an additional parameter set $\{\mathbf{c}\}$.

$$\Xi(x, X, t; X_0) = \sum_i^N c(t)_i \psi_i(x, X_0) \chi_i(X) \quad (1.36)$$

Because the same functional dependence is kept for the spatial dependence part, all the coupling term definitions for adiabatic and diabatic representations carry over to the time-dependent Schrödinger description.

1.1.2.5 END diabatic representation

The electron nuclear dynamics method employs a diabatic parametrization of the molecular wave function. The END diabatic product has as parameters the average nuclear positions (R) and momenta (P) in addition to electronic wavefunction parameters \mathbf{z} . As in the BH expansion the END expansion can be written in a general form as sums of products of electronic and nuclear parts, i.e.

$$\Xi(x, X, t; \mathbf{z}, R, P) = \sum_i^N c(t) \psi_i(x; \mathbf{z}, R, P) \chi_i(X; R, P). \quad (1.37)$$

Such a functional dependence implies that, as in Equation 1.34, dynamical equations derived from such parametrization will have both dynamical and potential couplings.

In the simplest case of a single product ($N = 1$) approximation to the wavefunction, the END product can be written as

$$\Xi(x, X, t; \mathbf{z}, R, P) = \psi(x; \mathbf{z}, R, P) \chi(X; R, P) \quad (1.38)$$

where R and P are average position and momenta of the nuclei and \mathbf{z} are the electronic wavefunction parameters. Both Equations 1.37 and 1.38 depend on the time-dependent parameters \mathbf{z} , R and P . Equation 1.38, however, depends on time only through the wavefunction parameters and defines the minimal parametrization for the END method. As we shall see the solution for time evolution of the wavefunction parameters amounts to the time-dependent Hartree-Fock (TDHF) method for electrons and nuclei.

1.2 Solutions to the Time-Dependent Schrödinger Equation

In this section we review time-dependent methods that approximate the solution of the time-dependent Schrödinger equation

$$i \frac{d}{dt} \Xi(x, X, t) = H(x, X, t) \Xi(x, X, t) \quad (1.39)$$

We place emphasis on methods that attempt to include non-adiabatic effects and do not use predefined potential energy surfaces (PES).

1.2.1 Time-Dependent Close Coupling Method

The close coupling method attempts to solve the Schrödinger equation directly by employing an expansion of the wave function usually given by [7, 8]

$$\psi(x, X) = \sum_n c_n(t) \phi_n(\vec{r}; R(t)) \exp \left[\frac{im}{2m} \vec{v} \cdot \vec{r} f_n(\vec{r}; R(t)) \right] \exp \left[\int^t \left(U_n(R(t')) + \frac{mv^2}{8} \right) dt \right] \quad (1.40)$$

Expansion in terms of adiabatic electronic eigenstates is commonly used. As in Equation 1.36, all time dependence is contained in the expansion coefficients. The close coupling equations resulting from Expansion 1.40 are usually solved along prescribed classical nuclear coulombic or rectilinear paths.

Equation 1.40 presents an expansion of the electronic wavefunction in terms of an electronic basis $\{\phi\}$ with time-dependent coefficients \mathbf{c} . $U_n(R)$ is the electronic potential energy, m is the electron mass and $f_n(\vec{r}, R(t))$ is a parametric function of the nuclear positions. Because of the limitations concerning the solution of the nuclear part and the need for global PES with coupling elements, the close coupling method has been used mostly to describe charge transfer reactions of small systems at relatively high energies.

1.2.2 Classical Path Method

The variant of the classical path described here uses nuclear coordinates as parameters and electronic variables as the internal quantum variables. With this parametrization, the classical path method [9, 4] is very similar in spirit to the close coupling approach as explained above. It uses a similar parametrization (see Equation 1.41) of the electronic wavefunction, however, it does not contain explicit terms to account for Galilean invariance of the electronic wavefunction. As in the

close coupling approach, the dependence of the solution on the nuclear degrees of freedom is parametric. The principal difference between the two approaches is that in the classical path method the solution of the classical nuclear equations of motion is attempted simultaneously with the propagation of the electronic coupled sets of equations. In the classical path method the forces acting on the classical nuclei are computed as an *ad-hoc* average between the electronic states involved in the dynamics.

The classical path method uses the parametrization

$$\psi(\mathbf{r}, \mathbf{R}) = \sum_n c_n(t) \phi_n(\mathbf{r}, \mathbf{R}) \exp \frac{i}{\hbar} \int^t U(R(t')) dt \quad (1.41)$$

in terms of the electronic basis $\{\phi\}$, the time-dependent coefficients \mathbf{c} and the electronic potential energy $U_n(R)$.

1.2.3 Trajectory Surface Hopping Method

The trajectory surface hopping method (TSH) [10] (for a review on the subject see Chapman [11]) attempts to solve the equations for the classical path method with the parametrization described above by using a probabilistic scheme. Instead of solving the coupled set of equations at all nuclear configurations, a hopping probability for the electronic configuration is computed at each instant in time. The resulting equation for the classical nuclei depends only on the hopping probability between the states involved (usually two). All explicit electronic dynamics (and phase information) is removed on the TSH method.

1.2.4 Car-Parrinello Method

The Car-Parrinello (CP) [12] method has been extensively used for structure as well as dynamics simulations. The CP method tries to find minima for the following energy functional

$$E[\{\psi_i(\vec{r}, \vec{R})\}, \{\vec{R}\}, \{\alpha\}] = \sum_i \int_{\Omega} d^3r \psi_i^*(\vec{r}, \vec{R}) \left[-\frac{\hbar^2}{2m} \nabla^2 + U(n(r), \{\vec{R}\}), \{\alpha\} \right] \psi_i(\vec{r}, \vec{R}) \quad (1.42)$$

where $U(n(r), \{\vec{R}\}, \{\alpha\})$ is the potential including the electronic energy, internuclear repulsion and the potential resulting from any external constraint, $n(r)$ is the electronic density defined according to Kohn-Sham theory as $n(r) = \sum_i \psi_i^*(\vec{r}) \psi_i(\vec{r})$, \vec{R}_I are the ions positions and $\{\psi_i(\vec{r}, \vec{R})\}$ is an electronic adiabatic single particle basis set. The minimization of the functional above is equivalent to finding the solution for the Kohn-Sham [13] problem.

In order to obtain equations of motion a Lagrangian is also introduced

$$L(\vec{r}, \vec{R}, n(r)) = - \sum_i \int_{\Omega} d^3r \frac{\mu}{2} |\dot{\psi}_i(\vec{r})|^2 + \sum_I M_I \dot{R}_I^2 + \sum_{\nu} \frac{1}{2} \mu_{\nu}^2 - E[\{\psi_i(\vec{r}), \{\vec{R}\}, \{\alpha\}] \quad (1.43)$$

where μ and μ_{ν} are arbitrary parameters and M_i are the ions masses.

The CP method attempts to minimize the above energy functional by employing a simulating annealing [14] procedure on wave function parameters (coefficients of the KS orbitals), the ions positions and the constraint parameter(s) α . The Lagrangian function given above is used to define equations of motion for the variational parameters. From the equations of motion, a simulated annealing procedure is implemented. It is important to note that the equations of motion derived from the CP procedure are only meaningful when $\ddot{\psi}$ is equal to zero. This guarantees that propagation of the nuclei happens on the Born-Oppenheimer surface given by the solution of the KS equation for the electrons. The CP method as explained here is not suitable for describing any explicit electronic (non-Born-Oppenheimer) dynamics.

1.2.5 Time-Dependent Hartree-Fock Based Methods

In the context of (time-independent) electronic structure calculations the time-dependent hartree-fock (TDHF) method calculates the linear response of a system described by a single Slater determinant. The equations for the TDHF method can also be obtained by considering the second order (harmonic) expansion of the single determinant expression for the energy in terms of the electronic wavefunction parameters [1]. The TDHF or RPA approximation amounts to finding the normal modes for the electronic degrees of freedom [15].

For a time-dependent description, the TDHF method appears as an approximation to the time-dependent Schrödinger equation. It is a consequence of considering a single term in the BH expression (cf. Equation 1.38) for the wave function with nuclei considered as classical particles and the electronic wavefunction as a single determinant. The TDHF method has a long history as it was already proposed in the 30s by Dirac[16]. Early applications for scattering [17, 18] did not consider the nuclear motion to be dynamic. These original applications did not consider explicit electron nuclear coupling as prescribed coulombic or straight line trajectories were used. Later derivations obtained the TDHF equations for the evolution of the wavefunction parameters by constructing a Lagrangian and applying the time-dependent variational principle (TDVP) [19, 20, 21, 22] or by using an density matrix propagation scheme [23] with classical nuclei. If no approximations are made this procedure ensures that instantaneous couplings between electronic and nuclear degrees of freedom are considered during the dynamics. The later applications of the TDHF method are the only ones suitable for describing chemical reactions.

The END method in its simplest implementation is a TDHF method for electrons and nuclei. It consists of using a wave function parametrized according to equation 1.38 and employing the time-dependent variational principle [24] in order

to obtain equations of motion for the wave function variational parameters \mathbf{c} , \mathbf{z} , R and P . In its minimum implementation, only \mathbf{z} , R and P are used as parameters. The resulting equations are a generalization of the Time-Dependent Hartree-Fock equations for moving nuclei.

1.3 Electron Nuclear Dynamics (END) Method

The complete END equations include all couplings between the electronic and nuclear degrees of freedom. These couplings have the general form that depends on the parametrization of the wavefunction (c.f. Equations 1.37 and 1.38). The addition of interaction of matter with an external field to such a formalism is straightforward if we consider the description of fields in the semiclassical limit (high intensity).

The END theory has been the focus of many publications [25, 26, 27] and will be briefly reviewed here. Emphasis is placed on the topics judged to be most important for the understanding of the analysis presented in the following chapters.

At the core of the END theory is the time-dependent variational principle, which is based on the definition of the quantum action [28]

$$A = \int_{t_1}^{t_2} L(\zeta^*, \zeta) dt, \quad (1.44)$$

where the quantum mechanical Lagrangian (with symmetric time derivatives and $\frac{i}{2} \frac{\bar{\partial}}{\partial t}$ acting on the left side) is defined as

$$L(\zeta^*, \zeta) = \langle \zeta | \frac{i}{2} \frac{\partial}{\partial t} - \frac{i}{2} \frac{\bar{\partial}}{\partial t} - \hat{H} | \zeta \rangle / \langle \zeta | \zeta \rangle \quad (1.45)$$

where H is the quantum mechanical Hamiltonian of the system and ζ is a vector of time-dependent complex parameters. For the states considered for the END ansatz time dependence is obtained through the variational parameters. With this constraint the quantum Lagrangian has the form (using the chain rule)

$$L = \frac{i}{2} \sum_{\alpha} \left(\frac{\partial \ln S}{\partial \zeta_{\alpha}} \dot{\zeta}_{\alpha} - \frac{\partial \ln S}{\partial \zeta_{\alpha}^*} \dot{\zeta}_{\alpha}^* \right) - E \quad (1.46)$$

where we used $E = \langle \zeta | \hat{H} | \zeta \rangle / \langle \zeta | \zeta \rangle$ and $S(\zeta^*, \zeta) = \langle \zeta | \zeta \rangle$. The equations of motion (EOM) are obtained by making the action stationary and imposing fixed endpoints boundary conditions. The equations of motion in terms of general variational parameters is given by

$$i \sum_{\beta} C_{\alpha\beta} \dot{\zeta}_{\beta} = \frac{\partial E}{\partial \zeta_{\alpha}^*} \quad (1.47)$$

$$-i \sum_{\beta} C_{\alpha\beta}^* \dot{\zeta}_{\beta}^* = \frac{\partial E}{\partial \zeta_{\alpha}} \quad (1.48)$$

Note the marked similarity between Equation 1.47 and the classical Hamilton's equation. In Equation 1.47, the sums run over the parameter set $\{\zeta\}$. The Hermitian metric matrix \mathbf{C} elements are given by

$$C_{\alpha\beta} = \frac{\partial^2 \ln S}{\partial \zeta_{\alpha}^* \partial \zeta_{\beta}}. \quad (1.49)$$

The equations of motion in matrix form reads

$$i \begin{bmatrix} C & 0 \\ 0 & -C^* \end{bmatrix} \begin{bmatrix} \dot{\zeta} \\ \dot{\zeta}^* \end{bmatrix} = \begin{bmatrix} \frac{\partial E}{\partial \zeta^*} \\ \frac{\partial E}{\partial \zeta} \end{bmatrix} \quad (1.50)$$

The END ansatz is a molecular coherent state constructed from

$$|\zeta\rangle = |z, R\rangle |R, P\rangle \equiv |z\rangle |\phi\rangle, \quad (1.51)$$

where the nuclear part is a product of Gaussians of the type

$$|\phi\rangle = \prod_k \exp\left[-\frac{1}{2} \left(\frac{X_k - R_k}{b}\right)^2 + iP_k(X_k - R_k)\right] \quad (1.52)$$

and the electronic part is a single determinantal (unnormalized) coherent state

$$|\mathbf{z}\rangle = \exp\left[\sum_{j=N+1}^K \sum_{i=1}^N z_{ji} b_j^{\dagger} b_i\right] |0\rangle. \quad (1.53)$$

Note that the electronic state $|\mathbf{z}\rangle$ depends only on z . This fact ensures that the structure of the equations of motion derived from such ansatz have the same form as Equation 1.50.

The Lagrangian for the molecular system in the narrow wavepacket approximation for the nuclei is given by

$$L = \sum_{j,l} \left\{ [P_{jl} + \frac{i}{2} (\frac{\partial \ln S}{\partial R_{jl}} - \frac{\partial \ln S}{\partial R'_{jl}})] \dot{R}_{jl} + \frac{i}{2} (\frac{\partial \ln S}{\partial P_{jl}} - \frac{\partial \ln S}{\partial P'_{jl}}) \dot{P}_{jl} \right\} + \frac{i}{2} \sum_{p,h} \left(\frac{\partial \ln S}{\partial z_{ph}} \dot{z}_{ph} - \frac{\partial \ln S}{\partial z_{ph}^*} \dot{z}_{ph}^* \right) - E \quad (1.54)$$

with $S = \langle z, R', P' | z, R, P \rangle$ and

$$E = \sum_{jl} P_{jl}^2 / 2M_l + \langle z, R', P' | H_{el} | z, R, P \rangle / \langle z, R', P' | z, R, P \rangle. \quad (1.55)$$

where the electronic energy Hamiltonian is given by

$$H_{el} = \sum_{A,B} \frac{Z_A Z_B}{r_{A,B}} + \frac{1}{2m_e} \sum_i \nabla_i^2 + \sum_{i,j} \frac{1}{r_{i,j}} \quad (1.56)$$

The equations of motion are obtained by minimizing the action as before. The resulting EOM are a set of coupled differential equations given by

$$\begin{bmatrix} i\mathbf{C} & \mathbf{0} & i\mathbf{C}_{\mathbf{R}} & i\mathbf{C}_{\mathbf{P}} \\ \mathbf{0} & -i\mathbf{C}^* & -i\mathbf{C}_{\mathbf{R}}^* & -i\mathbf{C}_{\mathbf{P}}^* \\ i\mathbf{C}_{\mathbf{R}}^\dagger & -i\mathbf{C}_{\mathbf{R}}^{\mathbf{T}} & \mathbf{C}_{\mathbf{R}\mathbf{R}} & -\mathbf{I} + \mathbf{C}_{\mathbf{R}\mathbf{P}} \\ i\mathbf{C}_{\mathbf{P}}^\dagger & -i\mathbf{C}_{\mathbf{P}}^{\mathbf{T}} & \mathbf{I} + \mathbf{C}_{\mathbf{P}\mathbf{R}} & \mathbf{C}_{\mathbf{P}\mathbf{P}} \end{bmatrix} \begin{bmatrix} \dot{\mathbf{z}} \\ \dot{\mathbf{z}}^* \\ \dot{\mathbf{R}} \\ \dot{\mathbf{P}} \end{bmatrix} = \begin{bmatrix} \partial E / \partial \mathbf{z}^* \\ \partial E / \partial \mathbf{z} \\ \partial E / \partial \mathbf{R} \\ \partial E / \partial \mathbf{P} \end{bmatrix}, \quad (1.57)$$

where the coupling terms in the narrow wave packet limit (zero width) are

$$(C_{XY})_{ij;kl} = -2Im \frac{\partial^2 \ln S}{\partial X_{ik} \partial Y_{jl}} \Big|_{R'=R}, \quad (1.58)$$

$$(C_{X_{ik}})_{ph} = \frac{\partial^2 \ln S}{\partial z_{ph}^* \partial X_{ik}} \Big|_{R'=R}, \quad (1.59)$$

and

$$C_{ph:qg} = \frac{\partial^2 \ln \mathcal{S}}{\partial z_{ph}^* \partial z_{qg}} \Big|_{R=R'}. \quad (1.60)$$

The coupling elements given by Equations 1.58-1.60 correspond to terms related to the Galilean invariance, non-adiabatic coupling, and pure electronic coupling between electronic states [29, 25] respectively.

1.3.1 Narrow Wavepacket Limit

As mentioned earlier the dynamical equations above were derived taking the width of nuclear wavepackets to be zero. That approximation is comparable to the frozen Gaussian approximation.

The effect of adding a width to the dynamical equations can be understood by its individual effects on the terms of the Lagrangian. The expectation value of the \hat{p}^2 operator of a Gaussian wavefunction is $\langle \hat{p}^2 \rangle = \langle -\partial^2 / \partial x^2 \rangle = p^2 + 1/2b^2$, so the frozen width term in that case is only a constant to be added to the kinetic energy. There is no contribution to the dynamics of the system due to this term.

The electron nuclear attraction integrals will change their value modestly due to the finite width of the nuclear charge distribution. Those effects however are minor because the width of the electronic wavefunction is much greater than the width of the nuclear wavefunction.

The overlap term can have nonzero off diagonal components due to the nuclear wavefunction. Although this can happen, only high energy scattering processes would make those terms of a sufficient size to be important. It is well-known that the innermost orbital of second row elements hardly affect processes of chemical interest.

Minimal END dynamics as presented in Section 1.3 therefore is completely equivalent to dynamics with frozen Gaussian [30, 31] for the collision energies in question.

1.3.2 Molecular Dynamics

Simplifications of the complete END equations are possible under certain circumstances and can greatly reduce the computational requirements. Such approximations are useful in comparing the END method with other methods. The END equations provide a general approach to molecular dynamics, so that standard equations for dynamics on the potential surface are easily obtained from the END equations.

In particular, if we require the stationary condition ($\dot{z}^* = \dot{z} = 0$) for the electronic wavefunction in equation (7) molecular dynamics (MD) equations are obtained. The nuclear potential is given by the z parameters that satisfy

$$-iC_R^* \dot{R} = \frac{\partial E(z, z^*, R, P, \varepsilon)}{\partial z} \quad (1.61)$$

or in the presence of an external electromagnetic field

$$\frac{\partial E_0(z, z^*, R, P)}{\partial z} + \frac{\partial \mu}{\partial z} \vec{\varepsilon} = iC_R \dot{R}. \quad (1.62)$$

Equation 1.62 includes two terms that are truly dynamical. One is the dipole term that depends on the time-dependent field, and the other is the boost term that is related to a Galilean transformation of the electronic reference frame to the moving nuclear frame. This boost term has an equivalent effect on the dynamics as the electronic translation factors (ETF) usually employed to basis functions that follow the nuclear motion. These two terms are the difference between the electronic structure calculations performed in this work and the electronic potential surface usually used for standard MD calculations.

The dynamical equations in this approximation have a form consistent with the fact that $\dot{z} = 0$ and are

$$\begin{bmatrix} \mathbf{C}_{RR} & -\mathbf{I} \\ \mathbf{I} & \mathbf{0} \end{bmatrix} \begin{bmatrix} \dot{\mathbf{R}} \\ \dot{\mathbf{P}} \end{bmatrix} = \begin{bmatrix} \partial E / \partial \mathbf{R} \\ \partial E / \partial \mathbf{P} \end{bmatrix}. \quad (1.63)$$

Note that one of the coupling terms is still present in the dynamical equations. The C_{RR} term (in this case) is just a friction like term related to the dragging force of the electrons on the center. The dynamics takes place on an adiabatic potential surface. These are the equations referred in this work as molecular dynamics (MD).

We can make two distinct approximations. The first is to neglect the dependence on the center velocity of the electronic energy (neglect the boost term in eqn. 1.61). This reduces the Equations for the electronic part to Hartree-Fock (HF) equations. For consistency C_{RR} is also set to zero in Equation 1.63.

Another approximation consists of neglecting the dipole contribution to the electronic energy when constructing the electronic wavefunction. This is what is usually done when a pre-calculated potential surface is used to study the dynamics of the nuclear wavefunction under the influence of an electromagnetic field.

The exclusion of the dipole term from the calculation of the electronic energy and density introduces some changes to the calculation of the force term ($\frac{\partial E}{\partial R}$) in Equation 1.63. Because an electronic state calculated by neglecting the effects of the external field is not stationary, extra terms would be introduced in the energy derivative expression. The non-polarized molecular dynamics (NPMD) is a molecular dynamics method that neglects the effects of the external field in the electronic configuration both in the energy and energy derivatives. As the name indicates, the electronic wavefunction is not allowed to polarize in the presence of the field.

As we shall see, the MDNP method is useful for comparison purposes because with it we are able to introduce a hierarchy of methods classified with respect to the behavior of the electrons under the action of a field. According to their dynamical behavior we can have full dynamical electrons (END), polarizable electrons (MD), or static electrons (MDNP).

1.4 Cross Sections Calculations

As an experimental observable, total cross section (TCS) is an important quantity to measure and compute. As the theoretical definition follows from the concept of flux, a direct experimental measurable quantity, straight comparisons can be made between theoretical and experimental results. The TCS can be defined in terms of an integral over the differential cross section (DCS). The DCS is an important quantity for theory as it relates to the deflection function from both quantum and classical formalisms. In this section we introduce the subject of classical binary collision for a central potential. Later in the section a connection between classical and quantum solutions for the scattering problem is made. A small generalization to reactive scattering processes is also mentioned.

1.4.1 Differential Cross Section

The formal differential cross section (DCS) for a collision problem is defined as

$$d\sigma(E) = \frac{\text{number of particles scattered into solid angle } d\Omega \text{ per unit time}}{\text{incident beam intensity}} \quad (1.64)$$

The binary collision problem has as constants of motion the collision energy and the total angular momentum. For a structureless or nonrotating target the angular momentum is specified by the initial impact parameter b . Enforcing particle conservation for a scattering by a central potential we obtain

$$2\pi I b |db| = 2\pi \frac{d\sigma(E, \theta)}{d\theta} I \sin \theta |d\theta| \quad (1.65)$$

with I being the incident beam intensity, θ the scattering angle, E the collision energy and b the impact parameter. The definition of the DCS for scattering by a central potential is therefore given by

$$\frac{d\sigma(E)}{d\theta} = \frac{b}{\sin \theta} \left| \frac{db}{d\theta} \right| = \frac{b}{\sin \theta} \left| \frac{db}{db} \right|. \quad (1.66)$$

The total cross section is defined as an integral over the DCS

$$\sigma(E) = 2\pi \int \frac{d\sigma(E)}{d\theta} \sin \theta d\theta. \quad (1.67)$$

From classical trajectories obtained from any of the semiclassical methods described previously in this document we can calculate the deflection angle Θ as a function of the impact parameter b . The function resulting from this calculation is called a deflection function ($\theta(b)$) and plays a central role in scattering theory. As experiments cannot make a distinction between positive and negative deflection angles, the scattering angle used in Equations 1.65 and 1.66 is defined w.r.t the deflection angle computed for trajectories such that

$$\theta = |\Theta| \text{ with } 0 < \theta < \pi. \quad (1.68)$$

The foremost feature of the classical DCS given by Equation 1.66 is that it has a singularity for θ equal 0, π and at the extrema of the deflection function $\theta(b)$. At these values of the deflection angle quantum effects are important for a correct description of the DCS. The cases where $\theta = 0$ or $\theta = \pi$ are called glory scattering while the cases where the deflection function has a maximum or minimum is called rainbow scattering. Semiclassical corrections to the DCS for small angles were derived by Shciff [32] with applications to scattering using the END method by

Cabrera-Trujillo et al. [33]. Rainbow scattering corrections were first developed by Berry [34] and applied in the END context by Morales [35] for the $H^+ + H_2$ charge transfer reaction and by Hedström [36] for the $H^+ + H_2O$ charge transfer reaction.

Fortunately, for the reactive cases treated in this document we do not encounter such difficulties. The deflection functions calculated are all repulsive in character and do not possess a singularity on the cross section for all impact parameters investigated. The standard classical expression was used to compute cross sections in this document.

For probabilistic events coupled to classical nuclei, such as electron transfer reaction, the more general expression for the classical DCS is to be used, i.e.

$$\frac{d\sigma_k(E)}{d\theta} = \sum_s \frac{b_s P_k(b_s)}{\sin \theta \left| \frac{d\theta}{db} \right|_{b=b_s}}, \quad (1.69)$$

where we introduce a sum over trajectories with the same scattering angle. In Equation 1.69, $P_k(b)$ is the probability of an event labeled by k . In the END context k usually labels a reactive or charge transfer channel. A brief review of semiclassical theory and the relations between classical and semiclassical results is presented in section 1.4.4

1.4.2 Classical Collisions

The classical description of a binary collision process introduces several fundamental concepts used throughout this document. In this section we outline the collision of two structureless particles interacting via a potential that depends only on the internuclear distance ($V(R)$).

The kinetic energy of two particles is given by

$$E_k = \frac{m_1}{2} \vec{v}_1^2 + \frac{m_2}{2} \vec{v}_2^2 = \frac{(m_1 + m_2)}{2} \vec{V}^2 + \frac{\mu}{2} \vec{v}^2 \quad (1.70)$$

where on the r.h.s we expressed the kinetic energy in terms of the relative velocity, the center of mass velocity and the reduced mass where

$$\vec{v} = \vec{v}_1 - \vec{v}_2 \quad (1.71)$$

$$\vec{V} = m_1\vec{v}_1 + m_2\vec{v}_2 \quad (1.72)$$

$$\mu = \frac{m_1 m_2}{(m_1 + m_2)}. \quad (1.73)$$

This new set of coordinate is usually refered to as center of mass coordinates. The kinetic energy associated with the collision process is given by

$$E_{kin} = \frac{1}{2}\mu^2\vec{v}^2. \quad (1.74)$$

For a spherically symmetric potential it is useful to define a new set of coordinates by centering the target at the origin and decomposing the velocity vector in its radial and angular components

$$\vec{v} = \dot{R}\vec{e}_R + R\dot{\theta}\vec{e}_\theta, \quad (1.75)$$

where \vec{e}_R and \vec{e}_θ are the radial and angular unit vectors. The relative kinetic energy in this new set of coordinates is given by

$$E_k = \frac{1}{2}\mu(\dot{R}^2 + R^2\dot{\theta}^2) = \frac{1}{2}\dot{R}^2 + \frac{J^2}{2\mu R^2} \quad (1.76)$$

where we used the definition of the total angular momentum for the system

$$\vec{J} = \vec{R} \times \mu\vec{v} = \mu R^2\dot{\theta}\vec{e}_\perp. \quad (1.77)$$

The conjugate momenta of R and θ is ($L = T - U$)

$$p_R = \frac{\partial L}{\partial \dot{R}} = \mu\dot{R}, \quad (1.78)$$

$$p_\theta = \frac{\partial L}{\partial \dot{\theta}} = \mu R^2\dot{\theta} = |J|, \quad (1.79)$$

respectively, where J is the total angular momentum.

The Hamiltonian is defined as

$$H = p_R \dot{R} + p_\theta \dot{\theta} - L = \frac{1}{2\mu} \left(p_R^2 + \frac{p_\theta^2}{R^2} \right) + U(R), \quad (1.80)$$

with the corresponding Hamilton's equations of motion for the conjugate momenta as

$$\dot{p}_R = -\frac{\partial H}{\partial R} = \frac{p_\theta^2}{\mu R^3} - \frac{\partial U}{\partial R}, \quad (1.81)$$

$$\dot{p}_\theta = -\frac{\partial H}{\partial \theta} = 0. \quad (1.82)$$

Equation 1.82 shows that p_θ is a constant of motion and that the total angular momentum is conserved. The magnitude of the total angular momentum of the collision is also related to the initial impact parameter and the initial collision velocity by

$$|J| = m|v_{t=0}|b = \mu R|v| \sin \theta_{t=0} \quad (1.83)$$

The final $|\theta|$ for the collision, called scattering angle, can be calculated by using Expression 1.77 and 1.80 (with $H = E$) and the equation

$$\int_{R_i}^{R_f} \frac{d\theta}{dr} = \pm \int_{R_i}^{R_f} \frac{\dot{\theta}}{\dot{R}} dR \quad (1.84)$$

with the minus sign corresponding to attractive scattering and the positive sign to repulsive scattering. Considering that the integral is symmetric w.r.t the distance of closest approach (R_0) we can write

$$|\theta| = \pi - 2b \int_{R_0}^{\infty} \frac{dR}{R^2 \left(1 - \frac{b^2}{R^2} - \frac{U(R)}{E} \right)^{\frac{1}{2}}}. \quad (1.85)$$

Equation 1.85 is the classical expression for the scattering angle generated by a central potential in the center of mass coordinate system.

1.4.3 Laboratory-Center of Mass Coordinate Transformation

We demonstrate in the last section that the intrinsic features of a scattering problem can be more clearly described in the center of mass coordinate frame. Because of this most theory and several experimental results are reported in the center of mass frame. We present in this section a brief review of laboratory-center of mass (CM) transformation for the scattering angle and differential cross sections. For reactive processes however there is no unique way of defining a global set of internal coordinates for describing reactants and products. Some coordinate representations used to describe reactive processes in polyatomics, e.g. the Jacobi coordinate set, do not present a continuous parametrization for a reactive process. The problem of using internal or center of mass coordinates is worsened for multi-channel reactions where the coordinates for reactants and each one of the products may not have a continuous parametrization. That is one of the reasons that a cartesian set of coordinates for describing a reactive process is used with the END theory.

The Laboratory-CM coordinate transformation can be better understood by considering a vector diagram (a Newton diagram) of the velocities of the particles involved on the collision process. In Figures 1.2 and 1.1 initial quantities are labeled by i while final quantities are labeled by f . Primes quantities refer to relative coordinates while unprimed quantities refer to laboratory coordinates.

Consider the triangle depicted in Figure 1.1. By using simple trigonometric rules we can relate laboratory quantities to CM quantities. Transformations from CM to laboratory scattering angle can be found by simple algebraic manipulations. Consider the equation

$$v_{1f} \sin \varphi = v'_{1f} \sin \Theta \quad (1.86)$$

$$v_{1f} \cos \varphi = v'_{1f} \cos \Theta + V_{cm} \quad (1.87)$$

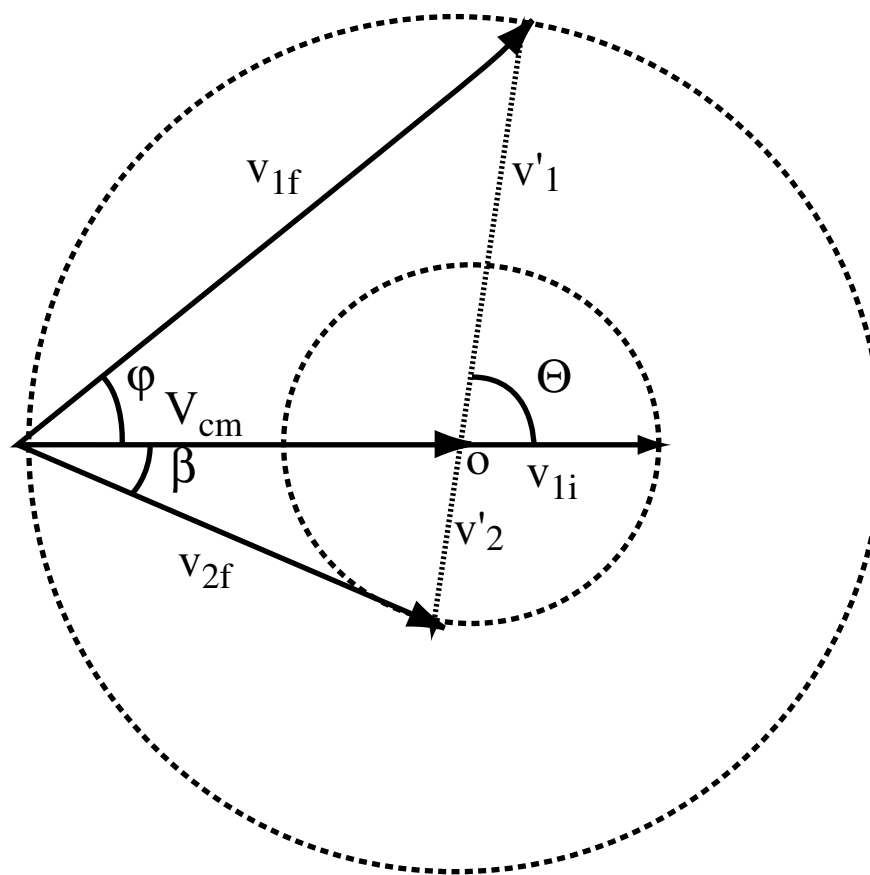


Figure 1.1: Newton diagram for a collision process with the target initially at rest. Only final quantities are plotted.

to find that (completing squares)

$$v_{if} = \sqrt{v'_{1f}{}^2 + \rho^2 + 2\rho \cos \Theta} \quad (1.88)$$

where we use $V_{cm} = \frac{\mu}{m_2}v_{1i}$ and define the collision parameter $\rho = \frac{\mu v_{1i}}{m_2 v'_{1i}}$ in terms of the initial collision velocity v_{1i} and the final projectile velocity in the center of mass frame. With Equation 1.88 we can define the laboratory scattering angle in terms of center of mass quantities

$$\cos \varphi = \frac{\cos \Theta + \rho}{\sqrt{1 + \rho^2 + 2\rho \cos \Theta}}. \quad (1.89)$$

The inverse transformation (laboratory to CM scattering angle) can be found by considering the relations

$$v'_{1f} \sin \Theta = v_{1f} \sin \varphi, \quad (1.90)$$

$$v'_{1f} \cos \Theta = v_{1f} \cos \varphi - V_{cm}. \quad (1.91)$$

With similar manipulations we obtain the CM scattering angle in terms of laboratory quantities, i.e.

$$\cos \Theta = \frac{\cos \varphi - \rho'}{\sqrt{1 + \rho'^2 - 2\rho' \cos \varphi}} \quad (1.92)$$

where we define a new collision parameter ρ'

$$\rho' = \frac{\mu_1 v_{1i}}{m_2 v_1}. \quad (1.93)$$

Equation 1.92 defines the CM scattering angle in terms of laboratory quantities only.

A transformation for the differential cross section between laboratory and CM frames can be found by imposing flux conservation of particles

$$2\pi I\sigma(\Theta) \sin \Theta d\Theta = 2\pi I\sigma(\varphi) \sin \varphi d\varphi \quad (1.94)$$

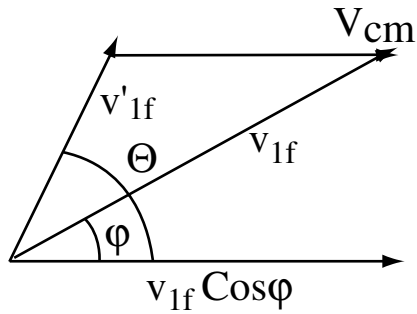


Figure 1.2: Velocity vectors from Newton diagram (Fig. 1.1) used to construct the CM-laboratory transformation.

which can be rearranged to

$$\sigma(\varphi) = \sigma(\Theta) \left| \frac{d(\cos \Theta)}{d(\cos \varphi)} \right|. \quad (1.95)$$

Equation 1.95 can be used together with Equation 1.94 to find a transformation between the differential cross section represented in terms of center of mass quantities to one in terms of laboratory quantities [37].

1.4.4 Semiclassical Differential Cross Section

A formal relationship between the quantum and classical differential cross section (DCS) can be obtained by means of the semiclassical theory. We start by reviewing a few results for the quantum scattering problem under the influence of a spherical potential ($V(r)$). Due to the symmetry of the problem L^2 , L_z are good quantum numbers. Therefore we seek solutions that are also solutions of L^2 , L_z and H . Our search starts by investigating the solution for the free particle problem in terms of spherical waves. The quantum and semiclassical treatment followed in this section deals only with elastic scattering processes.

The time-independent Schrödinger equation for scattering off a central potential is given by

$$[\nabla^2 - \frac{2m}{\hbar^2}V(r) + k^2]\Psi(\vec{r}) = 0 \quad (1.96)$$

where the momentum $\vec{p} = \hbar\vec{k}$ defines the collision energy

$$E = \frac{p^2}{2m}. \quad (1.97)$$

An interesting expression for the DCS that enables us to connect semiclassical and quantum theories is defined with respect to the scattering amplitude and is given by

$$\frac{d\sigma}{d\Omega} = |A(\theta)|^2, \quad (1.98)$$

which is related to the amplitude of the wavefunction at large distances (r)(Ω is the solid angle element). The ansatz of the scattering solution is usually taken to be

$$\Psi(\vec{r}) = e^{ikz} + \frac{A(\theta)e^{ikr}}{r}. \quad (1.99)$$

This ansatz can be understood as being a superposition of an unperturbed part related to the incoming wave and a outgoing spherical scattered wave. It is easy to see that such wavefunction has a flux through an element of area $dS = r^2 \sin(\theta)d\theta$ given by [38] $|\frac{A(\theta)}{r}|^2$, resulting in a DCS given by Equation 1.98.

The partial wave expansion is a standard method to solve the quantum scattering problem. In this method the wavefunction $\Psi(\vec{r})$ is expanded in terms of Legendre polynomials

$$\Psi(\vec{r}) = \frac{1}{r} \sum_{l=0}^{\infty} c_l \psi_l(r) P_l(\cos \theta) \quad (1.100)$$

where c_l are expansion coefficients, $\psi_l(r)$ are the solutions to the radial only problem at a fixed angular momentum l (partial waves), and $P_l(\cos \theta)$ are the Legendre polynomials. The functions $\psi_l(r)$ have to satisfy the radial equation for all l , i.e.

$$\left[\frac{d^2}{d^2r} + k^2 - \frac{2m}{\hbar^2} V(r) - \frac{l(l+1)}{r^2} \right] \psi(r)_l = 0 \quad (1.101)$$

The solution for the partial waves can be found by considering the solution of the radial Schrödinger equation in the limit $r \rightarrow \infty$ [38]. For potentials that decay faster than $\frac{1}{r}$ the asymptotic solution for the radial Schrödinger equation converges to the free particle solution given by

$$\Psi(\vec{r}) \rightarrow A_l \frac{1}{r} \sum_{l=0}^{\infty} B_l [e^{-i(kr-l\pi/2)} - e^{i(kr-l\pi/2)}] P_l(\cos \theta), \quad (1.102)$$

with the difference between the solutions without or with the potential given by the different boundary conditions at small r (actually at $r = 0$). It is possible to show that in the latter case the influence of the potential changes only the relative phase of the outgoing wave when compared to the free particle solution. The general solution for the partial waves in the asymptotic region is given by

$$\Psi(\vec{r}) \rightarrow A_l \frac{1}{r} \sum_{l=0}^{\infty} B_l [e^{-i(kr-l\pi/2)} - e^{i(kr-l\pi/2)} e^{i2\delta_l}] P_l(\cos \theta), \quad (1.103)$$

where all the influence of the potential is included in the phase shift term $e^{i2\delta}$. The latter equation has a more familiar form given by

$$\Psi(\vec{r}) \rightarrow A_l \frac{1}{r} \sin(kr - l\frac{\pi}{2} + \delta_l). \quad (1.104)$$

The overall normalization constant for the solution is not of interest in this case. Instead, by expanding Equation 1.99 in terms of partial waves, using

$$e^{ikz} = \frac{1}{r} \sum_{l=0}^{\infty} i^l (2l+1) P_l(\cos \theta) \quad (1.105)$$

and comparing with Equation 1.103 we can obtain an expression for the scattering amplitude [39]

$$A(\theta) = \frac{1}{2ik} \sum_{l=0}^{\infty} (2l+1) (e^{2i\delta_l} - 1) P_l(\cos \theta), \quad (1.106)$$

where we used the expansion given in Equation 1.103 and the orthogonality relation for the Legendre polynomials.

The relationship between the quantum result and semiclassical theory can be brought out by considering the expression for the phase shift in the JWKB (Jeffreys-Wentzel-Kramers-Brioullin) theory [38]. Consider the JWKB approximation to the central potential problem (Eqn. 1.101) in the classical region

$$\Psi(\vec{r}) = \frac{1}{(k_l(r))^{\frac{1}{2}}} \sin \left[\int_{a_l}^r k_l(r) dr + \frac{\pi}{4} \right], \quad (1.107)$$

with a_l the classical turning point and were we use

$$k_l(r) = k^2 - \frac{V(r)}{2m} - \frac{(l + \frac{1}{2})^2}{r^2}. \quad (1.108)$$

Direct comparison between the JWKB solution and Equation 1.102 suggests that the JWKB phase shift is given by

$$\delta_l = \frac{\pi}{2} \left(l + \frac{1}{2} \right) + \int_{a_l}^{\infty} (k_l(r) - kr) dr \quad (1.109)$$

Equation 1.109 has a more explicit form as

$$\delta_l = \int_{a_l}^{\infty} k_l(r) dr - \int_{(l+\frac{1}{2})/k}^{\infty} k_l(r, V(r) = 0) dr. \quad (1.110)$$

By considering the derivative of the phase shift w.r.t $L = (l + \frac{1}{2})$ we obtain

$$\frac{\partial \delta_l}{\partial L} = \int_{L/k}^{\infty} \frac{L}{[k^2 - L^2/r^2]^{1/2}} dr - \int_{a_l}^{\infty} \frac{L}{[k^2 - V(r)/2m - L^2/r^2]^{1/2}} dr. \quad (1.111)$$

Then substituting the classical variables given by

$$L = \left(l + \frac{1}{2} \right) \hbar = m v b = k \hbar b, \quad (1.112)$$

$$E = \frac{k^2 \hbar^2}{2m}, \quad (1.113)$$

we obtain

$$\frac{\partial \delta_l}{\partial L} = \frac{\pi}{2} - b \int_{a_l}^{\infty} \frac{1}{r^2 [1 - V(r)/E - b^2/r^2]^{\frac{1}{2}}} dr. \quad (1.114)$$

Equation 1.114 is exactly $\frac{1}{2}$ of the classical deflection function [37]. Noting that the variation in L is equivalent to a variation in θ through the collision momentum

and the deflection function we arrive at the relationship

$$\frac{\partial \delta_l}{\partial \theta} = \frac{1}{2} \Theta(b). \quad (1.115)$$

The relationship given by Equation 1.115 is of great importance for correcting results obtained with the END theory when the need arises. By knowing the classical deflection function and its relation to the semiclassical solution for the elastic scattering problem, semiclassical DCS can be computed via Equation 1.106 from purely classical deflection functions. It is important to note that the deflection function (and resulting phase shift) as used in the END theory do include inelastic processes and presents a generalization over the JWKB results as presented in this section. Most importantly, deflection functions calculated by the END method can introduce effects of excited electronic states that are fundamental for the description of charge transfer scattering processes.

1.5 Measurements

Equation 1.116 gives the velocity dependent rate constant in terms of the reaction cross section for a process R

$$k(v) = v\sigma_R(v). \quad (1.116)$$

The attenuation of an incident beam in the x direction due to process R for a $A + B$ collision is given by

$$-\frac{dI}{dx} = k(v)n_A n_B = I(x)n_B \sigma_R(v), \quad (1.117)$$

where $I(x)$ is the incident flux in the x direction and $n_{A/B}$ is the number density for particle A/B . The reactive cross sections therefore determine the microscopic rate for the reaction. Temperature dependent reaction rates can be constructed by convoluting a Maxwell-Boltzmann velocity distribution with $\sigma_R(v)$.

The opacity function is a theoretical quantity that can also help with mechanism interpretation. It is defined in terms of the cross section derivative w.r.t the impact parameter as

$$P(b) = \frac{1}{2\pi b} \frac{d\sigma_R}{db}, \quad (1.118)$$

and it gives the fraction of reactive collisions for a given impact parameter b .

The reaction cross section can be given as a weighted average over the opacity function:

$$\sigma_R = \int_0^{\infty} 2\pi b P(b) db. \quad (1.119)$$

1.5.1 Total Cross Section Calculation

The integral cross section can also be calculated by integrating over the initial conditions provided that we know the opacity function for the process of interest. The integral cross section is defined by

$$\sigma_k(E_{Lab}) = 2\pi \int_0^{\infty} b P_k(b; E_{Lab}) db. \quad (1.120)$$

To calculate the opacity function $P_k(b, E_{Lab})$ we have to average over the many initial orientations possible for a non spherical target, i.e.,

$$P_k(b, E_{Lab}) = \frac{1}{8\pi^2} \int_0^{2\pi} \int_0^{2\pi} \int_0^{\pi} p_k(\alpha, \beta, \gamma, b) \sin \beta d\alpha d\beta d\gamma, \quad (1.121)$$

where the function $p_k(\alpha, \beta, \gamma, b)$ is the reaction or charge transfer probability defined for channel k for a single trajectory calculation. The trajectory initial condition is specified by the target orientation labeled by angles α, β and γ and by an impact parameter b . If the projectile is not spherically symmetric one needs to introduce it's orientation average in the probability function. This approach is

sufficient if we are interested in total cross sections only. Product angular distributions (DCS) are not explicitly considered in this analysis.

In order to evaluate the average integral numerically, we need to consider $p_k(\alpha, \beta, \gamma, b)$ a smooth function of its parameters and construct a polynomial interpolation for the probability function over the angular variables. From that point we do a numerical integration to compute the integral. Consider the trapezoidal rule

$$\int_0^{2\pi} f(x)dx = \sum_{i=0}^{n-1} h_i f(x_i), \quad (1.122)$$

where we used $f(0) = f(2\pi)$. This integration implies zero order expansion for the integrand, therefore any available value in the interval can be used to compute the integral.

To compute the integral in β some care has to be taken as the weight function goes to zero for $\beta = 0$ and $\beta = \pi$. One solution is to evaluate the integral in β analytically. Using a first order expansion for the integrand function we have

$$\int_0^{2\pi} f(\beta) \sin \beta d\beta = \int_0^{2\pi} \bar{f}(\beta) \sin \beta d\beta, \quad (1.123)$$

where

$$\bar{f}(\beta) = f_i + h_i(\beta - \beta_i)(f_{i+1} + f_i), \quad (1.124)$$

and $h_i = (\beta_{i+1} - \beta_i)$. Substituting in Equation 1.123 we obtain

$$\begin{aligned} \int_{\beta_i}^{\beta_{i+1}} \bar{f}(\beta) \sin \beta d\beta &= -f_i(h_i\beta_i \cos \beta_{i+1} + \cos \beta_i + \cos \beta_{i+1} - h_i\beta_{i+1} \cos \beta_i) \\ &\quad + \beta_{i+1} + h_i \sin \beta_{i+1} - h_i f_i \sin \beta_i + f_{i+1}(h_i \sin \beta_{i+1} \\ &\quad - h_i\beta_{i+1} \cos \beta_{i+1} + h_i\beta_i \cos \beta_{i+1} - h_i \sin \beta_i) \end{aligned} \quad (1.125)$$

This procedure is used throughout this work to compute total cross sections for the several reactions studied.

1.5.2 Background on Guided Ion Beam Experiments

The absolute cross sections for the abstraction and exchange channels NDH_3^+ and NDH_2^+ in the reactive collision $NH_3^+ \rightarrow D_2$ are measured using a guided ion beam (GIB) apparatus [40, 41, 42]. These experiments are best suited for measuring ion-molecule reactions at hyper-thermal energies such as the one considered in this work. The main distinction between these experiments from the traditional crossed beam experiments is that the former can measure total cross sections but due to experimental design cannot measure product angular distributions. The final result of such experiments are time-of-flight (TOF) profiles that show ion count (intensity) versus time. The TOF profiles are integrated producing the total intensity. Branching ratios are obtained as the fraction of summed intensity in a particular product channel. Relative cross sections are the ratio of a product intensity over the reactant intensity. In addition, this methodology allows for the measurement of product ion laboratory velocity parallel to the incoming beam. Typical absolute errors for total cross sections measured in this scheme are in the 30% range while relative errors are smaller [41].

The special features that the GIB setup shares with the crossed beam experiments are [43] as follows,

- Single collisions provided that the pressure is low enough.
- Reactants are velocity (energy) selected.
- Supersonic nozzle expansion guarantees that reactant molecules have low temperature.
- Reactants can be state selected by use of electric, magnetic or laser fields (by coupling lasers to the setup).
- Reactants can be oriented and polarized to study steric effects.

And unlike most crossed beam experiments, absolute cross sections are measured.

Schematics of the GIB apparatus are pictured in the Figure 1.5.2 from Dressler [41]. The experimental setup is divided into

- An ion source generator.
- An octopole ion guide responsible for selecting the ion's collision energy and guiding the beam to the reaction chamber. A quadrupole mass filter can be used to mass select the reactant ions before they enter into the octopole ion guide.
- A field free collision chamber filled with the second reactant.
- A second octopole ion guide responsible for collecting the nascent product.
- The detection part with a quadrupole mass filter.

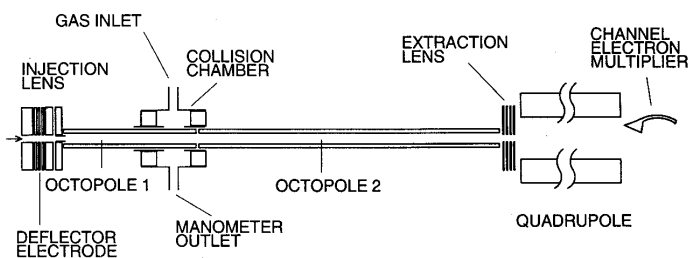


Figure 1.3: Pictorial representation of the interaction region of the guided ion beam experiment.

Some improvements of the GIB experiment by Poutsma [44] over the Quadrupole Tandem Mass Spectrometer (QTMS) setup used by Morrison [45] are

- The octopole guide would better control the divergence of the slow particles.
- The second octopole better collects both forward and side scattered products than a quadrupole guide of TMS setups.

The net result is that GIB experiments with octopole guides have better sensitivity than Quadrupole guided TMS experiments.

The GIB apparatus can be combined with a resonance-enhanced multiphoton ionization (REMPI) operating on the ion source to select the initial vibrational state of the reactant ion. By first electronically exciting the system to a state of

similar nuclear configuration as the ion (usually a Rydberg state) and later ionizing the excited molecule, REMPI is capable of producing vibrationally excited ions at selected vibrational states. In the case of ammonia the \tilde{C}' can be used as it has a planar nuclear configuration like the ion. Note that this technique is used also to generate ground state NH_3^+ molecules when the $\Delta\nu = 0$ transition is targeted.

CHAPTER 2
THE $NH_3^+ + D_2$ SYSTEM AT HYPERTHERMAL ENERGIES

2.1 Introduction

Our research involves the theoretical study of reactive scattering processes. More specifically we have been studying the reaction of NH_3^+ with D_2 at hyperthermal energies. Poutsma [44] and coworkers recently investigated this reaction in a molecular beam study providing experimental results in the form of relative cross sections for the two most important channels, the abstraction channel ($NH_3D^+ + D$) and the exchange channel ($NH_2D^+ + D + H$).

The NH_3^+ with D_2/H_2 reaction presents serious challenges for both experiment and theory. It is amenable enough for experimental investigation but exhibits non-Arrhenius temperature dependence of the reaction rate at low temperatures and two competing channels at higher collision energies that have strong dependence on NH_3^+ internal excitation. Moreover the $NH_3^+ + H_2$ reaction is believed to have some importance in the interstellar synthesis of ammonia. In this work we investigate the $NH_3^+ + D_2$ reaction at hyper thermal collision energies ranging from 6 to 16 eV in the center of mass (COM).

This chapter is divided in four sections and one appendix. Section 2.2 provides some background information about guided ion beam experiments and a brief review of experimental results for the reaction of interest whose initial conditions closely relate to the ones used in our calculations. Emphasis is placed on experiments performed by R. N. Zare's group. Section 2.3 presents a few theoretical results for electronic structure calculations for the NH_5^+ molecule and also presents the initial conditions grid and basis functions used for our cross section

calculations. Sections 2.4 presents results for total cross section, differential cross section and flux-velocity contour plots at collision energies of 6, 8, 12 and 16 eV in the center of mass frame. Sections 2.5 and 2.6 present the discussion conclusions respectively.

2.2 Experimental Results for Reaction $NH_3^+ + D_2$

Two investigations performed at R. N. Zare's group explore the $NH_3^+ + D_2$ reaction at collision energies ranging from 0.5 to 10 eV in the COM. In the earlier study Morisson et al. [45] utilize a TMS setup with quadrupole ion guides and considers initially excited NH_3^+ ions in the umbrella bending mode with $\nu_2 = 0-9$. The highest excited state corresponds to an internal energy of 1.1 eV. In the more recent study Poutsma et al. [44] use a GIB setup and considers two almost isoenergetic vibrational states as well as the ground vibrational state of the ion. The two excited states considered are the $\nu_1\nu_2 = 1^02^5$ and $\nu_1\nu_2 = 1^12^2$ where ν_1 corresponds to the symmetric stretching mode and ν_2 corresponds to the umbrella bending mode. The excited vibrational states 1^02^5 1^12^2 and have 0.60 and 0.63 eV of internal energy respectively.

The main interest of both studies is to gain insight into the mechanism of the reaction by considering several initial conditions with different energy components (vibrational,kinetic). By studying the energy flow from reactants to products one hopes to gain insight into the mechanisms of the generation of the exchange and abstraction products and their interrelationship.

At the experimental conditions considered the two main channels present for the reaction are:



and



or the equivalent for the present experiment



Even though GIB experiments can provide results for total cross sections, only relative cross sections were reported. Due to its design the sensitivity of the experiment depends on the kinetic energy of the ion source, i.e. sensitivity is collision energy and nascent product kinetic energy dependent. The result is that preferential detection of a particular product can occur if the channels differ markedly in final kinetic energy. The mentioned experimental weakness w.r.t sensitivity is not as pronounced for the newer GIB setup as compared to the older quadrupole guide TMS experiment but still seem to be an issue for the reaction under study.

The kinematics of the system guarantees that the products are forward scattered in the LAB frame, however for isotropically scattered products the collection efficiency for the GIB setup is only 10%. Therefore depending on the mechanism in operation and the resulting angular distribution, the collection efficiency can be different for the different reaction channels.

Another consideration is that the experiment measures the *long time limit* for the abstraction and exchange cross sections. With a traveling time of 40 to 50 μs from the reaction chamber to the detector, excited state nascent products can further react or dissociate and substantially affect cross section values. Energy spread for the COM collision energies seem to be well under control and reported to be of 0.2 eV in the COM or 1 eV in the laboratory frame.

The main qualitative experimental insight from Zare's work can be summarized as: channel (I) was found to be very sensitive to increase in collision energy while channel (II)/(III) was found to be very sensitive to increase in vibration excitation at collision energies above 4 eV in the COM.

Others have reached similar conclusions while studying the same reaction system under different initial conditions. Following Eisele et al. [46], Morrison suggests that the formation of the exchange product happens through a two step process with (I) followed by (IV). More recently another alternate mechanism was suggested by Poutsma (V). Winniczek et al. [47] explored reactions (I) and (II)/(III) using a cross ion beam setup. The experiment used a fixed collision energy of 0.5 eV in the COM and vibrationally excited ammonia cations with energies ranging from 3.3 to 4.9 eV. Winniczek found that excess vibrational energy appears in the product final kinetic energy and that the abstraction reaction proceeds through a direct rebound mechanism (not spectator stripping) while exchange proceeds through the formation of a long lived complex. Winniczek suggests that for the low collision energy considered in the experiment formation of the exchange product is not due to a two step process having the abstraction product as an intermediate, but rather due to the formation of a weakly bound complex. RRKM estimates suggest a lifetime consistent with a well depth of 0.2-0.7 eV relative to the reactants. In his work Winniczek suggests that this energy is compatible with a $NH_3^+ \cdot D_2$ complex and much less than the binding energy for the complex $NH_3D^+ \cdot D$. However more recent theoretical calculations [48] suggests that complex $NH_3D^+ \cdot D$ has a binding energy of 0.85 eV while complex $NH_3^+ \cdot D_2$ has a binding energy of only 0.06 eV when compared to reactants. Ischtwan et al. [49] also suggests a possible reaction coordinate cutting through extrema points of the $NH_3D_2^+$ potential surface, without the formation of a $NH_3D^+ \cdot D$ complex, but with an internal NH_4^+ rotation w.r.t the hydrogen that would lead to the exchange channel (II). Therefore, as opposed to what Winniczek claims, the dynamics of exchange and abstraction processes may not be so dramatically different.

Kemper and Bowers [50] considered COM collision energies in the 0.07-1 eV range and vibrational excitations in the 1-5 eV range in a tandem ICR (ion cyclotron resonance) experiment. Although operating in a rather different collision regime his conclusions are similar to Zare's: kinetic energy enhances (I) while vibrational energy enhances (II)/(III). Bowers suggest that the exchange reaction proceeds through a combination of direct and complex formation mechanisms while the abstraction reaction proceeds through a direct mechanism at higher temperatures (above 200-300 K). Low temperature experiments [51] suggests a low reaction barrier of 0.09 eV at the entrance channel for the abstraction reaction.

In Section 2.2 we introduce the *spectator stripping* model used by Zare's group to explain some of the experimental results. Though simple, the model can help connect results obtained in the experiments with results obtained by theoretical calculations. We make use of some of its results in the next paragraph.

An important threshold energy for the present study is the dissociation energy for the process



and an equivalent process for the loss of a D atom. The accepted threshold value for such process is 5.5 eV. Using the spectator stripping model we can predict at what collision energy we could have the formation of NH_2D^+ as a two step process of reaction (I) followed by reaction (IV). Assuming reactants initially in their ground state and using $\Delta H_{rxn} = 1.04$ eV the predicted value for the COM collision energy necessary for the production of NH_2D^+ from dissociation of NH_3D^+ is 8.0 eV in the COM. In other words, for collision energies above 8.0 eV we should see an increase in NH_2D^+ formation due to the opening of a new reaction channel.



Results presented by Zare’s group [45, 44] seem to corroborate the two step mechanism and spectator stripping model with two facts:

- There is an insensitivity of the cross section to a particular vibrational mode being excited.
- There is a steep increase in channel (II)(III) products at collision energies above 8 eV in the COM concomitant with a depletion of channel (I).

Two of the best accepted limiting mechanisms for a direct reaction (faster than the rotation of the formed reaction complex) are the *spectator stripping* mechanism and the *rebound* mechanism. In the rebound mechanism the reaction occurs at small values of the impact parameter b and products are back scattered in the COM frame. Cross sections are usually small due to the small range of reactive impact parameters. In this section we will describe the second limiting mechanism, the *spectator stripping*, model in detail.

The spectator stripping model is known to give reasonable estimates for internal energy deposition in product fragments for collision energies above 1 eV. The model assumptions are rather crude but it can help to shed some light on the reaction mechanism of the abstraction channel and its relationship to the exchange channel for the title reaction.

In the spectator stripping model the projectile NH_3^+ picks a D atom while the other D acts as a spectator. The main assumption of the model is that the spectator D and the reactant fragment NH_3^+ do not change momentum during the collision. With that assumption of momentum conservation one can derive the internal energy being deposited in the abstraction product NH_3D^+ . In this model the product NH_3D^+ velocity is given by (v is the original relative velocity)

$$m_{NH_3D^+}u = \frac{m_{NH_3^+}m_{D_2}}{M}v - \frac{m_Dm_{NH_3^+}}{M}v \quad (2.1)$$

$$= \frac{m_{NH_3^+}(m_{D_2} - m_D)v}{M} \quad (2.2)$$

where M is the total mass. Energy conservation under these conditions takes the form (ΔH_{rxn} being the energy liberated during the reaction) :

$$\frac{m_{NH_3^+}m_{D_2}v^2}{2M} + E_0^{int} = \frac{m_{NH_3D^+}m_Dv'^2}{2M} + \Delta H_{rxn} + E^{int}. \quad (2.3)$$

where we can use the fact that the new relative velocity is given by $v' = u - \frac{m_{NH_3^+}}{M}v$

$$E^{int} = \frac{m_{NH_3^+}}{2M} \frac{(m_{D_2}m_{NH_3D^+} - m_Dm_{NH_3^+})}{m_{NH_3D^+}} v^2 - \Delta H_{rxn} + E_0^{int}. \quad (2.4)$$

Equation 2.4 can be rewritten in a more useful form as

$$E^{int} = E_{coll.}^{com} \frac{(m_{D_2}m_{NH_3D^+} - m_Dm_{NH_3^+})}{m_{D_2}m_{NH_3D^+}} - \Delta H_{rxn} + E_0^{int} \quad (2.5)$$

or numerically

$$E^{int} = E_{coll.}^{com} * 0.5526 + \Delta H_{rxn} + E_0^{int}. \quad (2.6)$$

The values predicted by the spectator stripping model for collision energies considered in our simulations are given in Table 2.1.

2.3 Computational Details

2.3.1 Structures at Extrema Points of the NH_5^+ Potential

Early calculations involving characterization of NH_5^+ ground state structure were performed by Bugaets and Zhogolev [52] and by Kassab et al. [53]. Ischtwan [48] did a more comprehensive study of the NH_5^+ electronic potential surface with calculation of several minima and transition states. Large changes in energy were

observed when going from double zeta valence basis to a triple zeta valence basis function and small changes in energy when diffuse functions on the N were added. Results seem to be insensitive to the presence of polarization functions on the hydrogen.

Table 2.1: Predicted values for internal energy and relative kinetic energy by the spectator stripping model. The $E_{exp.}^{int.}$ estimate uses the experimental value $\Delta H_{rxn} = 1.04$ while $E_{theo.}^{int.}$ uses $\Delta H_{rxn} = 0.78$.

$E^{coll.}/eV$	$E_{exp.}^{int.}/eV$	$E_{theo.}^{int.}/eV$	$E^{kin.}/eV$
6	4.35	4.09	2.68
8	5.46	5.20	3.76
12	7.67	7.41	5.36
16	9.88	9.62	7.16

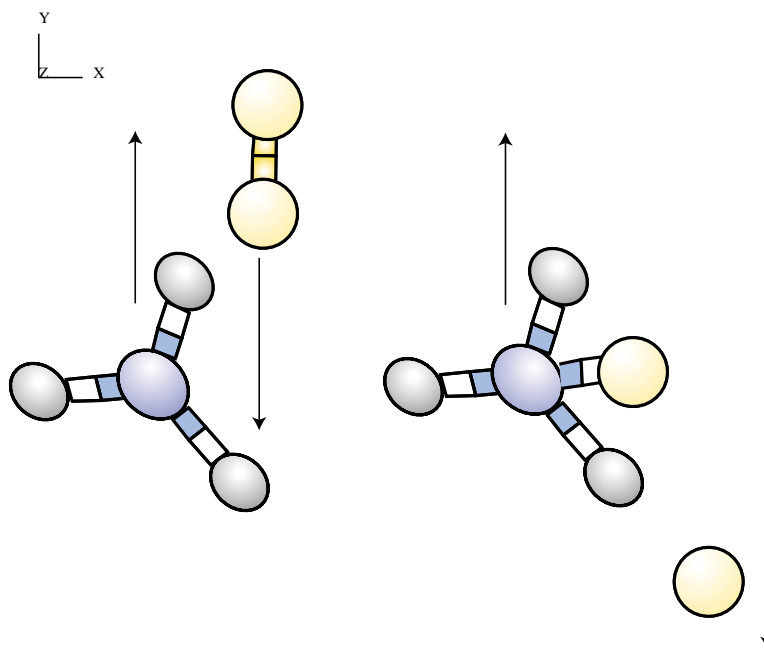


Figure 2.1: Spectator stripping model illustration for the $(NH_3^+) + D_2$ reaction.

In our simulations we employ a double zeta basis with polarization functions namely 6-311G* for nitrogen and 6-311 for hydrogen/deuterium (corresponding to (11s,5p,1d):[4s,3p,1d] on nitrogen and (5s):[3s] on hydrogen/deuterium and is referred here as N:6-311G*/H:6-311G). Other basis were also considered for the study: N:6-311G*/H:6-311G*, DZP, PVDZ and 6-31G.

Effects of electronic correlation on extrema structures and energies are sizable but do not change the principal features of the potential surface. The largest effect among the structures considered by Ischtwan [48] was on the transition state (TS) for the abstraction process. Using MP4 as the correlated method this structure corresponds to an activation barrier of 0.28 eV, while in Hartree Fock (HF) the barrier is 0.67 eV.

Discussion of reaction mechanism at hyper-thermal collision energies is not as straight forward as at lower, thermal, collision energies. At thermal collisions one expect the low energy path, sometimes referred as the reaction path, to dominate and a single mechanism can be suggested for a reaction. Transition state theory can be used to rationalize changes in transition state energy and geometry with changes in the reaction rate. For hyper-thermal energies there is no unique path, as reactive trajectories explore a much grater region of the potential. Extrema structures however (transition states (TS) and minima) can still help to interpret trajectories according to limiting cases.

Additional complexity is added at hyper thermal collision energies due to the possibility of electronic excitations during or after the reactive collision process. Electronic excitation can change not only the final energy partition but the outcome of the reaction process itself. We don't expect electronic excitation related to the charge transfer channel to play an important role during the initial approach for the $NH_3^+ + D_2$ reaction. Electronic excited states are usually important to describe charge transfer processes and can influence reactive channels as well, however, in our case the charge transfer channel ($NH_3^+ + D_2^+$) is very high in energy. Electronic excitation is allowed in our simulation and often happens shortly after a reactive encounter when the product molecule vibrates violently. As a consequence some

non negligible amount of energy can flow to electronic degrees of freedom. A more detailed discussion about this topic is presented in the discussion section.

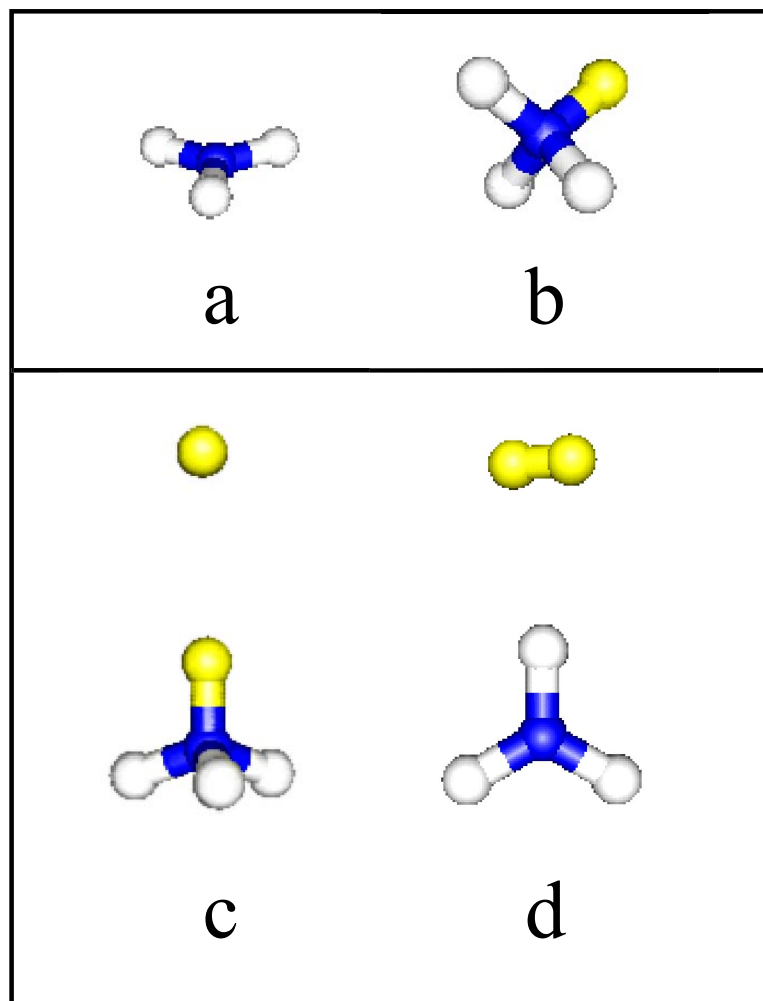


Figure 2.2: Minima structures for reactants products and complexes.

In Figure 2.2 we show the structure of some minima's for the Hartree Fock potential surface. Structures **a** and **b** are for reactant and product while **c** and **d** are minima structures along the abstraction reaction path. Figure 2.3 shows transition states (TS) found for the Hartree Fock potential surface. The relative energy differences between structure **a** in Figure 2.2 and structures in Figures 2.2 and 2.3 are given in Table 2.2 and 2.3. E_{diss} is the the D_2 dissociation energy.

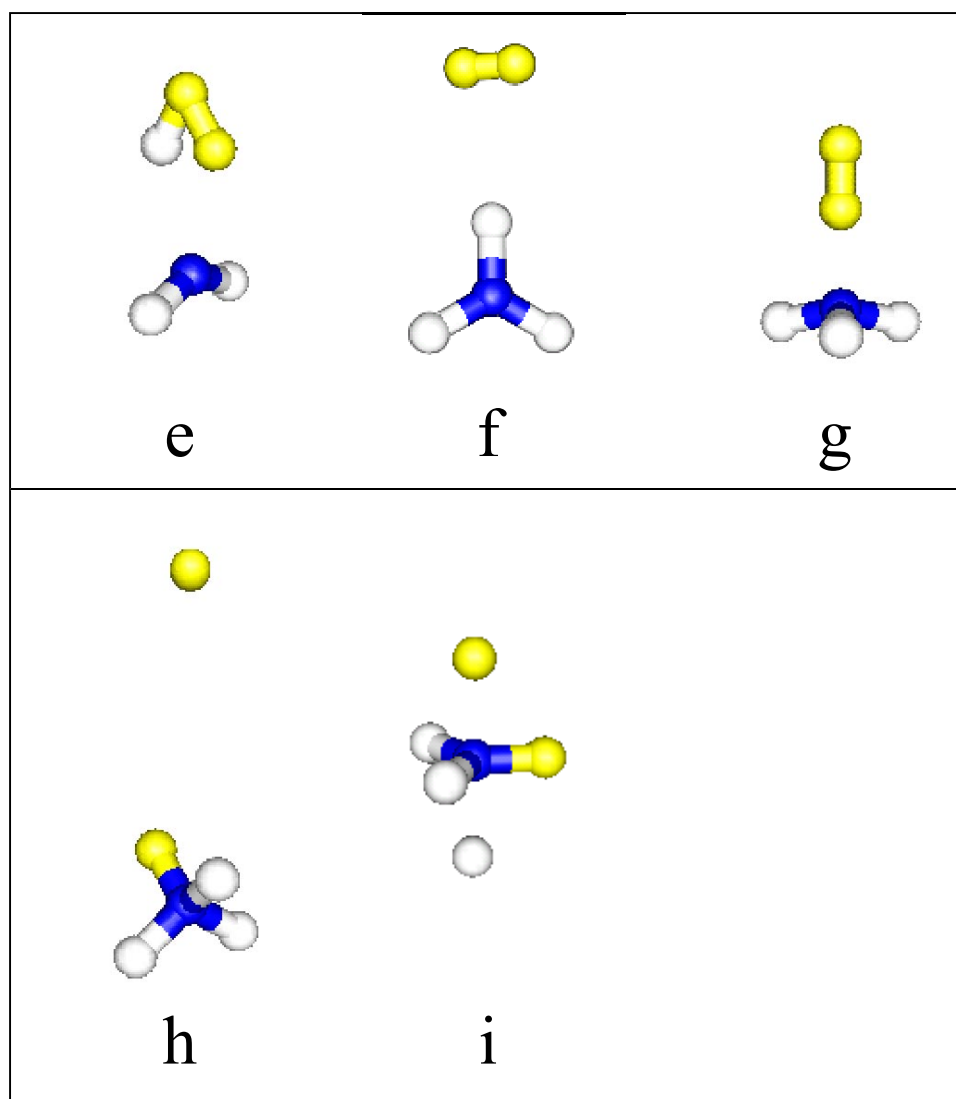


Figure 2.3: Transition state structures along abstraction (**f,g**) and exchange (**e, i** and **h**) reaction paths.

Among the TS structures, **f** and **g** lead to the abstraction product while **e**, **i** and **h** lead to the exchange product.

Table 2.2: Energies differences relative to reactants (structure **a**) and structures given in Figure 2.2 in eV. B_1 is a N:6-311G*, H:6-311 basis; B_2 is a DZP basis with polarization only on N.

Basis	E_a/eV	E_b/eV	E_c/eV	E_d/eV
B_1	0	- 0.779	-0.696	0.065
B_2	0	-0.768	-0.786	-0.039

Table 2.3: Energies differences relative to reactants (structure **a** in Figure 2.2) and structures given in Figure 2.3 in eV. B_1 is a N:6-311G*, H:6-311 basis; B_2 is a DZP basis with polarization only on N.

Basis	E_e/eV	E_f/eV	E_g/eV	E_h/eV	E_i/eV	E_{diss}/eV
B_1	2.881	-0.065	0.629	-0.680	2.613	3.553
B_2	-	-0.039	0.954	-0.776	2.527	3.557

2.3.2 Collision Grid and Initial Conditions

Often during the dynamics of reactive trajectories we observe structures similar to the ones pictures in Figures 2.2 and 2.3. Reactive trajectories at collision energies used in this simulation however can explore a much more diverse range of structures then the extrema ones pictured in Figures 2.2 and 2.3. Our initial condition grid has to be general enough to explore the whole possibilities of reactive trajectories at all collision energies as it is very hard to anticipate how the dynamics will progress. For the experiment in question there is no orientation preference on either reactants consequently an average over initial orientations is necessary for comparison between theoretical and experimental results.

The grid of initial conditions used to compute the cross sections has 10 unique orientations for the target NH_3^+ and 3 unique orientations for the projectile (one

along the C_3 symmetry axis of NH_3^+ , and two other orientations perpendicular to it). The total number of unique orientations considered is therefore 30. We considered impact parameters ranging from 0 to a maximum around 3 *a.u.* (typically we only run 6 impact parameters per orientation) with steps of 0.4 *a.u.* The total number of trajectories needed to generate a cross section is around 200. As mentioned in the previous section we used a 6-311G* basis for the nitrogen and a 6-311G basis for the hydrogen and deuterium. Figure 2.5 shows the initial NH_3^+ orientations while Figure 2.4 shows the initial D_2 orientations used in our simulations. The NH_3^+ orientations are generated by rotations parametrized according to Euler angles α , β and γ . An example of a collision configuration is pictured in Figure 2.6.

Orientation on the D_2 grid can be classified according to similarities with structures from Figures 2.2 and 2.3. Trajectories starting from orientation 1 (axial) can reach TS **g** in Figure 2.3, with the external D atom leaving in the backward scattering direction (in the laboratory frame). One can say without much questioning that structures similar to **g** are important for reactive processes having a rebound mechanism. Trajectories starting from orientation 3 (eclipsed) form a molecular complex with structure similar to **g** but with the D_2 rotated 90 degrees and allow for the external D atom to leave in the forward direction. Orientation 3 also allows for initial configurations that have D_2 and NH bonds being initially eclipsed and for configurations similar to **e**, **f** and **i**. Trajectories starting from orientation 2 (staggered) can explore regions of the configuration space similar to **e**, **f** and **i** as well as some unusual configurations, e.g. with D_2 and NH bonds being initially staggered at 90 degrees.

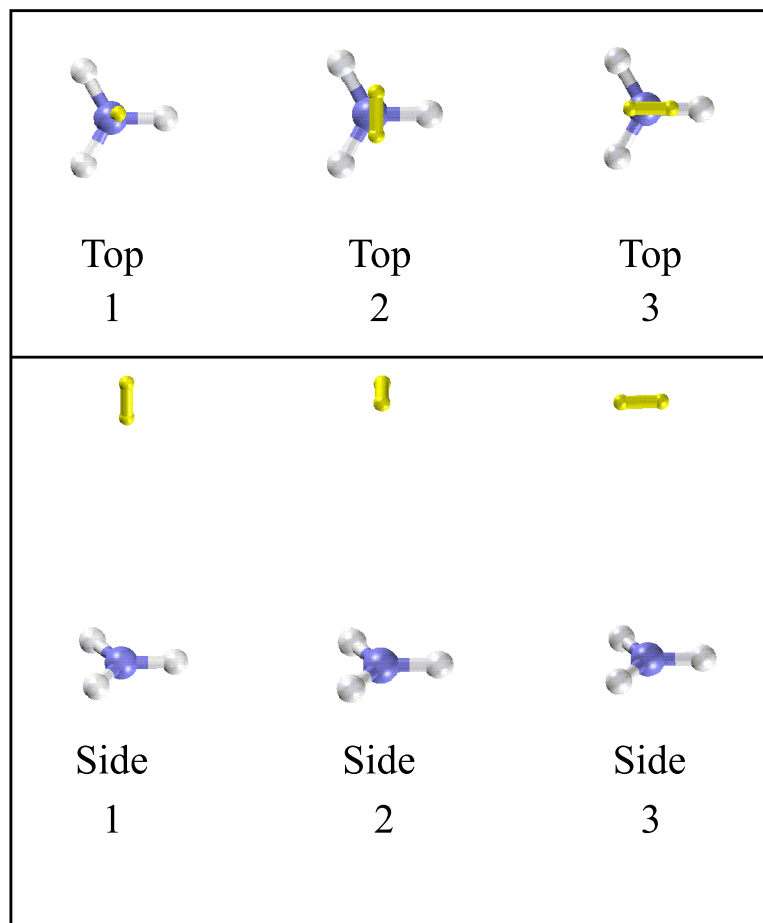


Figure 2.4: Initial D_2 orientations used in the cross section calculations.

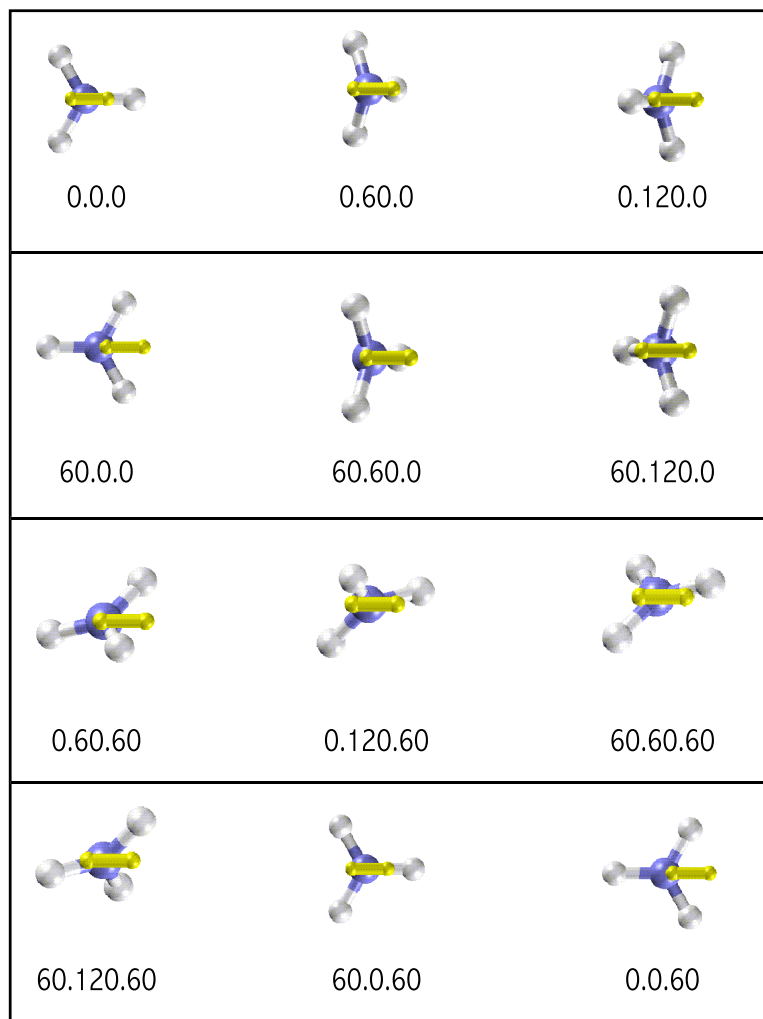


Figure 2.5: Initial NH_3^+ orientations used in cross section calculation. The first 10 displayed orientations are unique. Orientations are labeled by Euler angles α , β and γ .

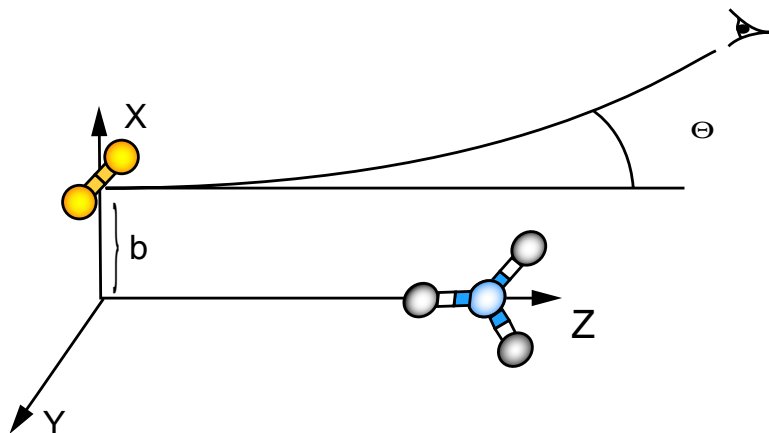


Figure 2.6: Example of collision configuration picturing the impact parameter b and the laboratory scattering angle θ .

2.4 Results

For the problem at hand we are interested in the reactive cross section for channels (I) and (III). As it turns out, channel (II) was not important for the energies considered in the simulation. As mentioned before, cross beam experiments can provide flux dependent angular distributions. Experimental differential cross sections can be measured and provide more detailed information about reaction mechanism. GIB experiments can also provide some angular distribution information by measuring the velocity vector along the propagation direction of the octopole guide. If final velocities are also measured, cross beam raw experimental data can be represented in terms of intensity contour maps or *flux-velocity* distributions [43]. Flux-velocity distributions can be used as a tool by both theory and experiment as a probe for the mechanism in action as idealized mechanisms provide distinctive profiles in flux-velocity plots. Collision complexes formation produces flux-velocity plots that are symmetric w.r.t to forward/backward scattering direction. A rebound mechanism produces a *flux-velocity* plot having pronounced intensity over angles $\simeq 180$ while a reaction following the spectator stripping model produces mostly forward scattering with defined final momentum.

The particular procedure we use for calculating the total cross section is discussed in Chapter 1 Section 1.5.1. Results for cross sections at four different energies are given in table 2.4.

From this point on experimental results referred in the text correspond to results from Poutsma et al. [45] and Morrison et al. [44] unless otherwise stated. Because the experimental flux was reported as a percentage of the total flux and the flux is proportional to the cross section, Table 2.4 shows experimental results normalized to the total theoretical cross section.

The primary fact one appreciates is that the same experimental trend is observed on the theoretical results: abstraction reaches a maximum and then decay with collision energy while exchange always increase with collision energy. However, our results overestimate abstraction cross sections and underestimate exchange cross sections. The abstraction cross section maximum is reached at a higher collision energy then in the experiment, 8 eV vs. the experimental value of 6 eV.

Table 2.4: Total cross sections for abstraction and exchange. Experimental values are calculated as a percentage of the theoretical total reactive cross section.

E_{COM}^{coll}/ev	σ_{exch}/a_0^2	$\sigma_{abst.}/a_0^2$	$\sigma_{exch}^{exp}/a_0^2$	$\sigma_{abst}^{exp}/a_0^2$
6	0	5.38	0.62	4.86
8	0.14	6.46	2.42	4.15
12	1.57	4.34	na	na
16	2.25	3.92	na	na

Table 2.5 contains results for the total cross section divided according to the different contributions arising from the D_2 grid (Figure 2.4). There are numerous important results one can read from the partial cross section results in Table 2.5. So all the trajectories with orientation 1 (axial) averaged over all orientations of

NH_3^+ are labeled by superscript 1, and similarly for orientations 2 (staggered) and 3 (eclipsed). The following is a list of important features obtained from Table 2.5:

- At 6 eV of collision energy there is no exchange and abstraction comes from contributions for D_2 orientations 1 and 3 only. Note that although orientation 1 leads to trajectories that can reach TS **g** in Figure 2.3, orientation 3 is the one that contributes most for the total cross section. This is true for all energies considered.
- Contributions from orientation 1 show an intriguing behavior for the abstraction reaction being basically constant between 6 and 8 eV, dropping at 12 eV then increasing again at 16 eV.
- Results for orientation 3 do not change much between 6 and 12 eV but drop dramatically at 16 eV. Maximum contribution to abstraction cross section from this orientation and maximum integral reactive cross section are reached at 8 eV. This happens because different parts of the NH_3^+ grid are reactive at different collision energies.
- Direct exchange threshold is close to 8 eV of collision energy. Exchange integral cross section picks up at 12 eV with the contributions coming from orientation 3 being the most important.

Table 2.5: Breakdown of the total cross sections for abstraction and exchange in terms of D_2 initial collision orientation. Labels refer to D_2 orientations as pictured in Figure 2.4.

E_{COM}^{coll}/eV	σ_{exch}^1/a_0	σ_{exch}^2/a_0	σ_{exch}^3/a_0	$\sigma_{abst.}^1/a_0$	$\sigma_{abst.}^2/a_0$	$\sigma_{abst.}^3/a_0$
6	0	0	0	1.68	0	3.71
8	0.094	0.0	0.049	1.710	0.716	4.010
12	0.516	0.288	0.765	0.132	0.716	3.497
16	0.449	0.721	1.075	1.724	0.232	1.967

2.4.1 Detailed Results for Collision at 6 eV

For this collision energy the spectator stripping model (SSM) predicts the kinetic energy loss into internal excitation to be 3.31 eV (see Table 2.1) for the abstraction reaction (reaction (I)). When compared to the computed values from the END simulations, shown in Figure 2.8-a and Table 2.6, the SSM value is a good estimate for the average. The computed distribution is nevertheless broad with values ranging from 0.2 to 5 eV. The broadening is expected as trajectories that do not strictly follow the SSM have different momentum for outgoing D atom and as a result different internal excitations.

Average values for the kinetic energy transfer contribution to the internal excitation as well as kinetic contribution of SSM estimates are given in Table 2.6. The SSM predictions for the kinetic energy contribution to the internal excitation agrees well with the average value computed from ENDyne trajectories. As expected at higher energies the SSM estimate compares well with the value computed from trajectories with D_2 initially in the eclipsed orientation 3. Most important, the agreement between the SSM and END computed values validates the analysis of Morrison et al. [54] based on estimates for the internal excitation of NH_3D^+ . In particular this is so because he considered the SSM estimate to be the average internal excitation. SSM based predictions helped explain the lack of mode specificity of the title reaction.

Again if we analyze our results in terms of contributions coming from different parts of the D_2 grid (Figure 2.4) a much more interesting picture emerges. Figure 2.8-a shows two peaks, one at higher energy coming from D_2 orientation 1 pictured in Figure 2.8-b and another one at lower energy coming from D_2 orientation 3 pictured in Figure 2.8-d. There is consequently a very strong dependence in product internal excitation with the particular reactive collision configuration. Chemically

Table 2.6: Average internal excitation from kinetic energy transfer, given in eV, from simulation results. Labels 1, 2 and 3 refer to D_2 orientations as pictured in Figure 2.4. Also included are the results predicted by the SSM model in eV for kinetic energy transfer.

E_{COM}^{coll}/eV	E_{ave}	E_{ave}^1	E_{ave}^2	E_{ave}^3	E_{SSM}^{kin}
6	2.67	4.03	4.23	1.77	3.31
8	3.92	5.56	4.32	2.89	4.42
12	5.77	8.78	7.62	4.82	6.63
16	7.44	7.16	9.63	7.52	8.84

this conveys that orientations 1 and 3 have different reaction mechanisms. Orientation 1 exhibit a rebound type mechanism with a large amount of kinetic energy loss to internal excitation while orientation 3 display a mechanism more according to the SSM. Deviations from the SSM occur because the outgoing D and the newly formed NH_3D^+ interact. As the $D + NH_3D^+$ potential is mostly repulsive the SSM predicted value is an upper estimate for the energy loss to internal excitation for the reaction. This generalization of the SSM mechanism is called the *spectator stripping recoil* mechanism (SSR).

Table 2.7: Average scattering angle ($\theta_{com.}$), given in Radians, from simulation results. Labels 1, 2 and 3 refer to D_2 orientations as pictured in Figure 2.4

E_{COM}^{coll}/eV	θ_{ave}	θ_{ave}^1	θ_{ave}^2	θ_{ave}^3
6	1.94	2.58	1.76	1.53
8	1.94	2.55	2.27	1.50
12	1.43	1.87	1.84	1.25
16	1.15	1.38	1.5	0.82

A chief attribute from Figure 2.8 is that all reactive trajectories from orientation 1 have internal energy above the dissociation threshold for reaction (IV). Hence, theory supports that formation of the abstraction product, reaction (III), at this collision energy can be due to the opening of a new channel given by (V). The predicted threshold value by the SSM model in Section 2.2 is 8 eV COM. Actual simulation results place this value somewhat below 6 eV as trajectories that can

undergo dissociation have a rebound type mechanism resulting in a greater than SSM kinetic energy loss to internal excitation. The experimental threshold for the exchange reaction seems to be around 4.5 eV of collision energy COM.

As shown in Table 2.4, there is no direct formation of the exchange product NH_2D^+ at this collision energy and orientation 2 only leads to one reactive trajectory.

Figure 2.7 shows the *flux velocity* distribution as a contour map of trajectories count. The polar variables are the final NH_3D^+ kinetic energy and the scattering angle in the COM frame. Here again, the distinct differences between trajectories starting with orientation 1 and 3 can be seen. Figure 2.7-b shows slow backward scattered products while Figure 2.7-d shows products scattered at a higher velocity and with scattering angle peaked around 90° . A histogram of the CM scattering angle is pictured in Figure 2.9 and also displays a two peak profile. Orientation 1 produces a larger, closer to 180° degrees scattering angle, while orientation 3 produces a peak around 90° degrees.

2.4.2 Detailed Results for Collision at 8 eV

Increasing the collision energy to 8 eV COM results in a few changes on internal energy excitation histograms and flux velocity plots. For D_2 orientation 1, Figures 2.10-b, 2.11-b as well as Tables 2.6 and 2.7 indicate that an increase in collision energy resulted in an increase almost solely of internal excitation. D_2 orientation 3 shows an increase in both internal excitation and exit product velocity. The significant result at 8 eV is the appearance of contributions coming from D_2 orientation 2.

As one might expect, a much larger fraction of trajectories contains internal excitation above the threshold limit. At 8 eV of collision energy a substantial

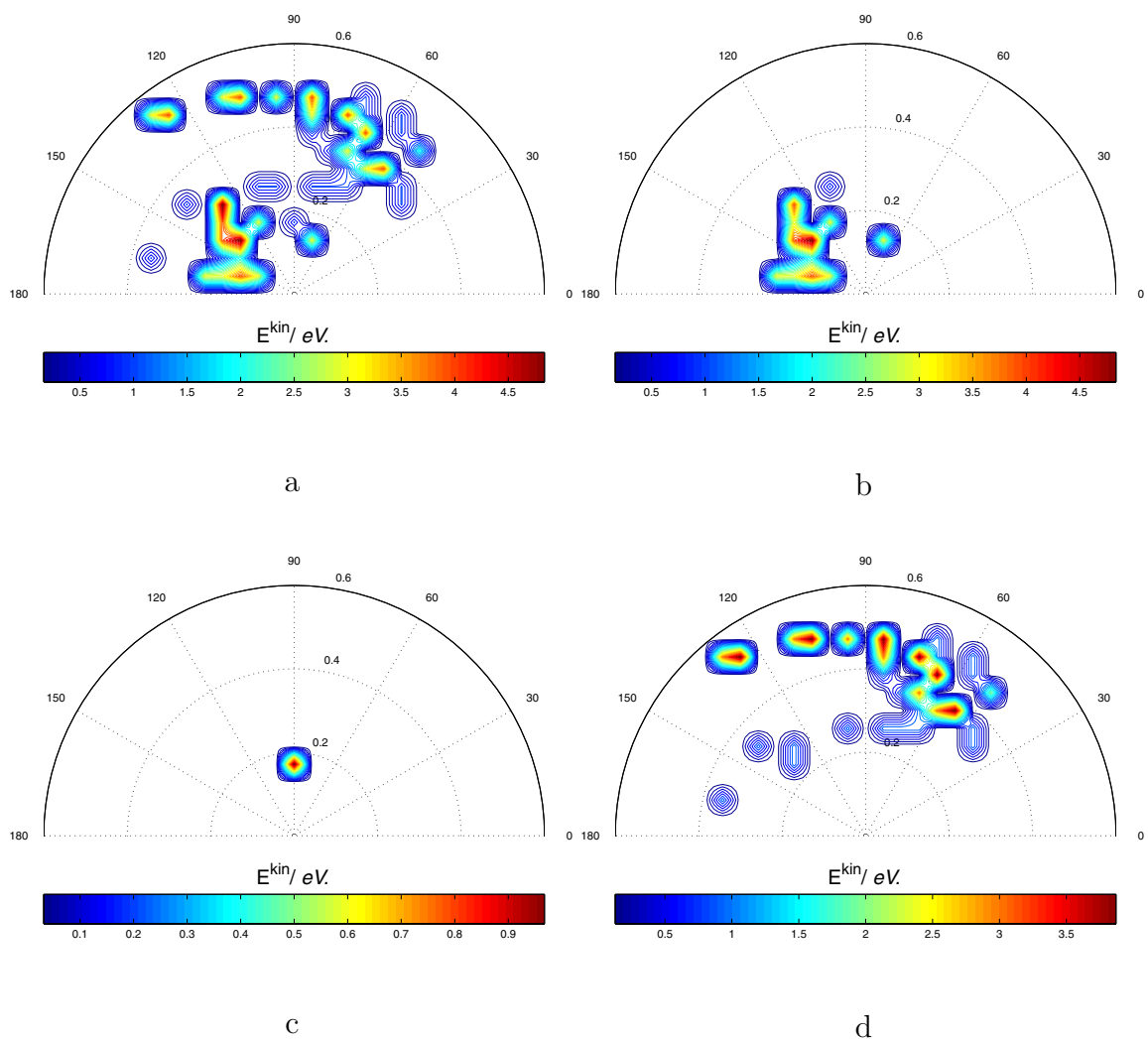


Figure 2.7: Flux velocity contour map for the abstraction product using a collision energy in the COM of 6 eV. We have clockwise: a) total flux; b) a partial of the grid with D_2 orientation label 1, c) same with orientation 2; d) same with orientation 3. The radial dimension is the final kinetic energy in the COM (eV) and colors label the histogram count.

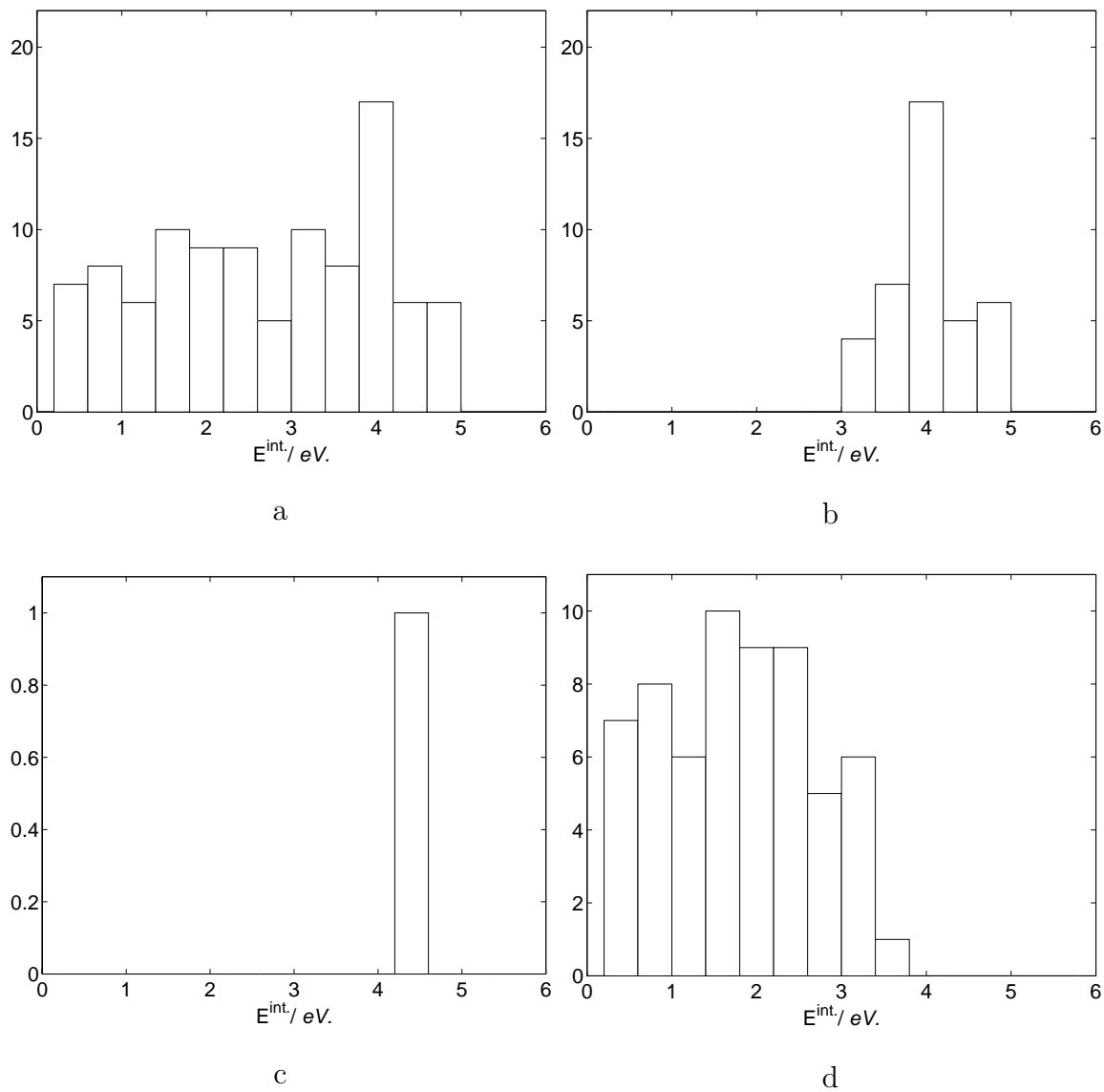


Figure 2.8: Histograms for internal energy transferred during the collision for the abstraction product using a collision energy in the COM of 6 eV. We have clockwise: a) total histogram; b) a partial of the grid with D_2 orientation label 1, c) same with orientation 2; d) same with orientation 3.

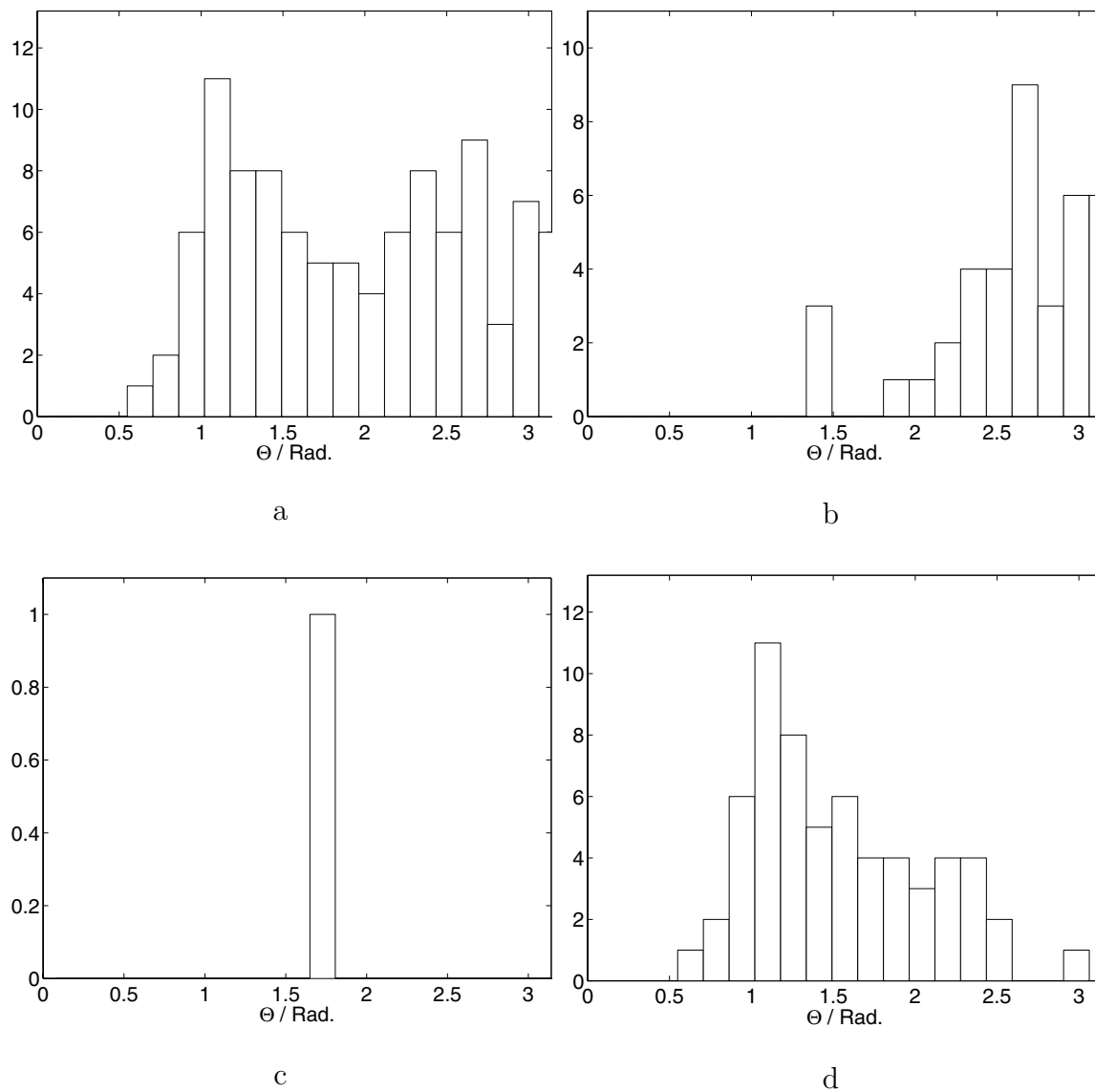


Figure 2.9: Angular distribution histograms for the abstraction product using a collision energy in the COM of 6 eV. We have clockwise: a) total histogram; b) a partial of the grid with D_2 orientation label 1, c) same with orientation 2; d) same with orientation 3.

fraction of trajectories from orientation set 2 and 3 have internal excitation above threshold for the new channel (V). Orientations 1 and 3 are clearly responsible for the two peak profile in Figure 2.11-a and 2.15-a. As in the 6 eV collision, trajectories with initial D_2 orientation 1 produces more internal excitation due to the rebound mechanism than trajectories with initial D_2 orientation 3. Trajectories with initial D_2 orientation 2 produces mostly backward scattered products with internal excitation in between orientations 1 and 3.

Mostly important at 8 eV is that the cross section for a direct exchange reaction, not due to a two step process terminated by reaction (V), is non zero as shown by Table 2.4. A direct exchange reaction mechanism is usually characterized by a billiard ball type collision in which a D atom ejects an H atom. A two step exchange mechanism is unlikely to be observed in our dynamics as the propagation time in our simulations is short, with propagation times ranging from 80 to 200 ps, and not long enough to allow for the dissociation of metastable NH_3D^+ molecules.

Scattering angle histograms continue to have a multi peak profile, with trajectories with D_2 initially at orientation 1 and 2 producing mostly back-scattered products while 3 produces a histogram peaked at less than 90° degrees. As in the 6 eV case, D_2 orientation 1 produce reactive trajectories through a rebound mechanism while D_2 orientation 3 produce reactive trajectories more according to the SSM. The predicted value by the SSM for kinetic energy loss to internal excitation overestimates, as in the 6 eV case, the computed number for most trajectories having initial D_2 given by orientation 3.

2.4.3 Detailed Results for Collision at 12 eV

At 12 eV of collision energy the picture is somewhat different than at 6 eV and 8 eV. The direct exchange cross section is large and D_2 orientation 1 produces

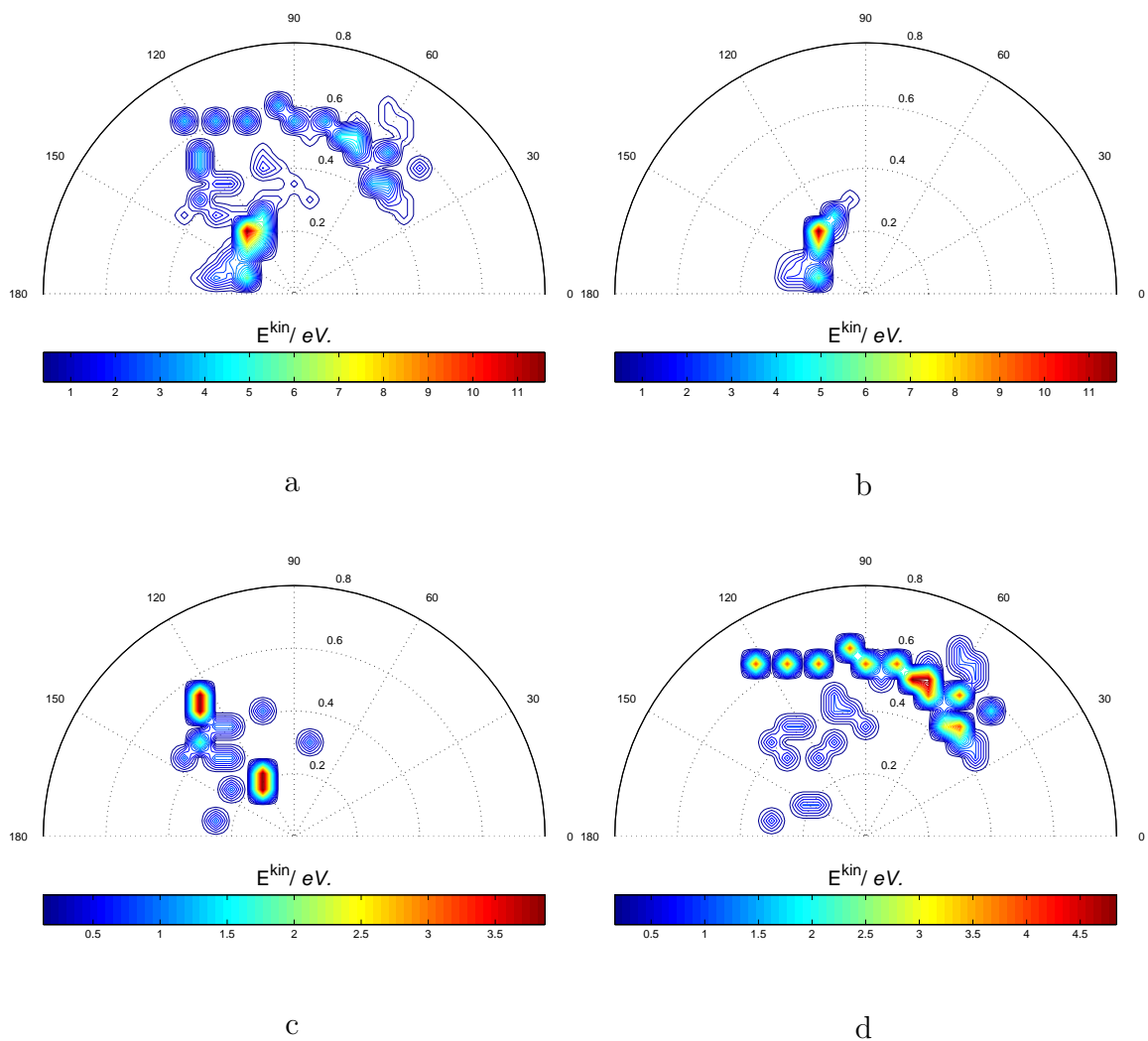


Figure 2.10: Flux velocity contour map for the abstraction product using a collision energy in the COM of 8 eV. We have clockwise: a) total flux; b) a partial of the grid with D_2 orientation label 1, c) same with orientation 2; d) same with orientation 3. The radial dimension is the final kinetic energy in the COM (eV) and colors label the histogram count.

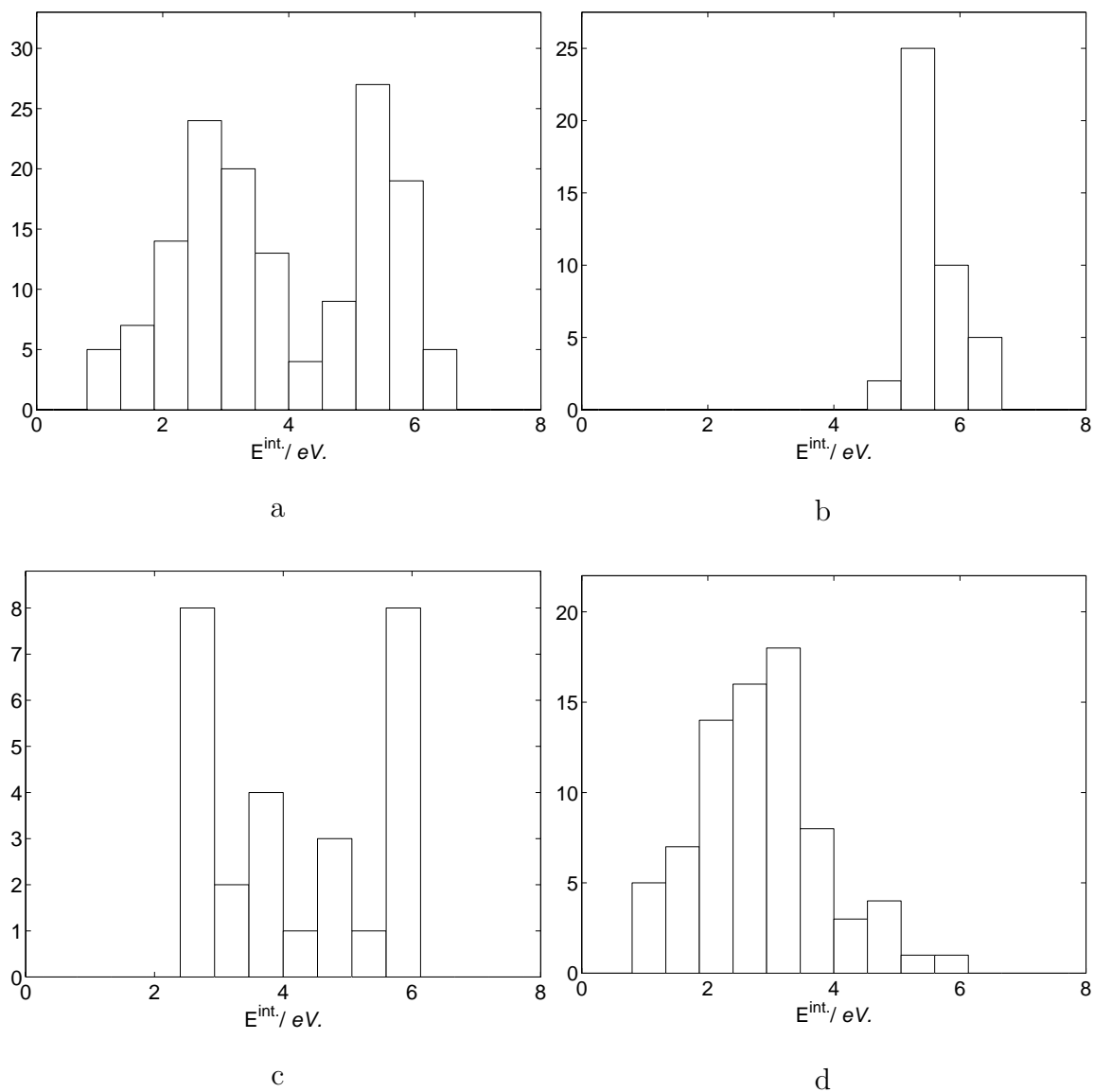


Figure 2.11: Histograms for internal energy transferred during the collision for the abstraction product using a collision energy in the COM of 8 eV. We have clockwise: a) total histogram; b) a partial of the grid with D_2 orientation label 1, c) same with orientation 2; d) same with orientation 3.

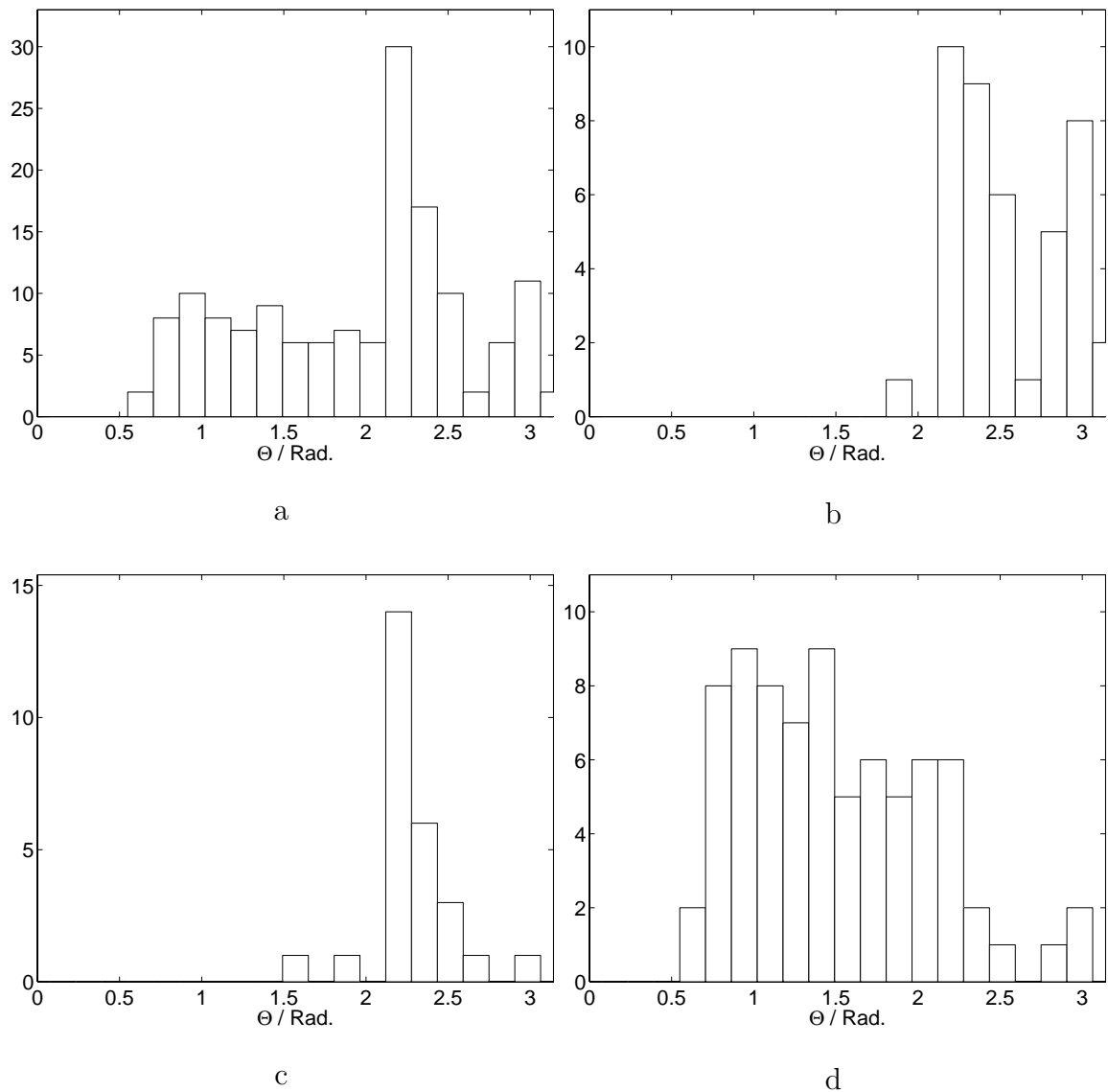


Figure 2.12: Angular distribution histograms for the abstraction product using a collision energy in the COM of 8 eV. We have clockwise: a) total histogram; b) a partial of the grid with D_2 orientation label 1, c) same with orientation 2; d) same 3.

very little abstraction product. Given the increase in internal excitation when going from 6 eV to 8 eV, trajectories with D_2 initial orientation given by 1 at 12 eV of collision energy seem to be unable even to form metastable NH_3D^+ in large numbers. A few reactive trajectories form a highly excited NH_3D^+ product (Figure 2.14-b).

As in the previous lower energy cases, the SSM prediction for kinetic energy loss to internal excitation for trajectories with D_2 initially at orientations 2 and 3 overestimates for most trajectories the computed values produced by the dynamics (see Figures 2.14-c and 2.14-d and Table 2.6). However, the theoretical computed distribution of internal excitation at 12 eV has several trajectories with internal excitation around and above the SSM prediction of 6.6 eV, specially from trajectories with D_2 initially at orientation 2 as pictured in Figure 2.14-c.

Figures 2.15-a through 2.15-d show that trajectories with D_2 initial orientation 1 show mostly backward scattering, consistent with a rebound mechanism, while orientation 3 shows a forward scattering peaked around 60° degrees. Trajectories with D_2 at initial orientation 2 shift to smaller values when compared to trajectories at 8 eV of collision energy and peak around 90° degrees. All angular information in addition to exit velocities is conveyed in the flux velocity plots (Figure 2.13). There it is clear to notice that an increase in 4eV of collision energy resulted in very little increase in the final exit velocity for the outgoing NH_3D^+ . Most excess energy went into internal excitation and D exit velocity. Because trajectories with D_2 initially at orientation 1 don't form the abstraction product in great numbers, the total flux is mostly forward scattered in the COM as shown in Figure 2.13-a.

In Figures 2.16 and 2.17 we present typical reactive trajectories for abstraction and exchange respectively at 12 eV of collision energy. The abstraction trajectory shown is very similar to other reactive trajectories at lower energies, while direct

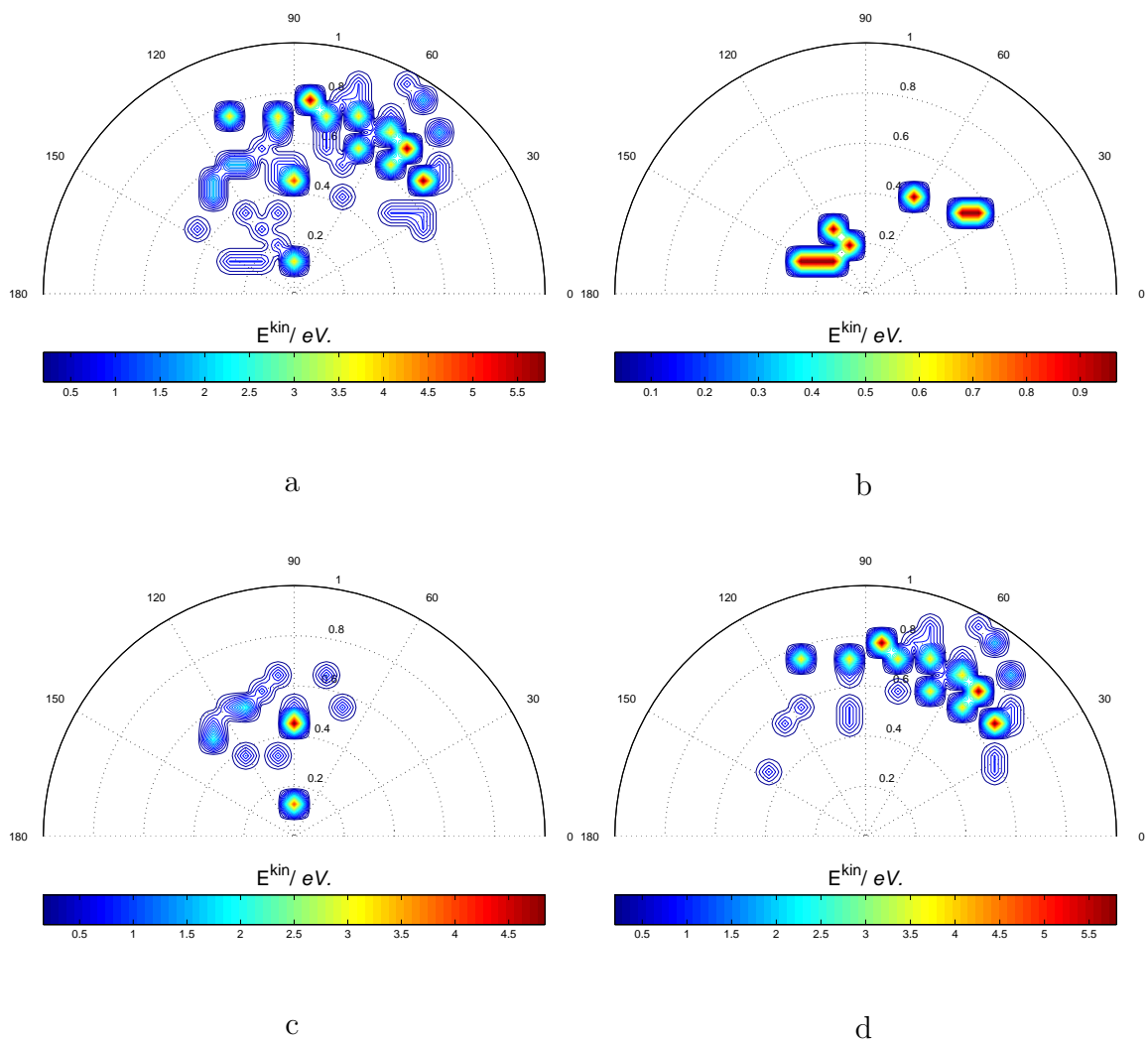


Figure 2.13: Flux velocity contour map for the abstraction product using a collision energy in the COM of 12 eV. We have clockwise: a) total flux; b) a partial of the grid with D_2 orientation label 1, c) same with orientation 2; d) same with orientation 3. The radial dimension is the final kinetic energy in the COM (eV) and colors label the histogram count.

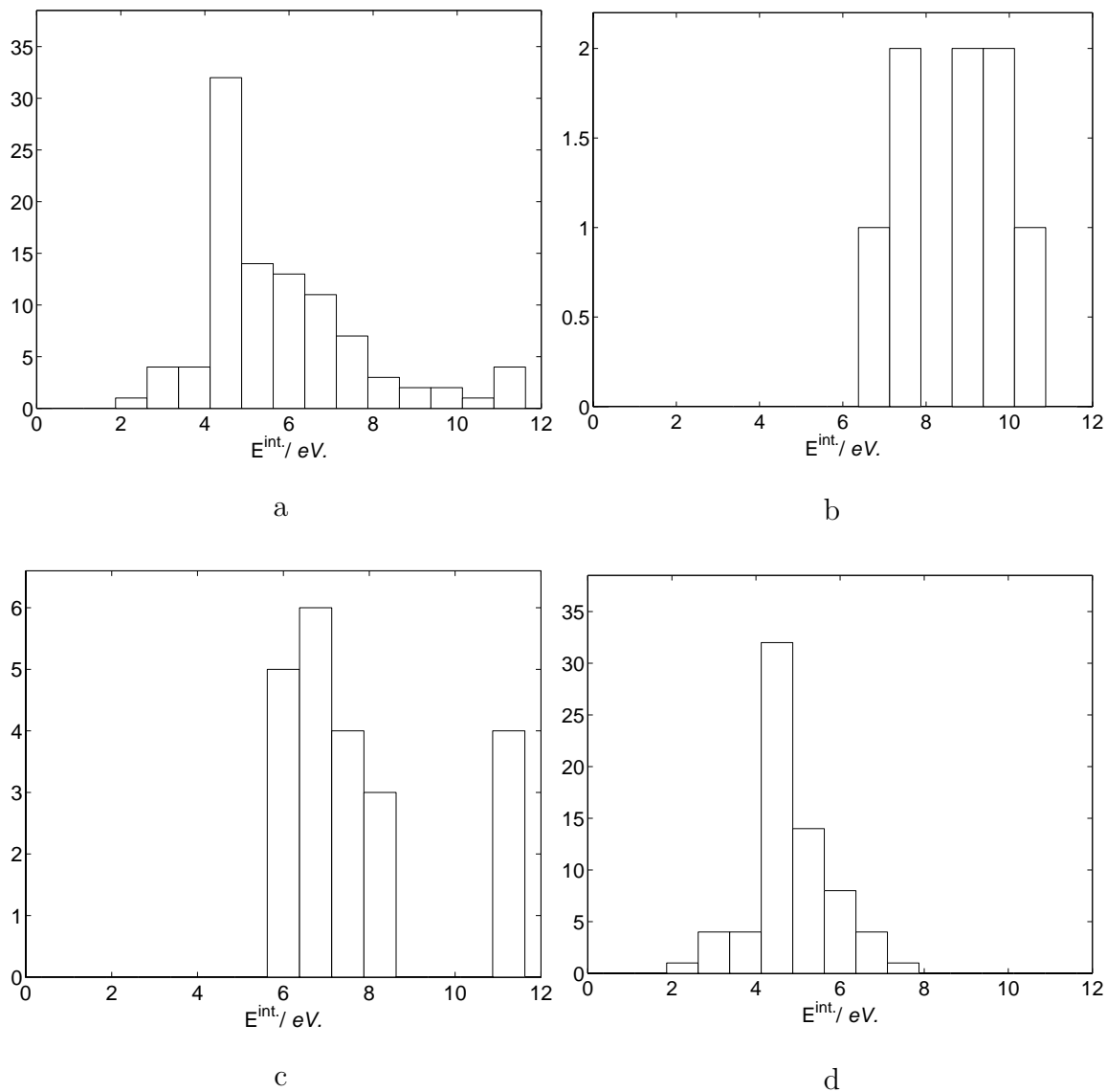


Figure 2.14: Histograms for internal energy transferred during the collision for the abstraction product using a collision energy in the COM of 12 eV. We have clockwise: a) total histogram; b) a partial of the grid with D_2 orientation label 1, c) same with orientation 2; d) same with orientation 3.

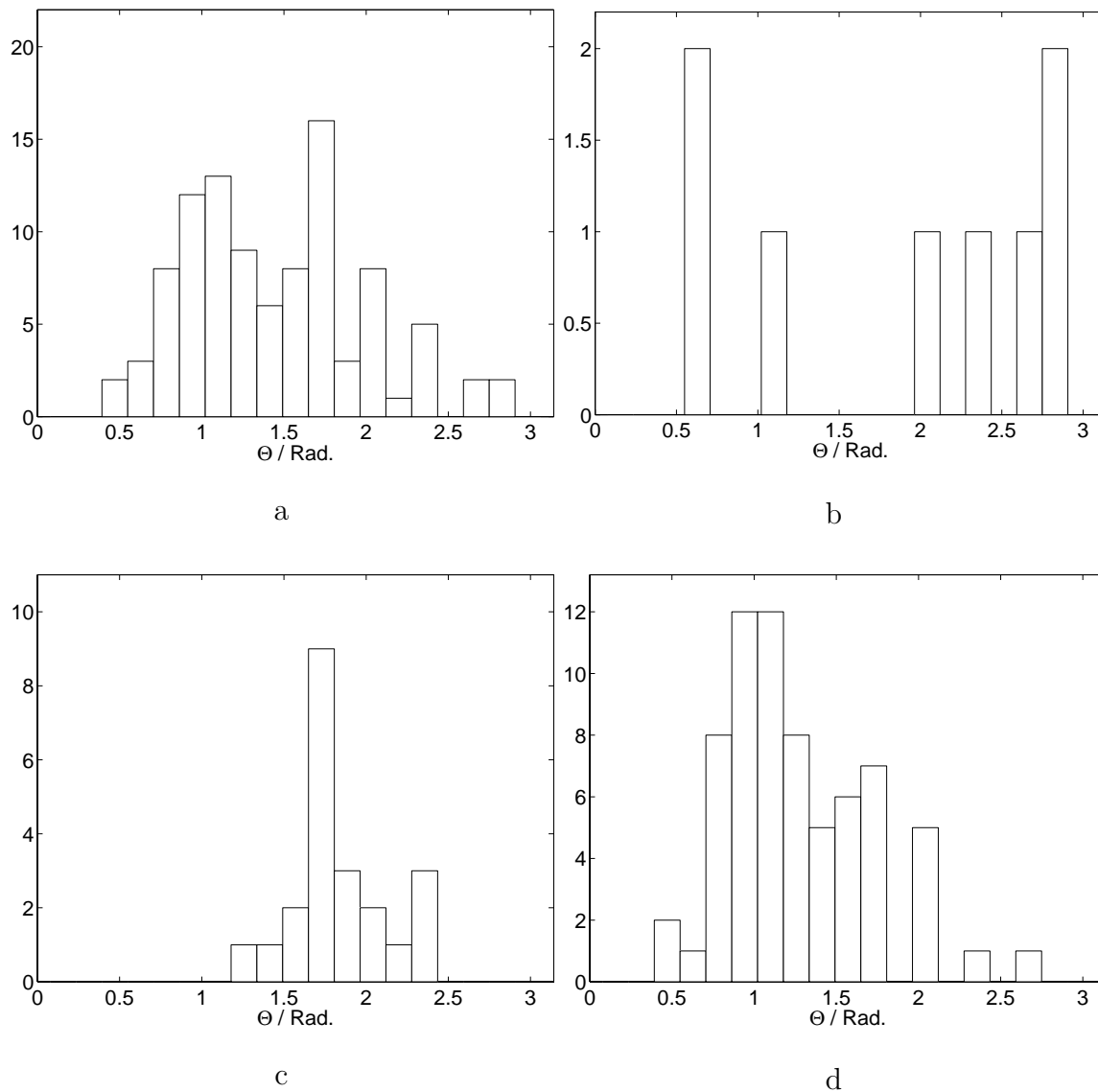


Figure 2.15: Angular distribution histograms for the abstraction product using a collision energy in the COM of 12 eV. We have clockwise: a) total histogram; b) a partial of the grid with D_2 orientation label 1, c) same with orientation 2; d) same with orientation 3.

abstraction reactions are only common at 12 eV and 16 eV. Mulliken population plot for the abstraction trajectory (Figure 2.16) shows that after the reactive encounter and breakage of the D_2 bond, the system is so excited that during the first oscillation of the newly formed $N-D$ bond a species with a biradical character is formed. However, shortly after 1500 a.u. of time the energy is redistributed over other vibrational and electronic modes leading to the formation of a metastable NH_3D^+ species. For the exchange channel the Mulliken population plot shows an adiabatic process corresponding to direct exchange reaction.

2.4.4 Detailed Results for Collision at 16 eV

At the highest collision energy investigated in this work, 16 eV, there is enough energy that the dynamics can explore a new set of reactive NH_3^+ orientations having initial axial D_2 configuration (1). As opposed to what happens at 6 eV and 8 eV, the axial orientation at 16 eV does not lead to a rebound mechanism (see Figures 2.20 table 2.7 for the average scattering angle). Most important, at this energy the staggered (3) orientation that at lower energies contributes most to the abstraction cross section is substantially reduced. Several trajectories form NH_3D^+ for a very short time but the excess of internal excitation does not allow for product formation. This shows that saturation of the abstraction channel for the direct process is occurring at the 16 eV collision energy.

At 16 eV of collision energy the SSM prediction also overestimate the computed values for kinetic energy loss. However, when compared to the prior estimates at lower collision energies, the computed value by the SSM is not far off. Average values for the kinetic energy loss and scattering angle shown in Tables 2.6 and 2.7 indicate that at this energy the SSM is a good approximation for the reaction

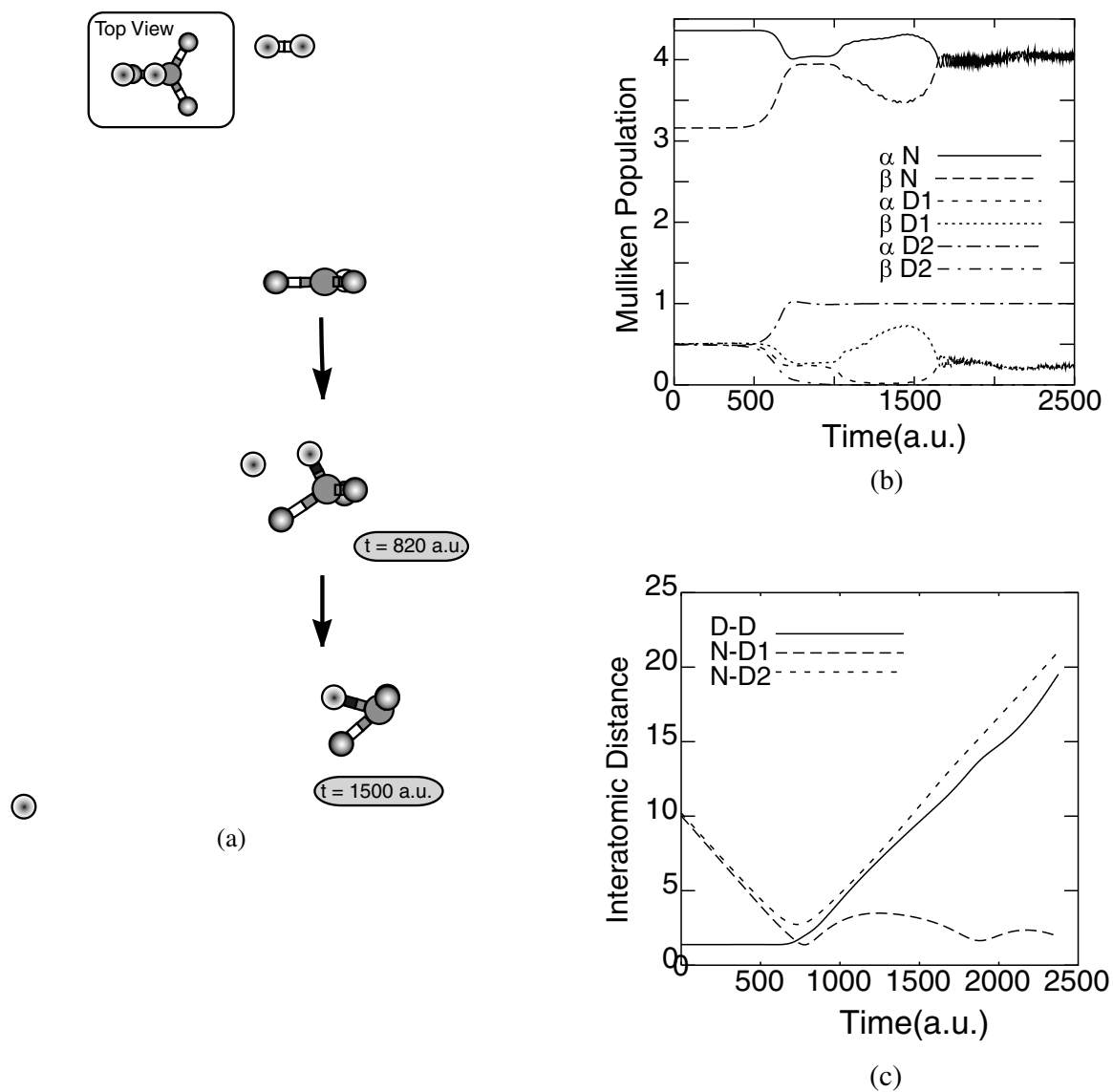


Figure 2.16: Typical END trajectory of $D_2 + NH_3^+$ with a D_2 initial eclipsed (3) orientation leading to abstraction. Time-evolution of atomic charges and interatomic distances. The collision energy for the trajectory was 12 eV.

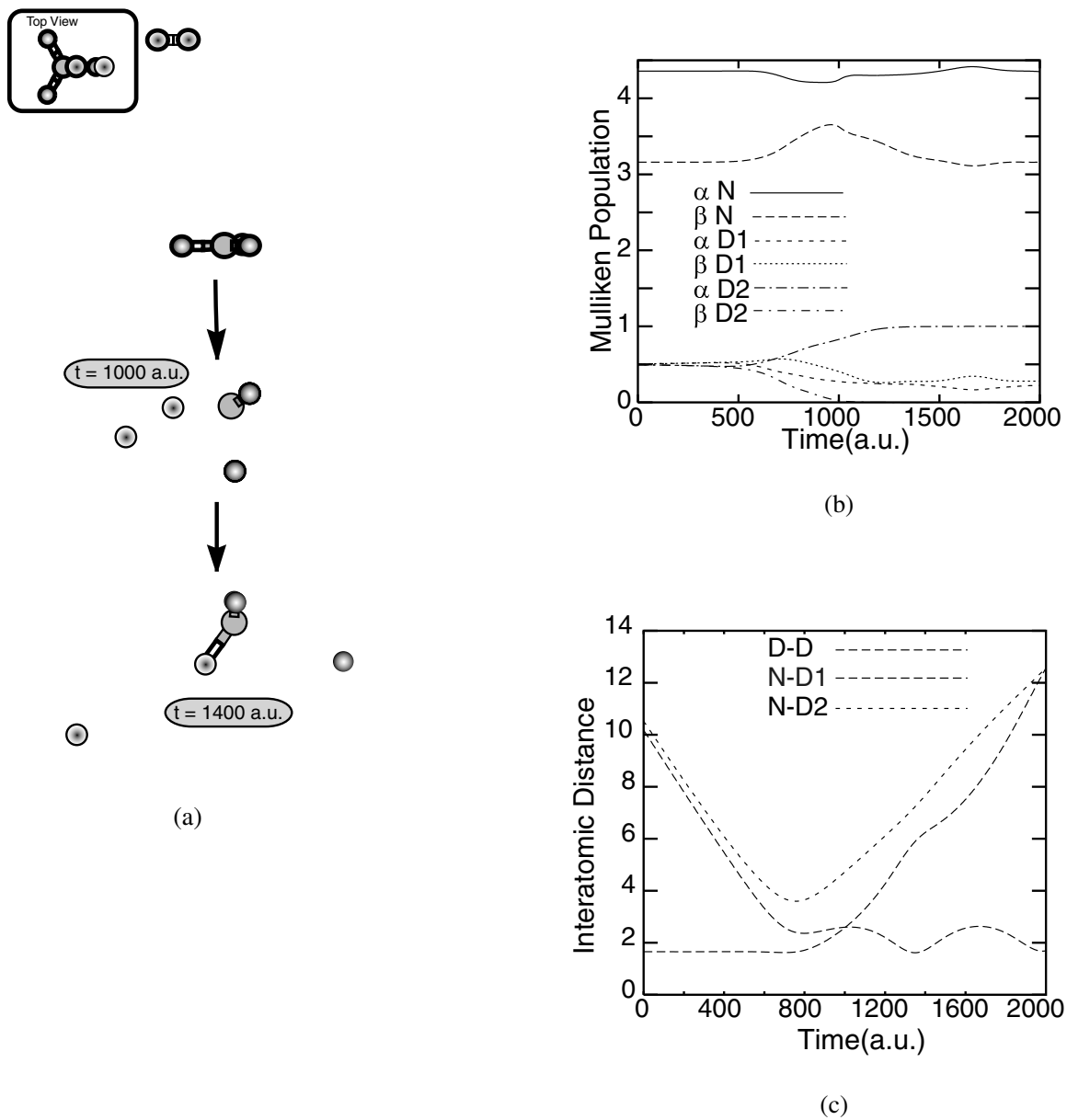


Figure 2.17: Typical END trajectory of $D_2 + NH_3^+$ with a D_2 initial eclipsed (3) orientation leading to direct exchange. Time-evolution of atomic charges and interatomic distances. The collision energy for the trajectory was 12 eV.

mechanism for all orientations. Figures 2.18 and 2.20 show that albeit having a broad angular distribution, all the flux is forward scattered for all orientations.

2.5 Discussion

Structures similar to **c** and **g** from Figure 2.3 occur on abstraction trajectories at 6 and 8 eV COM collision energy that have a rebound type mechanism. They are generated when starting with D_2 initially at orientation 1 (axial) as pictured in Figure 2.4 and form abstraction products with a large amount of internal excitation. Structure **i** from Figure 2.3 occurs in direct exchange trajectories at 8 and 12 and 16 eV of collision energy COM. Most of exchange trajectories have a billiard ball type mechanism, somewhat more constrained but similar to structure **i**, where the incoming D_2 molecule hits a H atom head on, followed by the breakage of the D_2 bond, the ejection of a H atom and capture of a D atom by the nitrogen. The configurations that contributes most to the abstraction cross section at all energies are modifications of structure **g** where the D_2 molecule is parallel or at a small angle to the original NH_3^+ plane. These configurations are generated by starting with D_2 orientation 3 (eclipsed) as pictured in Figure 2.4. On these configurations the external D atom escapes in the forward lab direction and the mechanism is analogous to the SSM. Although the mechanism is SSM alike, SSM usually over estimates the amount of internal excitation on the abstraction product molecule NH_3D^+ . We do not observe structure **e** in exchange trajectories as it's configuration implies a rebound type mechanism that probably would occur at lower collision energies and high internal excitation.

The temporal scale used to generate experimental results considered in this work are much larger then the reaction times and much larger then the simulation times considerer on the dynamics simulation. Time of flight in octopole guides for

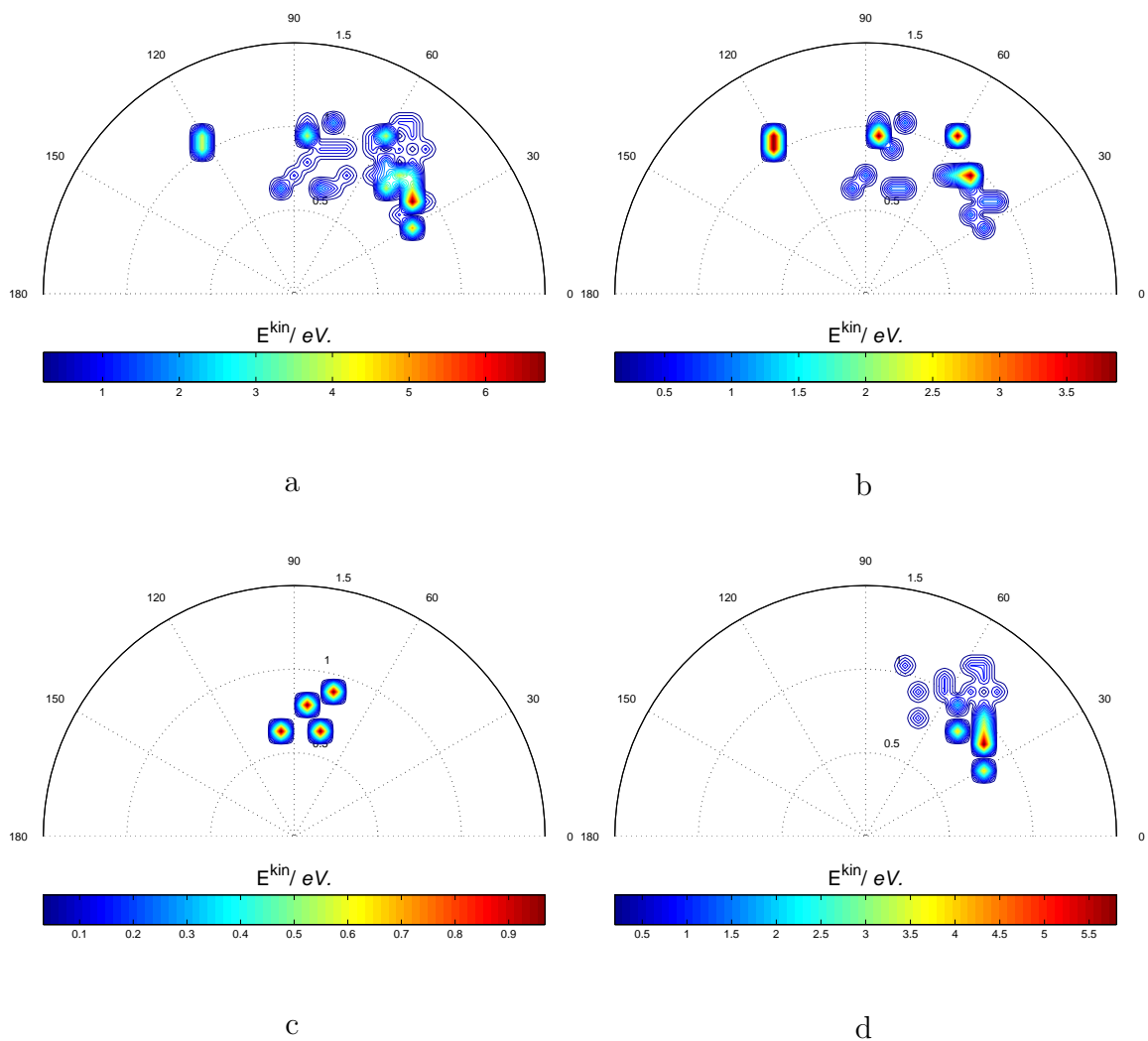


Figure 2.18: Flux velocity contour map for the abstraction product using a collision energy in the COM of 16 eV. We have clockwise: a) total flux; b) a partial of the grid with D_2 orientation label 1, c) same with orientation 2; d) same with orientation 3. The radial dimension is the final kinetic energy in the COM (eV) and colors label the histogram count.

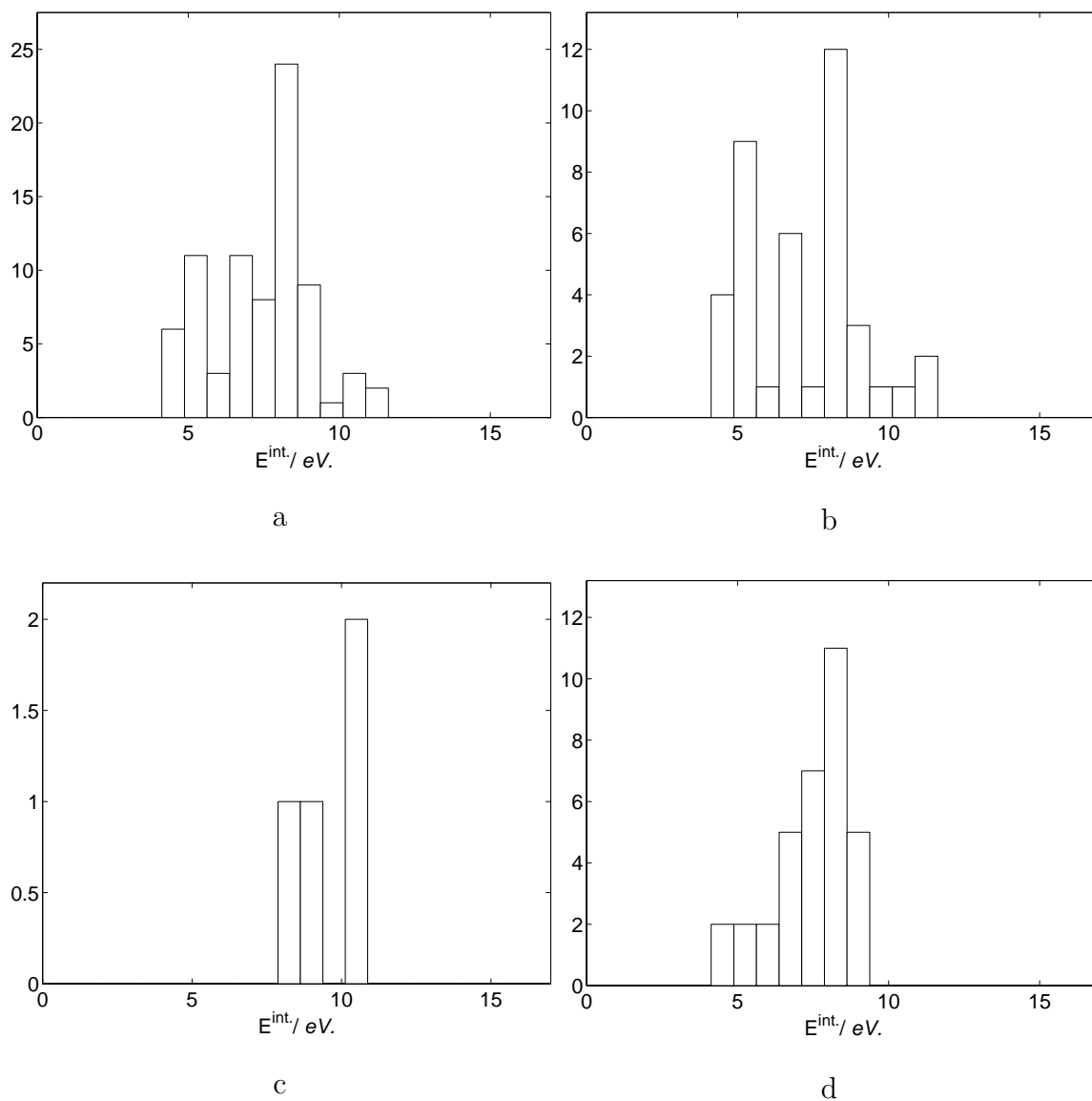


Figure 2.19: Histograms for internal energy transferred during the collision for the abstraction product using a collision energy in the COM of 16 eV. We have clockwise: a) total histogram; b) a partial of the grid with D_2 orientation label 1, c) same with orientation 2; d) same with orientation 3.

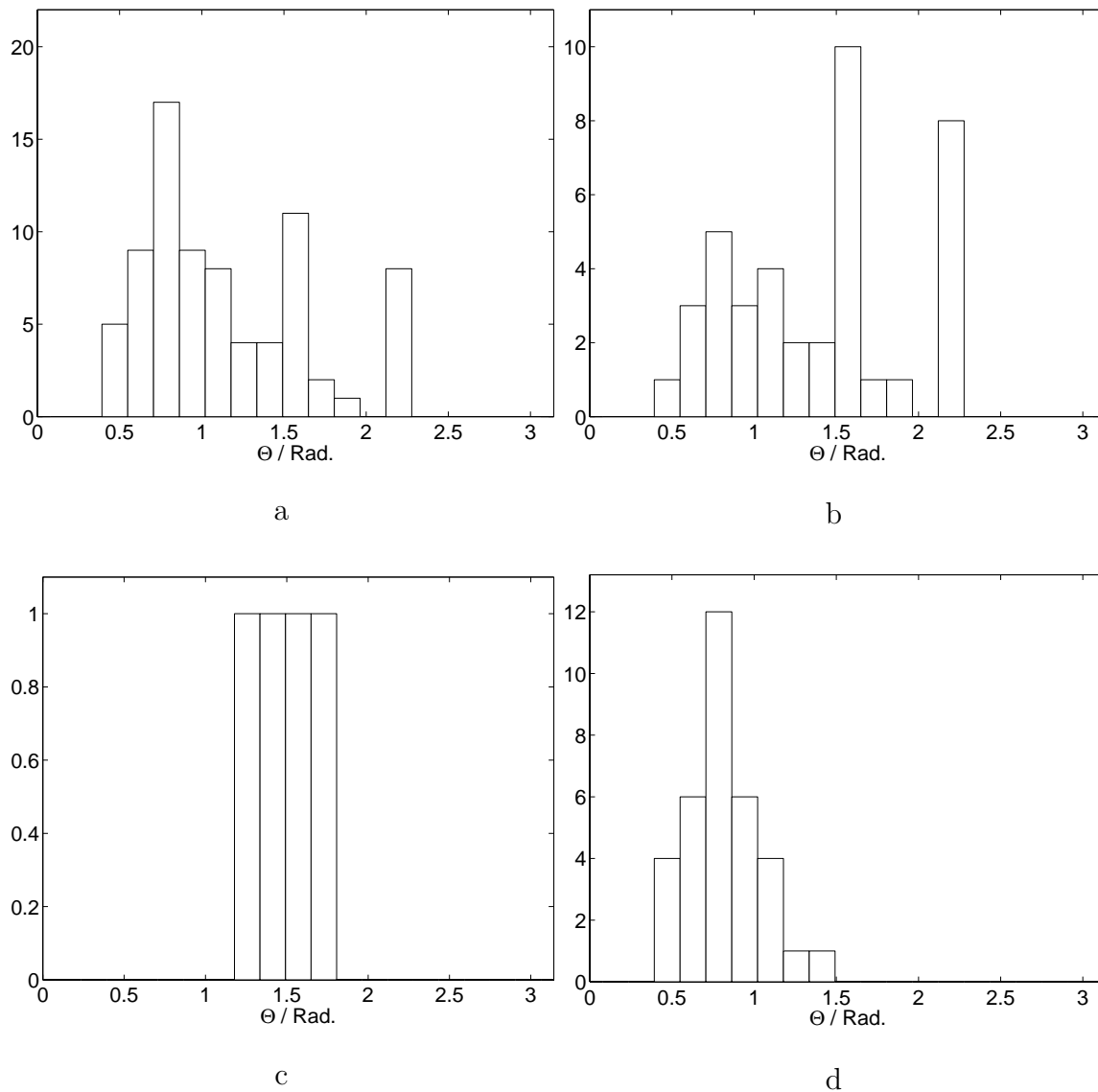


Figure 2.20: Angular distribution histograms for the abstraction product using a collision energy in the COM of gram 16 eV. We have clockwise: a) total histogram; b) a partial of the grid with D_2 orientation label 1, c) same with orientation 2; d) same with orientation 3.

the experiment considered here is around $50 \mu\text{s}$ from the reaction chamber to the detector while simulation times range from 80 to 200 fs. Owing to the formation of metastable abstraction products and the long time for product detection, the raw numbers for reaction cross sections computed from our simulations might not be the most accurate ones to compare with experimental results. A solution could be to just extend the simulation to longer times to estimate the fraction of metastable NH_3D^+ products that undergo reaction (V). Albeit a good idea, this would be an expensive computational procedure as we don't know for how long we would have to propagate the simulation to obtain a good estimate for the fraction of metastable products that dissociate into NH_2D^+ . Trial simulations on highly excited products reveal that 200 fs was not enough to reach a definitive conclusion.

In order to estimate the possible measured results from the END calculations we compute three different relative cross section estimates by assuming that 50%, 75%, or 100% of the metastable NH_3D^+ products actually dissociate by losing an H or a D atom with equal probability before reaching the detector.

The results of this exercise are shown in Table 2.8 for the assumption that 75% of the abstraction products actually dissociate. We also show in Figure 2.21 the experimental results [55] for collision energies between 6 and 10 eV compared with our estimates from the END simulations. The theoretical “error bars” represent the 50% and 100% breakups and the line is drawn for the 75% assumption. It is interesting to note that at the lower collision energies the experimental results are closer to the 50% dissociation rate, while they are closer to the 100% rate for the higher collision energies. Our estimate at 10 eV of collision energy are interpolated results, since no END calculation were run for that energy. The results shown in Table 2.8 have a remarkable agreement with experimental data from [55]. Values for relative cross section for the exchange and abstraction channels

as well as trends are reproduced. Not shown in Table 2.8 is the fact that, when corrected for dissociation, the abstraction cross section maxima for the energy interval considered occurs at 6 eV and not at 8 eV as shown in Table 2.4. This results agrees with experiments performed by Morrison et al. [54]. In order to compute the internal energy, we use the values for kinetic energy loss to internal excitation given in Figures 2.8, 2.11 and 2.14 and assume, as in the SSM, that all ΔH_{rxn} energy goes for internal excitation of NH_3D^+ . Using the dissociation threshold given in Table 2.3 the estimate for the reactive cross section considering dissociation are shown in Table 2.8.

Table 2.8: Total cross sections for abstraction and exchange considering dissociation of metastable NH_3D^+ products. Theoretical values at 10 eV are interpolated.

E_{COM}^{coll}/eV	σ_{exch}/a_0^2	$\sigma_{abst.}/a_0^2$	$\sigma_{exch}^{exp}/a_0^2$	$\sigma_{abst}^{exp}/a_0^2$
6	14	86	11	88
8	31	69	37	63
10	49	51	63	37
12	69	31	na	na
16	79	21	na	na

2.6 Conclusions

Minimal END theory with a single determinantal wavefunction for the electrons and classical nuclei is capable of capturing the essential chemistry of the reactions (I) through (III). Our results strongly suggest that the exchange product formation is mostly due to a two step process given by channel (III). Contributions of a direct process become appreciable at 10 and 12 eV of collision energy COM. By making the assumption of dissociation of a substantial fraction of the metastable abstraction products (NH_3D^+) the calculated relative cross sections agree well with the experimental results [55]. This assumption is supported by the behavior

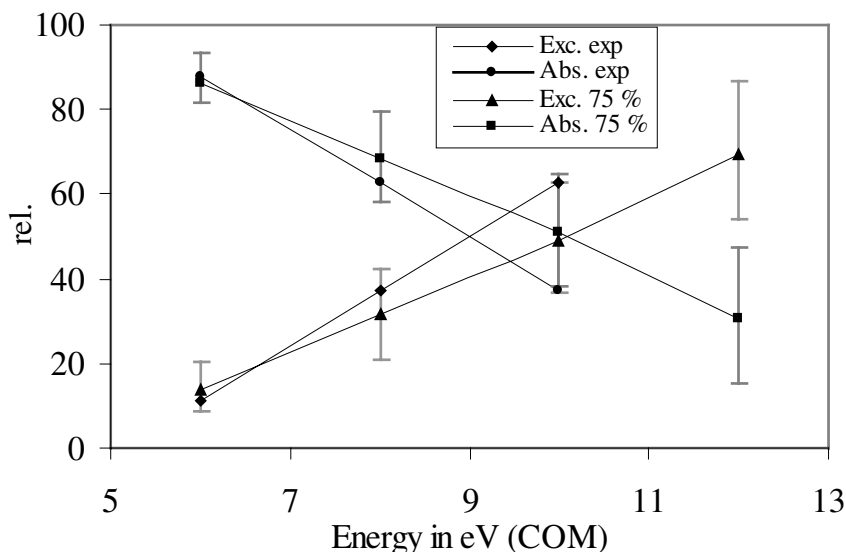


Figure 2.21: Experimental and theoretical relative cross sections. Theoretical values and error bars are obtained from dissociation probability estimates.

of sample trajectories and by the saturation of the abstraction channel seen at 16 eV of collision energy. Our predictions of the collision energy threshold for the exchange reaction being lower than 6 eV and the maximum of the adjusted abstraction cross section occurring at 6 eV for the corrected results also agrees with the measured results.

We believe that for the energies used in the present study the inclusion of all degrees of freedom is essential for the correct description of the chemical process. Fast internal energy redistribution occurring on nascent NH_3D^+ products can enhance the life span of metastable molecules by redistributing vibrational excitation among all modes. After the initial energy redistribution, dissociation can only happen in the relatively rare event of energy getting refocused in a particular stretch mode.

We conclude that for the energies considered the principal process for the abstraction product formation (NH_3D^+) does not proceed via a rebound mechanism. However, such a mechanism is very important for the exchange process at 6 and 8

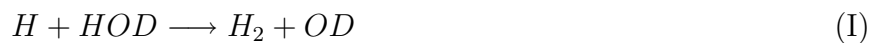
eV via the reaction (III). It is also clear that the SSM estimates for internal excitation are inadequate for this reaction since two very distinct mechanisms are in operation. Interestingly the predicted SSM value turns out to be a good estimate for the averaged internal excitation, but overestimates the calculated values for END trajectories that have a mechanism more akin to that of the SSM assumptions, for instance reactive trajectories starting from orientations 2 and 3 in Figure 2.4.

Although we did not explore the effects of internal excitation on the reactivity we find, due to the two step mechanism present with the formation of a long-lived intermediate, that the title reaction has very little mode specificity at a hyperthermal collision regime in agreement with experiment.

CHAPTER 3
H+HOD COLLISION AT 1.575 *EV*.

3.1 Introduction:

In work done by Bronikowski and coworkers [56, 57, 58] the cross section ratio (CS ratio), or branching ratio, for reactions (I) and (II) was measured for *HOD* prepared in its ground molecular state.



The experiment also measures the reaction where *HOD* was prepared with one quanta of vibrational excitation in the local *OD* and *OH* stretching modes. Experimental results show that enhancement due to the initial vibration was noticeable and that selective chemistry could be achieved for this 4 atom system. This was one of the first studies in which one could successfully control the selectivity of a reaction by exciting one of the reactants. The reaction of *H + HOD* was also experimentally studied by Sinha [59] and by Metz [60] where *HOD* was prepared initially in higher vibrational states.



The values measured by Bronikowski and coworkers indicated an enhancement greater than 20 for σ_{OD} and greater than 5 for σ_{OH} when comparing to the cross sections for *HOD* in its ground molecular state. The reaction enhancement is calculated as the ratio between the cross section for *OH* and *OD* formation starting with *HOD* in its ground state and the cross section starting with *HOD* in its

excited vibrational state. A branching ration of 1.38 ± 0.14 is associated with the ratio of the cross sections $\frac{\sigma_{OD}}{\sigma_{OH}}$ for HOD in its ground state shows that an isotopic effect exists even when no excitation is present in the nuclear motion. No absolute cross section was obtained in Bronikowski’s work. However, comparison with the work of Kessler and Kleinermanns [61], which measured the absolute cross section of the reaction (IV) at the same collision energy made possible the estimation of the total cross section. The estimates were obtained for reactions (I) – (II) by computing the ratio between the Laser induced Fluorescence (LIF) signal of the species with known total reactive cross section, σ_{OH} from reaction (IV), and the LIF signal of species with unknown total cross section.

Most, if not all, of the theoretical work done on this reaction use a common potential surface, sometimes with modifications, prepared by Elgersma and Schatz [62] over the *ab-initio* data points of Walch and Dunning [63] (the WDSE potential). There has been calculations using the quasiclassical trajectories method by Schatz and coworkers [62, 64], full quantum (with and without constrained nuclear degrees of freedom) by Zhang and Light [65] and by Wang and Bowman [66]. The and close-coupling equations for the nuclear motion were solved by Clary [67]. The reader may at this point ask what is different between the prior approaches and ours. First, our method does not use a precalculated potential energy surface. This has the advantage that one does not need to know the whole potential surface in advance. Second, we allow for excited electronic states to participate in the dynamics. Although the first excited potential surface of HOD is far apart in energy from the ground state one. This energy splitting is not known for all possible geometries of the collision complex $H + HOD$. Also, our experience have shown that one can perceive small cumulative effects on the differential cross section [68] due to the influence of excited states on the dynamics. It is still uncertain if those

effects are important for the calculation of the total cross section of the considered reaction. It is nevertheless clear that if the dynamics stay close to the ground state potential the surface then minimal END is not of the same quality as dynamics on a surface obtained from high quality *ab-initio* methods.

We also find it valuable to verify if conclusions reached in previous work would hold for our study considering that we have a different description of the collision process with the END theory. We realize that our description of the electronic degrees of freedom is approximate, but the surface used in most calculations, the WDSE surface, is also inexact. For example, for a collision on the WDSE surface only one of the bonds is allowed to break due to the asymmetric nature of the potential w.r.t. the activation barrier for abstraction. While experimental results indicate that the nonreactive bond acts as a spectator bond during the reaction and theoretical results do agree with that observation, the difference in activation barrier between the two bonds must not be crucial for the simulations. As we have a symmetric potential, there is no need to introduce *ad-oc* constraints. The reactive bond is whatever one the dynamics chooses.

Some experimental considerations need also be kept in mind when comparing the experimental results with results from theoretical calculations. In order to compute the products absolute concentration the experiment assumes that the LIF signal used to detect the products is near its saturation limit of 50 %. This means that the published enhancements are in fact a lower bound to the true enhancement. On the other hand the source of hydrogens for the experiment produces two atoms, one with 1.575 eV and another one with 0.6 eV of translational energy. The last one does not have enough energy to react with unexcited *HOD* but does have enough energy to react with the excited *HOD* molecule even in its lowest vibrational states. As the hydrogens are produced from the photolysis

at a ratio of 1:1.8, the one with 1.575 eV being the most common, the effect on the enhancement calculation might be non-negligible and the enhancement due to vibrational excitation can from that point of view be overestimated. Those considerations reveal the difficult nature of the experimental study undertaken by Bronikowski and coworkers.

3.2 Computational Details

The basis function used throughout the calculation was a STO-3G (1s2s2p) for the Oxygen and 4-31G (1s2s) for the hydrogens and deuterium. Although small, this basis produces the correct behavior necessary for the description of the reaction, i.e., the barrier for the $H + HOD$ reaction is for some known reactive orientations close to the published value of 0.9 eV, i.e., smaller than the hydrogen translational energy of 1.575 eV. In an exploratory study we consider the initial orientation of the H momentum vector to lie along the OD bond axis and with the HOD molecule in the plane that contains the OH bond and the projectile momentum vector. we refer, from now on, to this as the original collision plane. Calculations showed that using this orientation and the O:STO-3G H:4-31G basis the system undergoes a hydrogen abstraction reaction. This result is in agreement with others that point to this particular orientation as important in explaining the overall reactivity of the $H + HOD$ reaction. An attempt to improve the basis used in the first part of this work is developed in Section 3.4.

The calculation of the reaction cross section for the vibrationally excited HOD requires new considerations not present in the calculation of the ground state cross section. Due to the importance of the timing between the bond vibration and the impact time, we need to introduce another average distinct from the ones considered before. Specifically, we need to average over all possible conditions

generated when different initial phases are considered for the vibrational motion. The integration of the phase angle is equivalent to integrating over different initial internuclear separations [69, 70] with the limits of the integral given by the period of vibration. In practice this is done by considering different impact distances in a range given by the travelled distance of the projectile during a vibrational period, i.e., we calculate the cross section as defined above considering different initial impact distances and the same vibrational phase and average the result to produce the final cross section. In our calculations we consider four distinct initial distances for each cross section calculation of a vibrationally excited reactant. The integral for the total cross section presented in chapter 1 becomes

$$\sigma_k(E_{Lab}) = 2\pi \int_0^\infty b P_k(b; E_{Lab}) db \quad (3.1)$$

with an opacity function $P_k(b, E_{Lab})$ given by:

$$P_k(b, E_{Lab}) = \frac{1}{8\tau\pi^2} \int_0^{2\pi} \int_0^{2\pi} \int_0^\pi \int_0^\tau p_k(\alpha, \beta, \gamma, R_{AB}, b) \sin \beta d\alpha d\beta d\gamma dt, \quad (3.2)$$

where we have chosen to represent the phase integral over a vibrational period τ .

A visual representation of the mentioned procedure is shown in Figure 3.1

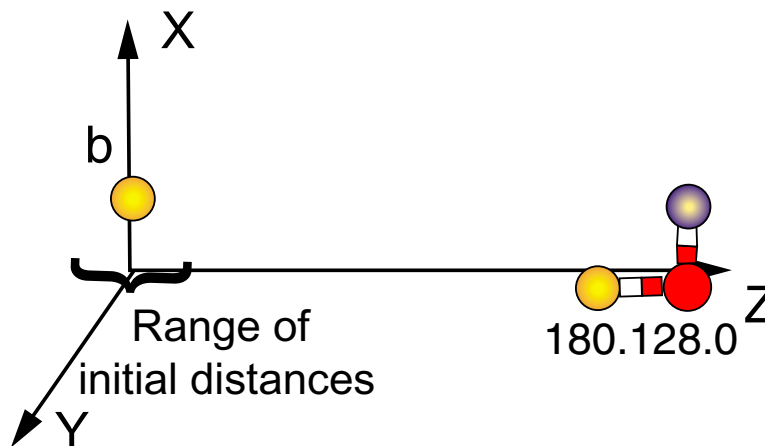


Figure 3.1: Pictorial representation of the phase average procedure used to calculate cross sections for initially excited *HOD* reactant.

A consideration absent in the majority of the work done concerning this reaction is the study of the role of excited states on the dynamics of the hydrogen abstraction. It has been shown that the first dissociative state of H_2O ($\tilde{A}^2 \ ^1B_1$) can be accessed with 266nm (4.66 eV) lasers and even 288nm (4.30 eV) lasers provided the system is far enough from equilibrium (see Vander [71] and also Plusquellic [72] and references therein). For the ground vibrational state of H_2O the absorption band starts around 180nm (6.88 eV). Approximate calculations using CIS and our small basis placed the first excitation energy at 7.79 eV. However, the quantity of interest here, at least for interpretation purposes, is really the lowest excitation energy for the collision complex. Spectroscopic results for collision complexes are hard to find and the present system is no exception. We estimated the first excitation energy, using CIS (configuration interaction with single excitations [73]), for the collision complex formed during the reaction starting with the initial orientation labeled by Euler angles 0.128.0 and impact parameter 0.2 to be only 1.17 eV. For the mentioned CIS calculations we used the same basis function used throughout this work. Calculation using a larger basis for all atoms, namely PVDZ, produced a first excitation energy of 2.61 eV for the same geometry of the collision complex. In a less dramatic example, the collision complex formed during the reaction that started with the initial orientation labeled by the Euler angles by 0.90.0 and impact parameter 1.0 had the first excitation energy at 2.62 eV for CIS and our small basis and 4.50 eV when using CIS and a PVDZ basis. The study of the nature of the excitation also revealed that there is only one configuration that has major importance for the description of that particular excited state. This is important, as it makes our method quite appropriate for describing the dynamics that involves the ground and this particular first excited state.

3.3 Results

We are using throughout this work the notation $[\alpha, \beta, \gamma]$, where α, β, γ are Euler angles, to label the different initial target orientations of the collision. In this notation $[0, 0, 0]$ is the original orientation pictured in Figure 3.2. Vibrational excitations of the *HOD* molecule are identified by tree numbers, the first one refers to the excitation of the mode with character of *OD* stretching, the second one refers to excitations of the bending mode, and the third one refers to excitation with the character of the *OH* stretching mode.

The O:STO-3G H:4-31G basis has a total of 22 functions and corresponds to 60 electronic parameters in the Thouless determinant. The grid used in the cross section calculations consists of 120 different orientations generated by Euler angle rotations. We used the y-counter-clockwise convention with the z axis lying between the H and D atoms in the molecule plane and the y axis perpendicular to z and to the *HOD* plane. For impact parameters we used an interval of 0.2 a.u. ranging from 0.0 to 4.0 a.u. along the x axis. The impact parameter was measured with respect to the center of mass of the target.

As mentioned earlier our method does not use potential energy surfaces. Although we consider this an advantage of the method there is no simple picture that can be extracted from our mathematical description of the dynamical state. To help to visualize the results obtained for the cross section we focus on key orientations leading to reactive trajectories and contribute substantially to the total cross section calculation. We believe that the direct interpretation of the results produced by the dynamics, bypassing the step of interpreting potential energy surface features, may be more meaningful especially when excited states participate in the dynamics.

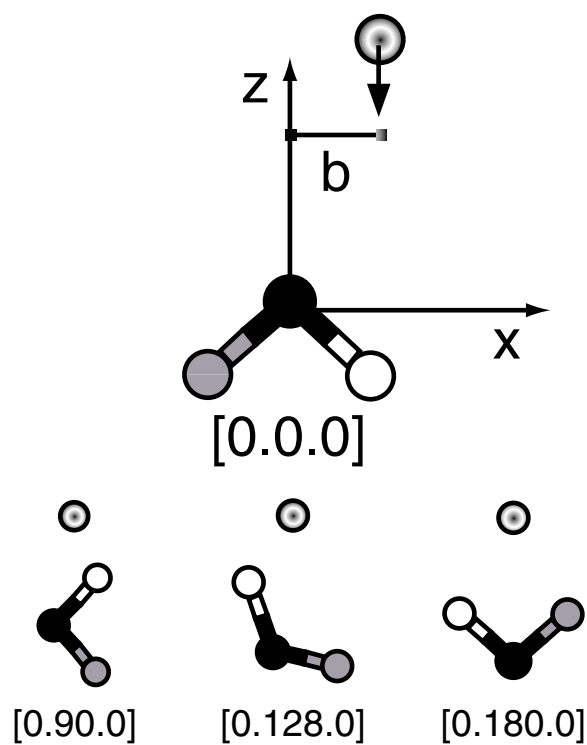


Fig 2

Figure 3.2: Placement of HOD molecule for the $[0,0,0]$ orientation in the xyz plane with the H atom as the open circle with a positive x coordinate. The projectile H atom has an initial momentum in the negative z direction and an impact parameter b in the x direction. Also, three typical reactive target orientations are shown.

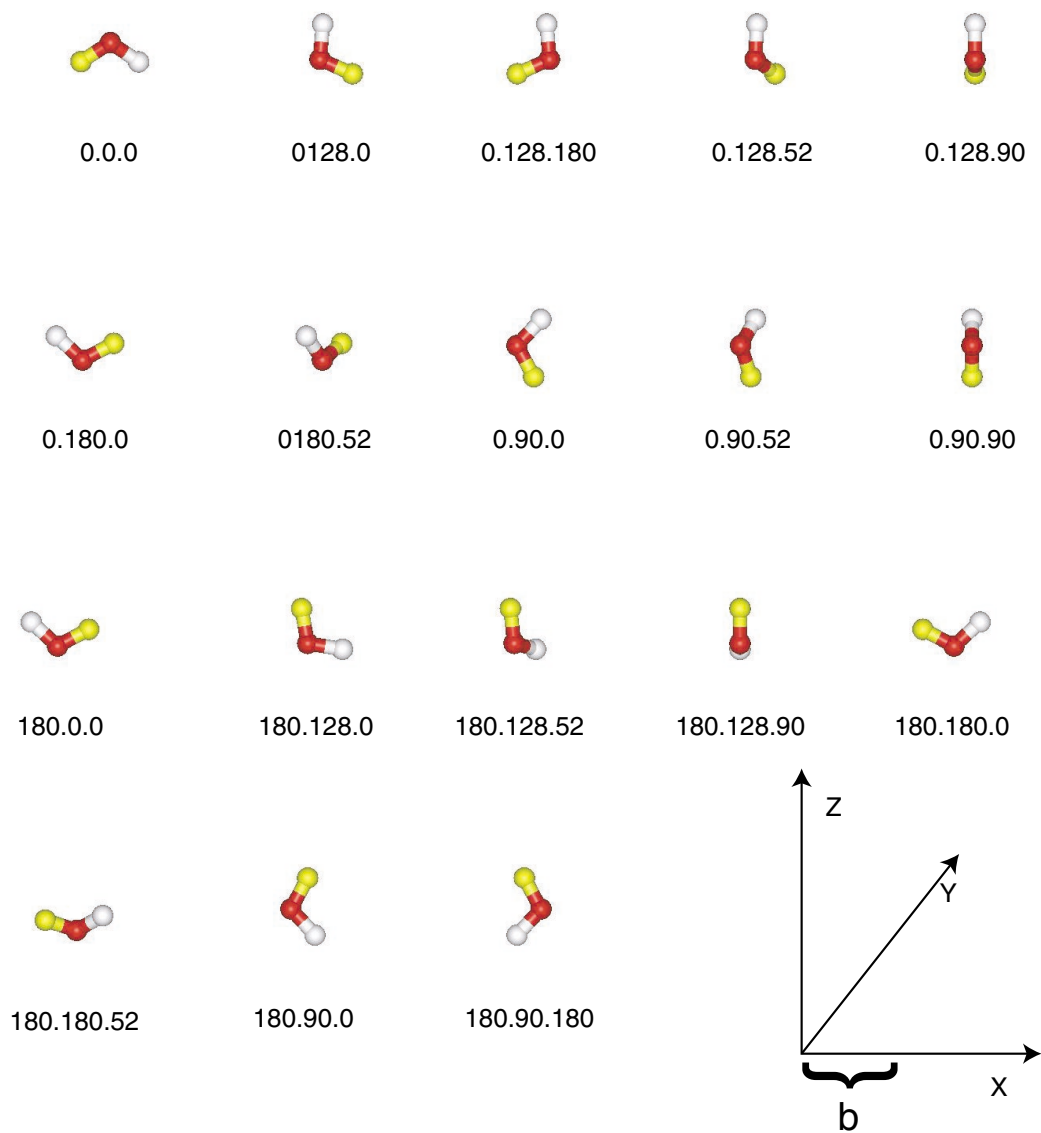


Figure 3.3: Orientations (36 unique) used in the integration grid for the $H + HOD$ reaction. The configuration labels refer to the Euler angles in the body fixed 'y' convention.

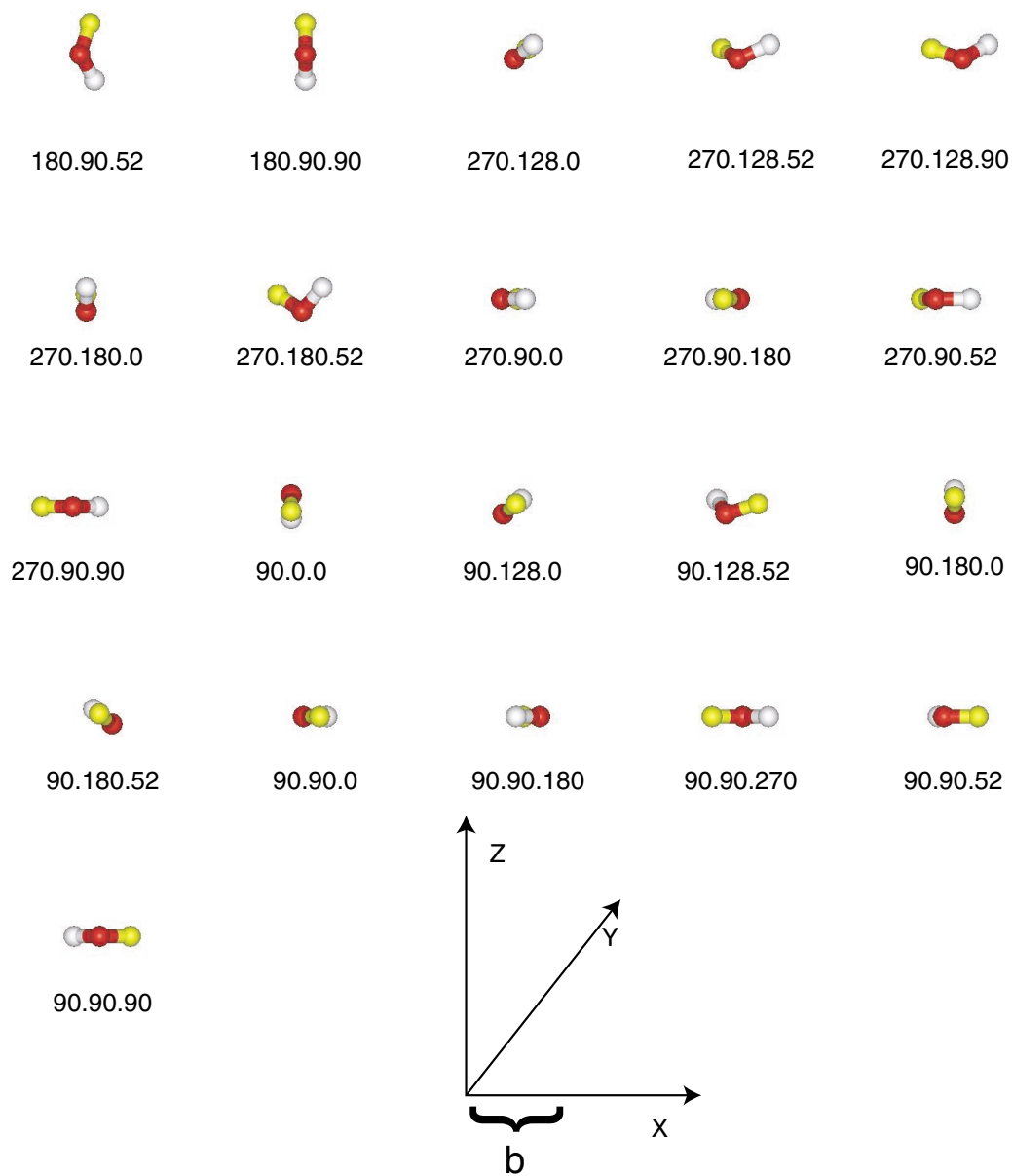


Figure 3.4: Continuation for orientations used in the integration grid for the $H + HOD$ reaction. The configuration labels refer to the Euler angles in the body fixed 'y' convention.

3.3.1 Results for *HOD* — Vibrational Ground State

The group of reactive orientations for the abstraction process were the ones with $[0, 128, X]$ ($X= 0, 52, 90, 180, 270, 360$), $[180, 180, 0]$ and $[0, 90, 0]$ for H abstraction (HA), and $[180, 128, X]$, $[0, 180, 0]$ and $[180, 90, 0]$ for D abstraction (DA). These orientations are similar to the cone of trajectories described elsewhere [56, 57, 58] and are also pictured in Figures 3.2, 3.3 and 3.4. However, a cone picture as the reactive part of the grid is not 100 % accurate as the trajectories do show sensitivity to the angle of attack to the OH/OD bond. More specifically the range of reactive impact parameters for the HA type reactions is about the same for the $[0, 128, X]$ set of orientations where the projectile initial momentum is parallel to the OH bond, but only $[180, 180, 0]$, and $[0, 90, 0]$ undergoes HA on the $[0, 180, X]$ and $[0, 90, X]$ set of orientations, i.e., only in the plane ($\gamma = 0$) trajectories are reactive for this set of orientations. Collisions perpendicular to the *HOD* molecule plane, e.g. $[90, 90, X]$ and $[270, 90, X]$ lead to exchange reactions, named here EH for exchange with H and ED for exchange with D. These resemble billiard ball type collisions where the displacement is induced by a direct hit of the incoming on the outgoing atom. Some in the plane trajectories also lead to exchange reactions and in the case of the ED reaction these are very important for the cross section of that particular channel.

Table 3.1 shows the results for the cross section we calculated for reactions (I)-(III) with *HOD*(0, 0, 0). Table 3.2 presents our results compared to various other theoretical treatments published on the literature. The theoretical treatments are full dimensionality quantum approach (FDQ) [65], reduced dimensionality adiabatic-bend approach (RD-AB) [66], and quasiclassical trajectories (QCT) [74].

Table 3.1: Exchange and abstraction reaction cross sections for $H + HOD(0, 0, 0)$ in \AA^2 .

$\sigma_{OD}/\text{\AA}^2$	$\sigma_{OH}/\text{\AA}^2$	$\sigma_{HOH_E}/\text{\AA}^2$	$\sigma_{HOD_E}/\text{\AA}^2$
0.337	0.277	0.020	0.162

Table 3.2: Absolute cross section and cross section ratios for the reaction $H + HOD(0, 0, 0)$.

Method	OD:OH	$\sigma_{OD}/\text{\AA}^2$	$\sigma_{OH}/\text{\AA}^2$
END	1.22:1	0.337	0.277
FDQ	1.37:1	0.028	0.020
RD-AB	1.38:1	0.031	0.025
QCT	2.5:1	0.076	0.014
Exp	1.38 ± 0.14	0.085 ± 0.035	0.062

After calculating trajectories over all possible collision conditions we have the necessary data to compute the exchange cross section for the H and D exchange with H projectile. From the results in Table 3.1 one can see that our method predicts a strong isotope effect also on the exchange cross section. We could not find experimental results for the exchange cross sections. This came as no surprise since those cross sections should be very hard, if not impossible, to measure due to the fact that they produce species in the reactant mixture usually considered of HOD studies, i.e. H_2O and HOD . Results for the cross section for the $H + D_2O(0, 0, 0) \rightarrow D + HOD$ reaction available in the literature ($0.36 \pm 0.15 \text{\AA}^2$, or 0.18 ± 0.075 per bond) may indicate that our value for σ_{HOH_E} is too low [75].

3.3.2 Results for $HOD(0, 0, 1)$ — OH Local Mode Excited

Due to the large computational requirements to run a complete grid of orientations and impact parameters, as defined for the calculation of the cross section of the ground state reaction, we decided to reduce the size of the grid for the cross section calculation with the reactant in a vibrational excited state. We assumed that no new orientation would be reactive, i.e., only the orientations that were

reactive for the ground state reaction were considered in the calculation of the cross section with vibrationally excited HOD . This is the same as to say that the only changes in total cross section were due to changes in the impact parameter range that produced reactive trajectories. Within that approximation 12 unique orientations were considered for the cross section calculation. Using symmetry considerations those 12 unique orientations correspond to 40 orientations of our original grid of 120 orientations for the cross section calculation with HOD in its ground state. As mentioned before, to get a total cross section for $HOD(0, 0, 1)$ we need to perform an average over one vibrational period of the local mode vibration. We performed this average by running trajectories at different initial impact distances for the incoming hydrogen, namely 9.28 a.u., 10.0 a.u., 10.71 a.u., 11.42 a.u. and 12.13 (identical to 9.28 a.u. due to the periodic nature of the vibration). By following this procedure the collision for each different initial impact distance will occur during different phases of the vibration, averaging out any specific effect of the timing between the vibration and the collision. Although those considerations may not seem *a priori* of much relevance, we have observed an extreme sensitivity of the total cross section with the timing of the collision. Variations of as much as 60% in the cross sections were found when only the initial impact distance was changed.

A general trend was that softer collisions (softer being the trajectories that collide in phase with the vibration) produced reactive trajectories over a wider impact parameter range therefore increasing the cross section. This can be understood using a simple model for the reaction and energy conservation arguments. In one limiting case the collision happens when the excited bond H or D atom has momentum opposite to the velocity of the incoming H . A large amount of energy goes into the vibration of the formed H_2 or HD molecule making the system hit

the H_2/HD repulsive wall. What follows next is that the abstracted atom returns to the HOD molecule and no net reaction takes place. In a second limiting case the collision happens when the incoming H and vibrating H or D have momentum pointing in the same direction. Under those conditions most of the energy is released as kinetic energy of the newly formed H_2/HD (if this is true, the calculations with the OD bond excited should show a smaller dependence on the timing of the collision due to the smaller vibrational frequency of the OD bond). Another trend we have observed is that changes in the impact parameter range, that was reactive in the ground state reaction, happen in the direction of larger impact parameters, sometimes at the expense of smaller impact parameters becoming nonreactive.

Table 3.3 presents our results compared to various other theoretical treatments published in the literature for $H+HOD(0,0,1)$ reaction. The nomenclature follows form Table 3.2.

Table 3.3: Absolute cross section and cross section ratios for $H + HOD(0,0,1)$ reaction.

Method	OD:OH	ENH	$\sigma_{OD}/\text{\AA}^2$	$\sigma_{OD}/\text{\AA}^2$
END	2.50:1	1.78	0.60	0.24
FD	13.5:1	16.5	0.276	0.024
RD-AB	14:1	19	0.312	0.023
QCT	8.5:1	7.1	0.403	0.047
EXP	> 25:1	> 20	> 1.54	0.062

3.4 Improving the Basis Description

A consistent END result for reactions (I) and (II) from ground and excited HOD molecules is that the calculated total cross section is larger then that obtained with other theoretical methods. When compared to experimental results,

the END results fail to show the large enhancement observed experimentally and by some other theoretical methods.

In order to seek to understand our results a basis set study was performed for the $H + HOD$ reaction. Properties considered to judge basis set quality were based on properties of the Hartree Fock (HF) SCF solution for the system. Barrier heights as well as ground and transition state geometries and frequencies were considered. Our results for energies, geometries and frequencies for an optimized basis is shown on Table 3.4 along with results for other potentials used to describe the $H + HOD$ reaction. The potentials considered for comparison were IS5 from Isaacson [76], OC from Ochoa, Aspuru and Clary [77] and WDSE from Schatz and Elgersma.

In order to optimize the basis functions we started with the following basis for the HOD molecule: O:4-31G (8s4p:3s:2p) and H:6-31G** (4s1p:3s1p). The basis were fully uncontracted and the exponents were optimized using the GAMESS [78] program for ground and transition state geometries. The contraction scheme was kept the same as in the original basis for the core (1s orbital on the oxygen) but changed for the valence. We contracted the basis using SCF orbital coefficients from an atomic calculation using the scheme O 8s4p:3s2p and H 5s1p:2s1p with (independent s and p exponents). The valence contraction was done using an average between optimum values for exponents and coefficients at the ground state and transition state structures.

The optimized basis manages to reproduce at the HF level several of the important features present in higher level potentials. The most obvious difference between the HF results and the other potentials is on the location of the transition state. At the HF level it occurs too early in the configuration space, resulting in a potential that is too steep along the reaction coordinate when compared to the

other potentials. The transition state frequency as well as the newly formed bond frequency at the transition state configuration reflect this fact. As a result the potential exhibits an inaccessible transition state for trajectories that deviate slightly from the steepest descent reaction path. In other words the potential constructed from the optimized basis functions is unreactive for trajectories at the energy of 1.575 eV. Electronic correlation effects might be the source of such discrepancy as the IS5 and OC potentials are calculated using multi reference methods.

Table 3.4: Energy differences (ts=transition state, rxn=reaction), transition state frequency (imaginary) and frequency for the newly formed bond. (a) Frequencies in brackets corresponds to calculations at the IS5 transition state geometry. The energy difference for the true END TS is -0.09 eV. Results are in eV for energy and cm^{-1} for frequency.

Method	ΔE_{ts}	ΔE_{rxn}	FRQ_{ts}	$FRQ_{(H_p-(H/D))}$
END	1.14	0.12	2878 (1410 ^a)	1767 (2356 ^a)
IS5	0.93	0.67	1476	2205
OC	0.89	0.64	1102	2505
WDSE	0.94	0.69	1191	2576

3.5 Conclusions

The preliminary study of the reaction using a small basis showed that the END theory managed to reproduce the ground state reaction of $H + HOD(0, 0, 0)$ with a certain degree of success. The anisotropy in the reactivity between the OD and OH bonds was correctly described by the END method even when using a minimal basis set for the dynamical study. An attempt to describe an enhancement with initial reactant excitation proved unsuccessful and did not reproduce the experimental results. It is important to note that other theories that also rely on classical nuclei (QCT) reported results obtained by neglecting trajectories with products having energy less than the zero point vibrational energy. The interesting shape

of the ground state potential along with the inability of methods that use classical nuclei to obtain favorable results for the enhancement indicate that quantum effects might play an important role for this reaction. We did not observe effects related to electronic excitation that might imply a non-adiabatic mechanism for the title reaction.

CHAPTER 4
LIH AND *HF* DYNAMICS UNDER INTENSE FIELDS

4.1 Introduction

The classical and quantum dynamics of simple systems, in particular diatomics, under the influence of a strong electromagnetic field has received much attention over the past years [79, 80, 81, 82]. Photodissociation rates and nonlinear effects in the absorption spectra are some of the properties that can be directly studied using methods that describe the dynamics of the system. The electron nuclear dynamics (END) theory used is formally capable of describing both dissociation and the interaction of the system with a strong electromagnetic field in an *ab-initio* manner. No predetermined potential is used and all the couplings between electronic and nuclear modes are present in the dynamical equations. Neither is any perturbative expansion used to calculate the interaction of the system with the radiation.

In the present study we look at vibrational excitation through the interaction with intense infrared laser fields of two simple diatomic molecules, namely *LiH* and *HF*. The (small) size and the availability of good potential surfaces, useful for comparison purposes, were some of the important factors to be considered when choosing the system. Approximations appropriate to intense lasers are introduced, namely, treating the field classically, and employing the dipole approximation. Thus the molecule interaction with laser light can be formulated in terms of a time-dependent external field. This formulation is not restricted to harmonic time dependence, but is general. Excitation induced through intense infrared lasers in the HF molecule has been studied extensively. Both nonrotating [79] and rotating

HF [80, 83], in a monochromatic field have been considered and the quantum and classical approaches compared and found to lead to similar conclusions. Classical mechanics predicts time averaged quantities of the correct order of magnitude and also correctly predicts increased, although underestimated, excitation for laser frequencies to the red of the fundamental one-photon resonance. It does not produce peaks at the multiphoton frequencies. This can be understood since the multiphoton resonances are essentially quantal phenomena. The anharmonicity of molecular vibrations impedes the efficiency of the excitation process because the field becomes more off resonant up the ladder of excited states and the dipole transition matrix elements diminish progressively. Efforts have been made to tailor the laser field such that excitation or dissociation probabilities are optimal. Investigations have been done with two-mode lasers [84, 85, 86], with chirped ultrashort pulses [87], with trains of pulses [88], and also with the use of control theory to optimize the features of the pulse trains [89]. In view of this previous work, little needs to be added concerning the interrelation of classical and quantum description of the laser or the effect of the laser properties on the nuclear vibrational excitation.

Our study focuses on the impact of the coupling to the electrons, either directly through the nonadiabatic electron-nuclear terms or indirectly through the effect of the electron-field interaction on the electronic structure. In all of the above mentioned investigations it is assumed that the electronic structure is not perturbed by the electron-field coupling even though extremely high (10^{12} - 10^{14} W/cm²) power densities are used. Our method allows us to take a critical look at this assumption. We show that, in the cases studied, the nonadiabatic terms have negligible effect, while the modification of the electronic structure engendered by the interaction with the field has considerable effect on the vibrational dynamics. Other dynamics studies have been made with external fields and approximate (diatomics

in molecules, DIM) surfaces (see, e.g., Bastida and Gad ea [90]) taking into account nonadiabatic effects.

We consider the simple diatomic molecules HF and LiH and initial conditions that do not induce rotation as a first effort, for computational simplicity and because diatoms allow for a stringent comparison of the END approach with quantum wave-packet calculations. Particularly the HF system has been used extensively in various studies. These two diatomics are quite different. LiH has a bigger dipole, is a strongly ionic molecule even for large nuclear displacements, and has a rather anharmonic potential, while HF is more harmonic and has a nonlinear dipole as a function of internuclear distance indicating a more covalent bonding character.

For the sake of comparison other methods of calculating the interaction of molecular systems with strong fields were also used. We perform wavepacket propagation on pre-constructed ground state electronic potential surface of LiH using initial conditions identical to the ones used in the END calculations. Two types of molecular dynamics with a modified electronic Hamiltonian that includes the center momenta and the dipole interaction term were also calculated.

4.2 Theory

4.2.1 END with External Fields

The complete END equations traditionally include all the coupling between the electrons and nuclei. These couplings have the general form that depends on the parametrization of the wavefunction. The addition of the field to such a formalism is straightforward if we consider the field semiclassical limit, which is valid for the chosen range of laser intensities.

The Hamiltonian of the system in the presence of a field under the long wavelength approximation is given by

$$H = \sum_A \frac{P_A^2}{2M_A} + \sum_{A,B} \frac{Z_A Z_B}{r_{A,B}} + \sum_{A,i} \frac{Z_A}{r_{A,i}} + \sum_i \frac{P_i^2}{2m_e} + \sum_{i,j} \frac{1}{r_{i,j}} + \vec{\mu} \cdot \vec{\varepsilon} \quad (4.1)$$

where the sums run over the nuclei (A, B) and electrons (i, j). The dipole $\vec{\mu}$ is the sum of the electronic and nuclear dipoles.

The difference between the dynamical equations used in the present simulations and the standard END equations as described in section 1.3 in chapter 1 is the addition of a field dependence on the energy due to the extra term in the Hamiltonian. Note that the dipole moment depends on the parameters of the wavefunction, so additional terms appear in energy derivatives.

$$\frac{\partial E}{\partial R} = \frac{\partial E_0}{\partial R} + \frac{\partial \mu(R, z)}{\partial R} \cdot \vec{\varepsilon} \quad (4.2)$$

$$\frac{\partial E}{\partial z} = \frac{\partial E_0}{\partial z} + \frac{\partial \mu(R, z)}{\partial z} \cdot \vec{\varepsilon} \quad (4.3)$$

and an equivalent equation for z^* . E_0 is the unperturbed energy

$$E_0 = \sum_A \frac{P_A^2}{2M_A} + \langle z | H_{el} | z \rangle / \langle z | z \rangle. \quad (4.4)$$

where

$$H_{el} = \sum_{A,B} \frac{Z_A Z_B}{r_{A,B}} + \sum_i \frac{\nabla_i^2}{2m_e} + \sum_{i,j} \frac{1}{r_{i,j}} \quad (4.5)$$

The coupling with the field therefore introduces direct changes only on the r.h.s of the equation of motion (EOM) (equation 1.57 in chapter 1).

In this chapter we make use of the molecular dynamics (MD) and non polarized molecular dynamics (NPMD) that differ in the way they treat electronic polarization. The MD method allows for electronic polarization with the action

of an external field (but not electronic excitation) while the NPMD method does not. More details about the MD method and NPMD were presented on chapter 1 in section 1.3.2.

The END, MD, and NPMD methods are used in this chapter because they introduce a hierarchy of methods classified with respect to the behavior of the electrons under the action of a field on the dynamics. According to their dynamical behavior we have full dynamical electrons (END), polarizable electrons (MD) and static electrons (NPMD).

4.2.2 Initial Conditions

The harmonic coherent state for the nuclei $|z\rangle$ can be expressed as (z is a complex parameter, n is a positive integer)

$$|z\rangle = e^{-\frac{1}{2}|z|^2} \sum_{n=0}^{\infty} (n!)^{-1/2} z^n |n\rangle, \quad (4.6)$$

where $|n\rangle$ represents the harmonic oscillator stationary states. The occupation probabilities for a state n is given by

$$P(n) = \exp\left(\frac{E_\nu}{\hbar\omega}\right) \frac{E_\nu}{\hbar\omega} \frac{1}{n!}, \quad (4.7)$$

where E_ν is the energy going into the vibrational mode. The coherent state mapping is not only important in order to perform vibrational analysis for the trajectories, it also brings a theoretical framework for the choice of the initial conditions used in the calculations.

What is even more important is the fact that the mapping above is valid for the case where there is a field acting on a harmonic oscillator through a linear dipole function. This means that a quantum harmonic oscillator with a width equivalent to the ground state characteristic width will follow a classical trajectory when the field is turned on [91] for any initial phase of the field.

The mapping between the energy in a coherent state and the energy in a quantum state is $\hbar\omega |z|^2 \rightarrow \hbar\omega(|z|^2 + \frac{1}{2})$. This means that an initial condition in the classical harmonic system that maps onto the $\nu=0$ quantum state has the system at rest at the equilibrium position.

Grounded on the facts described above we used only one initial condition for all our simulations, the one with the oscillator at rest in the ground state, when performing both classical and quantum calculations. Anharmonicities and polarization effects break this elegant simplification and it is one of the purposes of this work to find out when this happens. The laser field is written as

$$\vec{\varepsilon}(t) = \vec{\varepsilon}_0 p(t)_\varepsilon \sin(\Omega t) \quad (4.8)$$

where $\vec{\varepsilon}$ defines the electric field strength and polarization, $p(t)$ is a dimensionless function with maximum value 1.0 describing the pulse shape, and Ω is the carrier frequency. Two field intensities, each with linear polarization, are used, 35 GW/cm² and 1 TW/cm², corresponding to field strengths of 0.001 and 0.0054 a.u., respectively. In combination with the initial condition that aligns the molecule with the field this avoids introducing any rotational motion; a realistic assumption, since rotational time scales are much longer than vibrational ones and we do not want to evolve the system over a long time anyway. The quantum wave-packet propagation is similarly limited to the vibrational degree of freedom. The END initial conditions are further specified by using the nuclear equilibrium distance and putting the electrons in the SCF state at that geometry.

Various field frequencies were considered. The results for each simulation for a particular frequency and field intensities are summarized in section 4.3.

4.3 Results and Discussion

4.3.1 Static Properties

The 3-21G family of electronic basis functions is used in the END ansatz for both LiH and HF. This limited basis provides an acceptable model for seeking an understanding of the factors determining the dynamics. Changing the basis to a more complete one (6-31G*) didn't prove to introduce significant differences on the dynamics. The contraction scheme used was H:(3s):[2s], Li:(6s,3p):[3s,2p] and F:(6s,3p):[3s,2p].

Because the spin symmetry of the ansatz does not break either for the MD or the NPMD calculations, restricted Hartree-Fock (RHF) limiting behavior exists at large bond distances in the potential and dipole used in the MD and NPMD wave-packet calculations. Fortunately this unphysical behavior does not affect the dynamics significantly since such large bond distances are not explored by the nuclei. The wave-packet calculations may be more susceptible to the ill-behaved region of the dipole and the potential due to the fact that the nuclear wave function has a finite width. Unlike MD and NPMD, the full END approach admits a consistent exploration of symmetry broken solutions that, for instance, allows for a correct description of bond breaking and bond formation in closed shell systems [92]. The agreement between the END and the MD calculations is an indication that the dynamics is not affected by the unphysical RHF behavior of the potential curve at large separation.

As a way to judge the quality of the basis set we performed time-independent calculations on HF and LiH. Results for HF show that the dipole function is somewhat sensitive to the basis set, but for the region of interest the agreement with the results obtained with a more flexible wave function [93] is acceptable (see figure 4.1). Equivalent results were obtained for LiH by Butalib and Gadéa [94]

using full configuration interaction (the dipole moment results were obtained from Berriche and Gadéa supplied to us in a private communication). Values obtained for the equilibrium distance are 1.771 a.u. for HF and that for the vibrational frequency is 4150.8 cm^{-1} , while for LiH we calculate 3.066 a.u. and 1428.8 cm^{-1} , respectively. For LiH, the dipole as a function of distance has a linear behavior

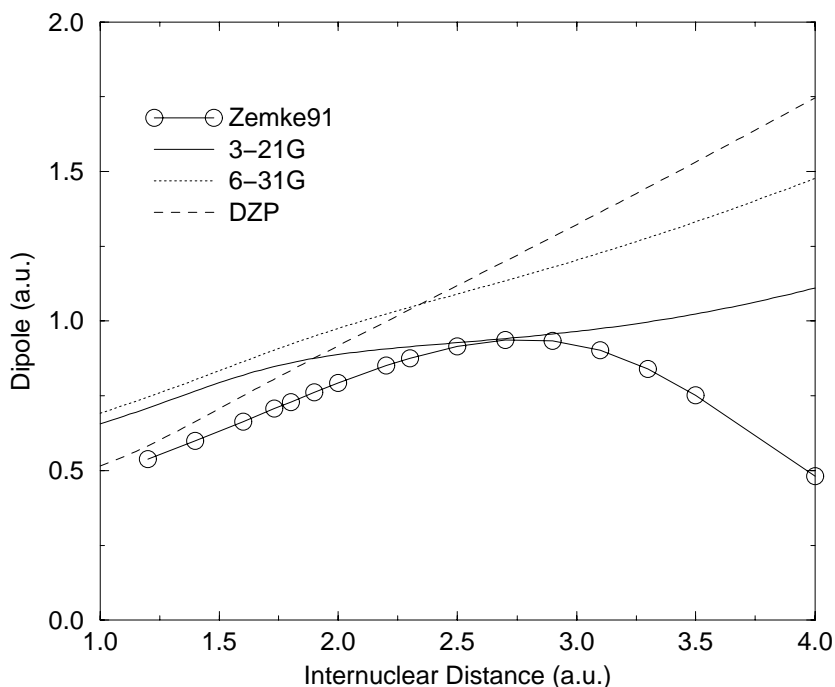


Figure 4.1: Dipole moment functions for HF calculated using RHF for different basis functions (this work) and CASSCF-MRCI.

for small distortions of the potential when the polarization term is neglected in the electronic Hamiltonian (NPMD method). On the other hand, its derivative, related to the force term $(\vec{\mu} \cdot \vec{\epsilon})$ is twice as big as the one calculated with better electronic wavefunctions [94] while for HF is too small around $R = 2.0$ a.u.

Calculations using the renormalized Numerov [95] method and a potential obtained with RHF exhibit an excitation energy for the first vibrational state of 6.310×10^{-3} au (1393.72 cm^{-1}), which is different from the harmonic frequency

of 6.531×10^{-3} . END calculations using initial conditions to map the $\nu=0$ quantum state oscillates with a frequency very close to harmonic. This leads us to use different frequencies when comparing calculations performed with END and wave-packet (WP) methods and to introduction of a quantity called detuning frequency. The detuning frequency is defined as the difference between the frequency of the applied field and the fundamental frequency of the oscillator ($\nu_0 \rightarrow \nu_1$ transition frequency for WP). For the WP calculations the fundamental frequency was taken to be 6.310×10^{-3} and for the END, MD and NPMD it was taken to be 6.531×10^{-3} .

4.3.2 Dynamics Results

In the zeroth order approximation the system may be considered to be a linearly driven harmonic oscillator, i.e., the potential is assumed harmonic and the dipole linear, while the electrons have no couplings to the nuclear dynamics. As mentioned before this approximation is appropriate and interesting because the classical and quantum response of a harmonic oscillator to a linear external force is identical. The energy of the oscillator system with mass m and frequency ω , initially in its ground state, is given by

$$\epsilon(t) = \frac{\mu_0^2 \epsilon_o^2}{2m} \left| \int_0^t ds p_\epsilon(s) \exp[i\omega s] \right|^2. \quad (4.9)$$

For a continuous wave monochromatic field, i.e., $p(t)_\epsilon = 1$, and small detuning $\Delta = \Omega - \omega$, the energy transfer is periodic with the detuning period $\frac{2\pi}{\Delta}$,

$$\epsilon(t) = \frac{\mu_0^2 \epsilon_o^2}{2m \Delta^2} \sin^2 \left(\frac{\Delta}{2} t \right). \quad (4.10)$$

An example for LiH of the absorbed energy for a continuous wave field is shown in figure 4.2 obtained both with the END and the quantum wave-packet methods. The results are for matching detuning, rather than identical field frequency,

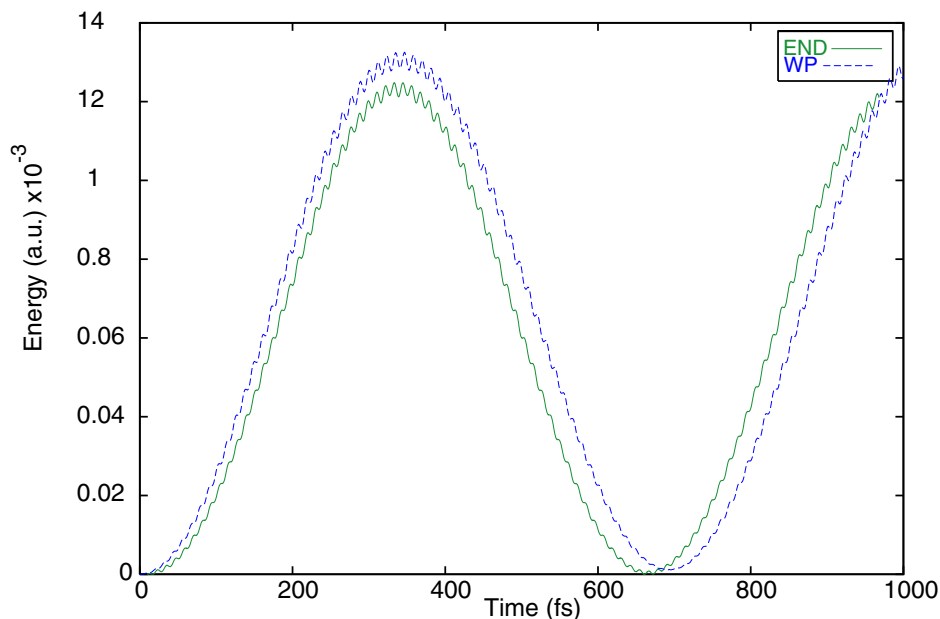


Figure 4.2: Absorbed energy for LiH using a continuous field of intensity of 35.1 GW/cm^2 and a detuning of $212 \times 10^{-6} \text{ a.u.}$

because the END and the quantum methods have slightly different fundamental frequencies ν_0 . We have simply used the ground state for both the classical and the quantum case, and have not averaged over ensembles of trajectories to improve the classical-quantum correspondence for the initial condition. For a ground state in a nearly harmonic system this should be an acceptable approximation. In this example we have used the LiH molecule. The weaker field, and a detuning above the fundamental frequency, i.e., away from multiphoton resonances, conspire to optimize oscillatorlike behavior and the mutual agreement between the methods. Considerable differences do occur for other field conditions, but for a detailed investigation we refer to Walker and Preston [79], Dardi and Gray [80], Lin et al. [96], and Goggin and Milonni [97].

Time averaged absorbed energies [79, 80, 96] are used to compare the classical and the quantum calculations. Averages were taken over detuning period intervals. The spectrum of average absorbed energy as a function of field frequency is a broad

peak with spikes at the multiphoton frequencies. The broad peak is reproduced in calculations with classical treatment of the nuclei, but the evidence of multiphoton frequencies is inherently quantum mechanical. As the field strength increases the peak heighten and and shifts to the red. This is apparent in the results in Table I, which gives the average absorbed energy for LiH. The stronger field shows the larger absorption values at detunings that are shifted to the red.

As expected from the literature both END and MD exhibit agreement with the quantum wavepacket results. None of the detunings in Table I coincide with a multiphoton frequency. The differences between END and MD in Table I appear to be almost negligible. A similar observation was made when inspecting results for the time evolution of bond distance and electric dipole moment. The same observation was again made for the differences between END and MD in all test calculations on HF. This leads us to the first conclusion, namely, that for the kind and magnitude of timedependent field used here, nonadiabatic effects in the molecular Hamiltonian are of little consequence for the dynamics. Since the MD calculations require significantly less computational time, the remaining calculations are all of this type.

Table 4.1: Average absorbed energy (in 10^{-3} a.u.) taken over the first detuning period for LiH using a continuous field with intensities 35.1 GW/cm^2 (upper part of the table) and 1 TW/cm^2 (lower part of the table) at different detunings Δ (in 10^{-6} a.u.).

Δ	END	MD	WP
212	0.59	0.60	0.61
-68	4.81	4.63	4.45
-248	0.56	0.56	0.72
212	5.84	5.87	6.87
-68	10.97	11.06	12.29
-248	14.55	14.53	15.38

For a Gaussian pulsed field of finite duration one can compute the energy absorbed after the pulse has subsided. To a very good approximation this also applies to a pulse with a Gaussian profile of width τ (full width at half maximum, or, FWHM) and one finds

$$\epsilon(\infty) = \frac{\mu_0^2 \epsilon_0^2}{2m\Delta^2} \exp[-(\Delta\tau)^2]. \quad (4.11)$$

The pulse duration needs to be matched to the detuning Δ the carrier frequency to obtain optimum energy. When the pulse is too short the system does not have time to respond; when the pulse is too long as in figure 4.3, system releases energy back to the field. We have used width of 5942 a.u., which roughly matches the larger negative detuning (248×10^{-3}). An example of the time evolution of the absorbed energy is shown in figure 4.3. A comparison is shown in figures 4.4 and 4.5 for the final energy absorbed of LiH and HF as described by the methods MD, NPMD, i.e., with and without electronic polarizability included and with the wave-packet method.

It is immediately evident that the effect of the polarizability is significantly more pronounced for HF than for LiH. The use of different approximations to solve the dynamics, of course, leads to different approximations for the description of the time-dependent dipole. More precisely, MD introduces relaxation with the field and adiabatic corrections and END also introduces nonadiabatic corrections. As already mentioned, the dynamics produced by END and MD are here very similar. This small difference is assigned to the very small nonadiabatic effects on the dynamics. In contrast, the MD dynamics is different from the NPMD, indicating that electronic relaxations, or polarization with the field is an important dynamical effect. The polarization is shown in figures 4.6 and 4.7 as the departure from the NPMD dipole function given by the solid diagonal line.

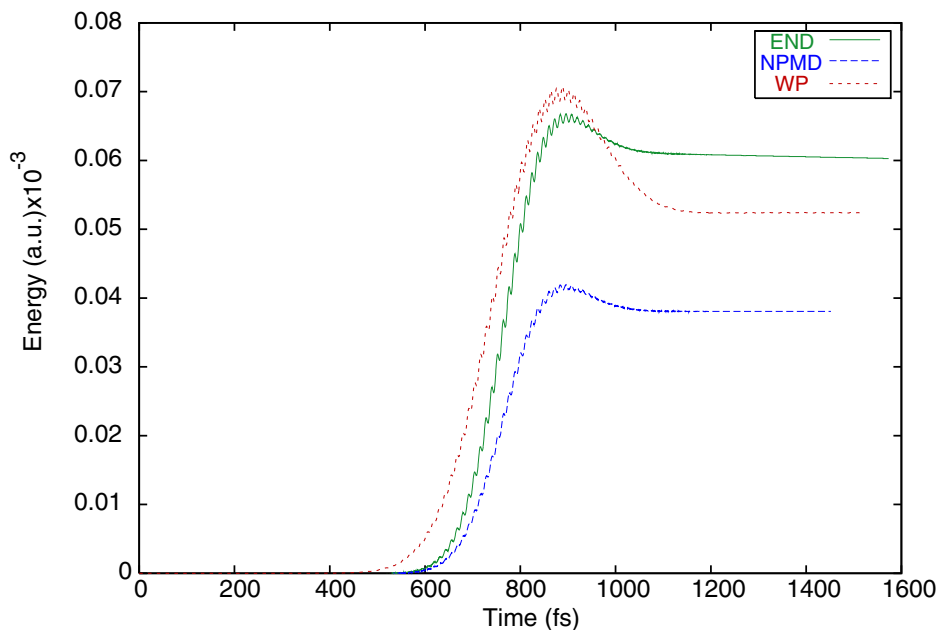


Figure 4.3: Absorbed energy as a function of time for LiH with the END, NPMD, and WP calculations. A Gaussian pulsed field with intensity 35.1 GW/cm^2 and detuning $248 \times 10^{-6} \text{ a.u.}$ is used.

Note how the amplitude of the motion is much smaller in MD for HF, suggesting a more important role of the polarizability for this molecule. The response of the dipole moment to the field allows estimates of the polarizability and hyperpolarizabilities to be made. The dynamics explicitly yields the dipole at each time step, allowing the dipole to be obtained directly from the time-dependent dipole (see figure 4.8) as a function of the field for different internuclear distances. If we assume a linear response of the dipole with the field, $\mu = \mu_0 + \alpha\varepsilon(t)$, the dependence of the polarizability (α_{xx} in this case) on the internuclear distance is obtained directly from the data in figure 4.8 to produce the results in figure 4.9. Similar results are computed for LiH and shown in figure 4.10. Computed values for HF at equilibrium are similar to other results in the literature [98] using larger basis sets. The computed polarizability is not exactly the dynamic one since it represents the response to a Gaussian shaped pulse with a frequency spread. Cal-

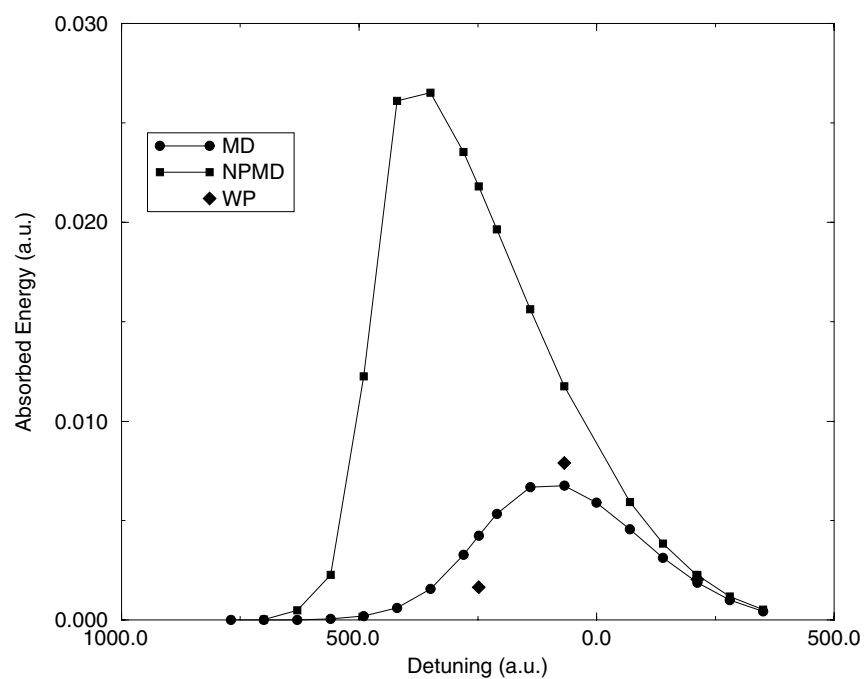


Figure 4.4: Absorbed energy, in $h\nu_0$ units, as a function of detuning (in 10^{-6} a.u.) for HF calculated with MD and NPMD. A pulsed field with intensity $1 \text{ TW}/\text{cm}^2$ is used.

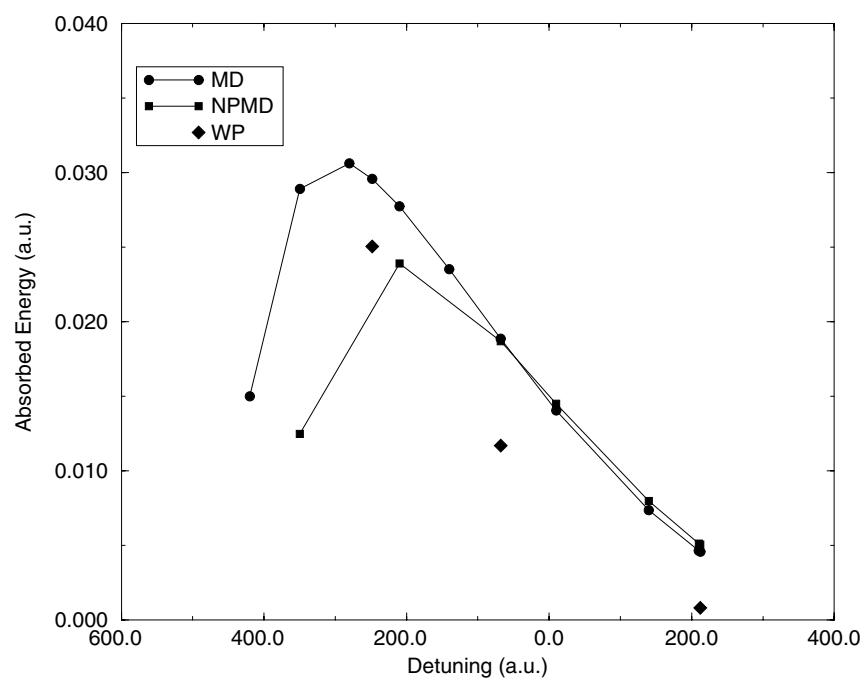


Figure 4.5: Absorbed energy, in $h\nu_0$ units, as a function of detuning (in 10^{-6} a.u.) for LiH calculated with MD and NPMD. A Gaussian pulsed field with intensity 35.1 GW/cm^2 is used.

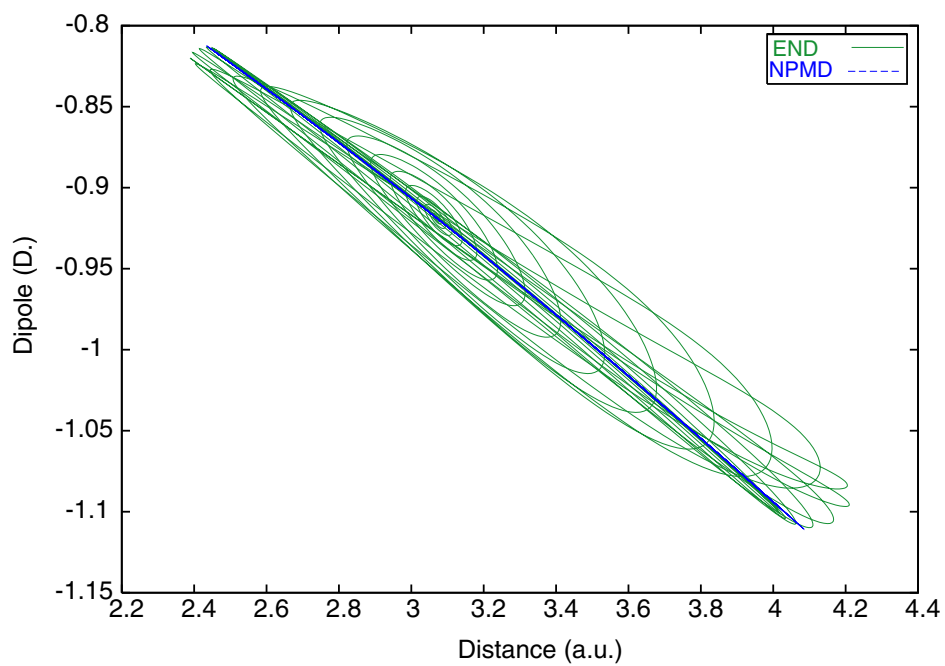


Figure 4.6: Molecular dipole vs bond distance traced during time evolution for LiH at detuning 68×10^{-6} a.u. and field intensity of 1.0 TW/cm^2 for NPMD (line) and MD (oscillatory parametric curve). The calculated equilibrium bond distance is 3.066 a.u.

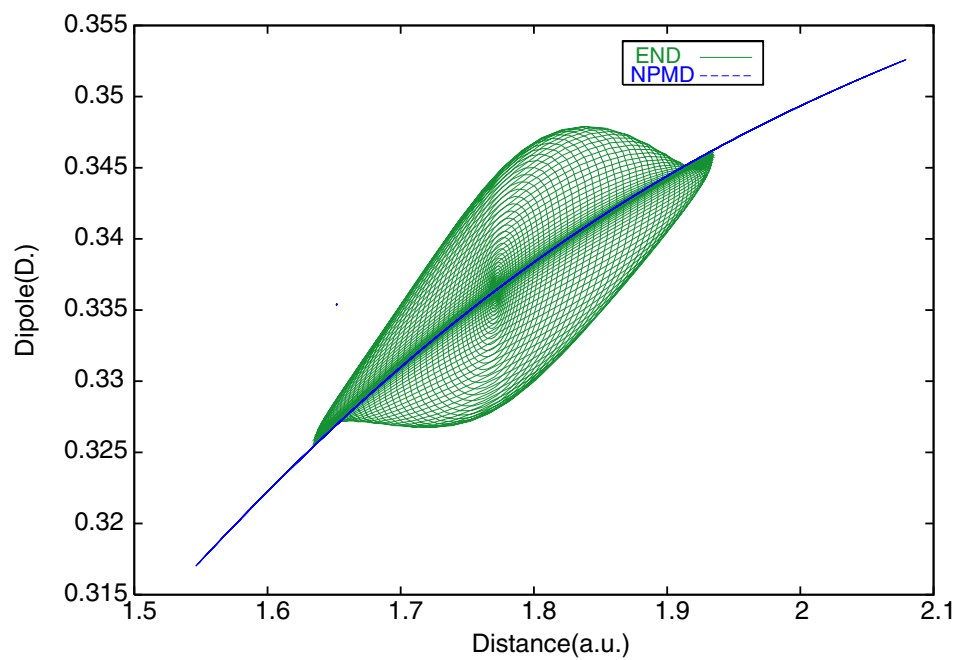


Figure 4.7: Molecular dipole vs bond distance traced during time evolution for HF at detuning 68×10^{-6} and field intensity of 1.0 TW/cm^2 for NPMD (line) and MD (oscillatory parametric curve). The calculated equilibrium bond distance is 1.771 a.u.

culations using our basis sets for static polarizabilities at different internuclear distances have shown that the variation with frequency is small, but bigger for LiH, and fluctuates about the value for the static polarizability for both LiH and HF.

The polarizability α accounts for a contribution to the energy which can be expressed as $\frac{-1}{2}\alpha(\vec{R})\varepsilon_0^2 p(t)_\varepsilon^2 \cos(\Omega t)^2$. Its effect on the dynamics of the two systems may be discussed in terms of classical perturbation theory [99]. The classical analog for a polarizable molecular system is that of an anharmonic oscillator driven by a force of frequency Ω , arising from the dipole interaction, and a force with frequency 2Ω , arising from the polarizability. The Taylor expansion of the electronic potential at the equilibrium distance under these conditions is given by

$$E_{el} = \frac{1}{2}kR^2 + \frac{1}{6}aR^3 + \frac{\partial\alpha(\vec{R})}{\partial R}R\varepsilon^2 + \frac{1}{2}\frac{\partial^2\alpha(\vec{R})}{\partial R^2}R^2\varepsilon^2 \quad (4.12)$$

with k being the force constant, a the anharmonicity coefficient, $\alpha(\vec{R})$ the polarizability and ε the electric field.

There are two kinds of resonances that can be induced by the polarization of the electronic potential. It can be shown that an harmonic oscillator with a time dependent force constant (as induced by the polarization) can undergo parametric resonance when the time dependency on the parameters oscillates with a frequency $2\omega_0$ as it happens in our case (due to the term $\frac{\partial^2\alpha(\vec{R})}{\partial R^2}R^2\varepsilon^2$). It can also be shown that an anharmonic oscillator driven by a force of frequency close to $2\omega_0$ (from $\frac{\partial\alpha(\vec{R})}{\partial R}R\varepsilon^2$) undergoes resonance. Assuming validity of perturbation theory the effective force term arising from the polarizability term in an anharmonic oscillator is given by [99]

$$F_{eff} = -\frac{a'b}{3\omega_0^2} \frac{1}{2} \frac{\partial\alpha(\vec{R})}{\partial R} \varepsilon_0^2 p(t)_\varepsilon \cos(\Omega t + \delta), \quad (4.13)$$

with a' being half the anharmonicity coefficient on a Taylor expansion for the potential, b the amplitude of the motion, ω_0 the harmonic frequency, $\alpha(\vec{R})$ the polarizability, Ω the field frequency and δ an arbitrary phase related to the initial conditions. Note that for LiH and HF the derivative $\frac{\partial\alpha(R)}{\partial R}$ is always positive while the anharmonic coefficient is negative, making the sign of the effective force given by 4.13 opposite in sign to the field. The result is an enhancement of the effective dipole force term for LiH (which also has a different sign with respect to the field) and a reduction of the dipole force for HF. This result is in accord polarization effects observed on the dynamics.

4.3.3 Effect of the Basis Set

No new physical effect was observed when a bigger (6-31G) basis set was used to describe the electronic wavefunction. The effect of changing the basis set can be understood by its influence on the electronic potential. A larger basis set produce a more anharmonic potential with a shifted (to lower values) resonance frequency. As a result the END and MD dynamics absorbs less energy in the two-photons resonance condition (due to the greater anharmonicity) for the two field intensities used. The dynamics with the larger basis set for the other detuning frequencies produce results nearly identical to the case with a small basis set.

4.4 Conclusions

The electron nuclear dynamics theory which is capable of full nonadiabatic treatment of molecular systems has been applied to study molecular processes in a time-dependent external field. In this initial study we have investigated the effects of nonadiabatic coupling terms, as well as the interaction of intense laser fields with the electron and the nuclear dynamics for the simple diatomic molecules LiH and

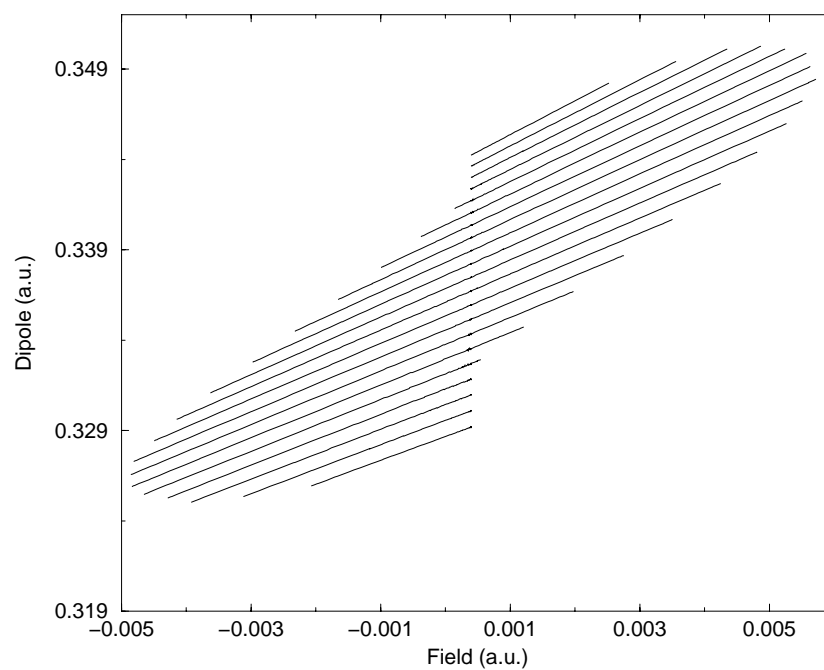


Figure 4.8: Dipole as a function of the field for HF for different internuclear distances (different lines). The field intensity used is $1 \text{ TW}/\text{cm}^2$ and the detuning is $248 \times 10^{-3} \text{ a.u.}$

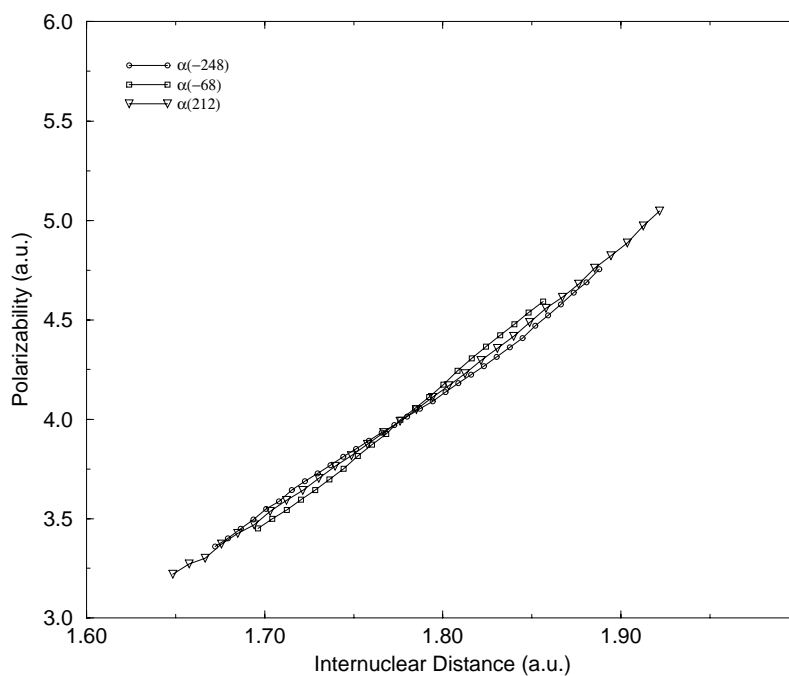


Figure 4.9: Polarizability ($\alpha(\Delta)$) vs internuclear distance for HF using a field of 1 TW/cm² and different detunings.

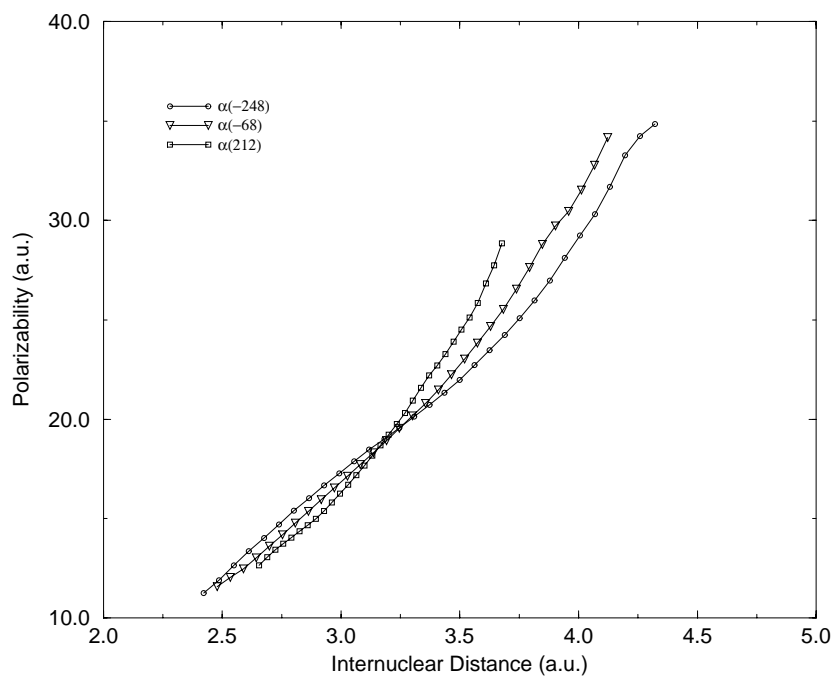


Figure 4.10: Polarizability ($\alpha(\Delta)$) vs internuclear distance for LiH using a field of $1 \text{ TW}/\text{cm}^2$ and different detunings.

HF. At the chosen field intensities the results of the full END and the molecular dynamics on a field dependent potential energy surface yield similar results, the difference being greater for the HF molecule. This indicates that for the cases studied the infrared (IR) light absorption is adiabatic. The applied field can be considered of moderate intensity, however, in view of the absorbed energy (as seen in figures 4.4 and 4.5) and the number of vibrational quanta involved, the situations are quite different for the two molecules. The external field interaction with the electrons appears to be crucial for the correct description of the dynamics, since inclusion of the polarization proves to have a substantial effect. The polarization effects are more pronounced for the HF molecule than for LiH. The new capability of the END approach to molecular processes offers interesting possibilities to study more complex molecular systems. The correct description of the induced dipole is fundamental to describe the correct absorption process (see also Hammerich et al. [100] and references therein).

Results from M. Perisco and P. V. Leuven showed [101] that the multiphoton process can be viewed as having three regimes regarding the field frequency. They are in order of increasing detuning: (i) the process of energy absorption is recurrent and the short time dynamics is characterized by an "apparent" detuning period (apparent detuning can be different from the actual detuning); (ii) the energy absorption process is non-recurrent and (iii) the system energy oscillates according to its Rabi frequency. These regimes depend strongly on the field intensity and anharmonicity of the potential. In particular the stronger the field intensity the lower the frequency (bigger detuning) necessary to make the dynamics enters into the non-recurrent regime. Based on this we can explain part of the results obtained. In their work the apparent detuning is defined by the rising time, or the time it takes for the energy absorbed to reach the first maximum. The detuning frequency

is calculated using the result for the forced harmonic oscillator.

$$|\Delta| = \frac{\pi}{T} \quad (4.14)$$

with Δ being negative when T decreases with the lowering of the field frequency.

With our choice of initial conditions for LiH and HF, the WP dynamics has results similar to the recurrence regime (i) with both field intensities. That regime of the WP dynamics is more similar to END dynamics (as it always shows a recurrence pattern) than the other two regimes. That explains in part the close agreement between WP and END.

CHAPTER 5 FINAL STATE ANALYSIS

5.1 Introduction

The final state obtained from a END simulation can, in principle, give information about state to state events. However in order to obtain such information, e.g., the probability for a specific event to occur, one needs to extract the information from the final dynamical state. The theory and implementation of how this is done for a single determinatal state within the END framework is detailed in the sections below. In this document we focus on how to deal with events related to the electronic wavefunction of the final state. Blass et al. [102]. gives a detailed account on how to extract information for rovibrational quantities.

There are several experimental quantities that depend directly on the probability of finding the system in a specific state; charge transfer cross sections being an obvious one. For such a case, one is interested in the sum of components of charge transfer states in the final time-dependent wavefunction. When dealing with hydrogenic species one can use the particle Mulliken population to estimate single electron charge transfer probabilities. However, when multi-electron transfer probabilities are non negligible or when dealing with more complex species, Mulliken populations may not offer a reliable approximation for charge transfer probabilities. For charge transfer probabilities in multi-electron systems one should use a more general scheme as the one discussed here. Within the procedure outlined here we can also compute time dependent excitation energies and excitation probabilities. This feature could be used to study models of ultra-fast spectroscopy experiments.

5.2 Background Theory

5.2.1 Unitary Transformations Using Basis Operators

Any unitary transformation can be represented in exponential form as

$$U = \exp(\mathbf{X}) \quad (5.1)$$

with \mathbf{X} being an anti-hermitian matrix. The definition of a matrix exponential is given by

$$\exp(\mathbf{X}) = \sum_{n=1}^{\infty} \frac{\mathbf{X}^n}{n!} \quad (5.2)$$

One of the advantages of such parametrization for unitary matrices is that any choice of anti-hermitian matrix \mathbf{X} produces a unitary transformation. Some interesting algebraic properties of unitary matrices in exponential form are

$$\exp(\mathbf{X})^\dagger = \exp(-\mathbf{X}) \quad (5.3)$$

$$\mathbf{A} \exp(\mathbf{X}) \mathbf{A}^{-1} = \exp(\mathbf{A} \mathbf{X} \mathbf{A}^{-1}) \quad (5.4)$$

$$\exp(-\mathbf{X}) \mathbf{A} \exp(\mathbf{X}) = \mathbf{A} + [\mathbf{A}, \mathbf{X}] + \frac{1}{2!} [[\mathbf{A}, \mathbf{X}], \mathbf{X}] + \dots \quad (5.5)$$

Equation 5.5 is the well known *Baker-Campbell-Hausdorff* (BCH) expansion.

Non-unitary transformations that preserve the overlap or metric matrix \mathbf{S} can also be expressed in term of matrix exponentials. The transformation matrix \mathbf{V} can be expressed in exponential form as

$$V = \exp(\mathbf{X} \mathbf{S}). \quad (5.6)$$

Expression 5.6 is readily obtained from 5.4 and representing \mathbf{V} as $\mathbf{V} = \mathbf{S}^{-1/2} \mathbf{U} \mathbf{S}^{1/2}$. The BCH expansion can also be generalized for transformations that preserves \mathbf{S} .

We can also express unitary operators in terms of exponentials of basis creation and annihilation operators. Introducing the anti hermitian operator $\hat{\kappa}$

$$\hat{\kappa} = \sum_{ih} \kappa_{ij} b_i^\dagger b_j, \text{ where } \hat{\kappa}^\dagger = -\hat{\kappa}. \quad (5.7)$$

where κ is a complex matrix with pure imaginary diagonal elements and the sum runs over the whole basis set. We can now define a unitary operator as

$$\hat{U} = \exp(-\hat{\kappa}) \quad (5.8)$$

The operator exponential is defined in analogy with 5.2 by a Taylor expansion of the exponential

$$\exp(\hat{\kappa}) = \sum_{n=1}^{\infty} \frac{\hat{\kappa}^n}{n!}. \quad (5.9)$$

An important property for our purposes is that a unitary transformation over the spin orbitals basis $\{\psi\}$ can also be represented as a unitary transformation over the basis creation operators $\{b^\dagger\}$. More specifically if we transform the spin orbitals by a unitary transformation \mathbf{U} , i.e.

$$\tilde{\psi} = \psi \mathbf{U}, \quad (5.10)$$

then a modified Slater determinant can be constructed with the transformed spin orbitals $\tilde{\psi}$. The associated basis creation operators for such spin orbitals are a transformed set $\{\tilde{b}^\dagger\}$. The mapping between Slater determinants and a product of basis creation operators (eq. 1.7) reads for the modified determinant

$$\left| \tilde{\psi}_1 \dots \tilde{\psi}_N \right| \longleftrightarrow \prod_{h=1}^N \tilde{b}_h^\dagger |vac\rangle. \quad (5.11)$$

From Equations 1.2 and 5.11 one can conclude that the basis creation operators should transform as

$$\tilde{b}_g^\dagger = \sum_i b_i^\dagger U_{ig} = \sum_i b_i^\dagger [\exp(-\kappa)]_{ig}. \quad (5.12)$$

Using the BCH (eq. 5.5) expansion we can show that the modified basis creation operators can also be expressed as

$$\tilde{b}_g^\dagger = \exp(-\hat{\kappa}) b_g^\dagger \exp(\hat{\kappa}) \quad (5.13)$$

Inserting the expression for the creation operators into Equation 1.6 we can readily see that

$$\left| \tilde{\Psi}_0 \right\rangle = \prod_{h=1}^N \tilde{b}_h^\dagger |vac\rangle = \exp(-\hat{\kappa}) \prod_{h=1}^N b_h^\dagger \exp(\hat{\kappa}) |vac\rangle \quad (5.14)$$

or

$$\left| \tilde{\Psi}_0 \right\rangle = \exp(-\hat{\kappa}) \left| \Psi_0 \right\rangle. \quad (5.15)$$

Equation 5.15 offers a convenient way to parametrize transformations over determinants as any choice of matrix κ produces unitary transformation over the basis set. In the next section we introduce a parametrization used in the electron nuclear dynamics method that has the form of Equation 5.15 with constraints imposed on the matrix κ .

5.2.2 Thouless Determinant

The END single determinantal wavefunction given in terms of basis field operators $\{b^\dagger\}$ and a set of complex parameters $\{z\}$ has the form (N is the number of electrons and K is the number of basis orthonormal functions):

$$|z\rangle = \exp \left\{ \sum_{h=1}^N \sum_{p=n+1}^K z_{ph} b_p^{\dagger} b_h \right\} \left| \Psi_0 \right\rangle \quad (5.16)$$

which represents the most general parametrization of a single determinant over the single electron wave function space in consideration. This representation of

a single determinant was first introduced by Thouless [103] and for that reason a determinant constructed this way is called a Thouless determinant.

The Thouless parametrization differs from Equation 5.15 because it considers for the parametrization of the transformation only the occupied versus virtual block of the κ matrix. A transformation constructed that way is not unitary and does not conserve the norm. However, there are some important properties that such transformation has that a general unitary transformation does not. Two of the most important properties of the Thouless parametrization for it to be considered in a time dependent formalism are

- The \mathbf{z} parameters only mix occupied and virtual orbitals on the reference. This implies that a change on \mathbf{z} would necessarily change the determinantal state.
- $|z\rangle$ only depends on \mathbf{z} (not \mathbf{z} and \mathbf{z}^*). This is important when deriving equations of motion for the system using the time dependent variational principle [16].

We can map the single determinantal wave function in operator space with a Slater determinant over a basis set by considering the product

$$D = \langle vac | \sum_{i=1..h} \prod_{h=1}^N \psi_h(r_h) b_h \prod_h \left(b_h^{\bullet\dagger} + \sum_{p=n+1}^K z_{ph} b_p^{\bullet\dagger} \right) | vac \rangle \quad (5.17)$$

By considering a determinant generated by the equation above and the Thouless determinant written as

$$|z\rangle = \prod_{h=1}^N \left(1 + \sum_{p=n+1}^K z_{ph} b_p^{\bullet\dagger} b_h^{\bullet} \right) |\Psi_0\rangle \quad (5.18)$$

one can see that the orbitals in a Thouless determinant have the form

$$\chi_h = \psi_h + \sum_{p=n+1}^K \psi_p z_{ph}. \quad (5.19)$$

For such a case $\{\psi_h\}$ represents the orbitals of the reference set, i.e., the ones present in $|\Psi_0\rangle$, and $\{\psi_p\}$ represents the orbitals of the virtual set. The choice of the reference and virtual set is rather arbitrary and does not have to correspond to

the traditional definition commonly used in Hartee-Fock calculations. Note that the orbitals defined by Equation 5.19 do not form a orthogonal set. In matrix form the orbitals can be represented as a function of the z parameters in a basis set $\{\psi\}$ according to

$$\chi^\bullet = \begin{pmatrix} \psi^\bullet & \psi^\circ \end{pmatrix} \begin{pmatrix} I^\bullet \\ z \end{pmatrix}. \quad (5.20)$$

The column array in Equation 5.20 is referred in this document as a *state* array.

In order to introduce an orthogonal virtual space consider the matrix

$$\begin{pmatrix} I^\bullet & -z^\dagger \\ z & I^\circ \end{pmatrix} \quad (5.21)$$

and the product

$$\begin{pmatrix} I^\bullet & z^\dagger \\ -z & I^\circ \end{pmatrix} \begin{pmatrix} I^\bullet & -z^\dagger \\ z & I^\circ \end{pmatrix} = \begin{pmatrix} I^\bullet + z^\dagger z & 0 \\ 0 & I^\circ + z z^\dagger \end{pmatrix}. \quad (5.22)$$

The above equation shows that the orbitals defined by

$$\chi^\circ = \begin{pmatrix} \psi^\bullet & \psi^\circ \end{pmatrix} \begin{pmatrix} -z^\dagger \\ I^\circ \end{pmatrix} \quad (5.23)$$

form a set of virtual orbitals orthogonal to the occupied set as a function of the z complex parameters.

The completeness relation in this representation assumes the form

$$I = \begin{pmatrix} I^\bullet \\ z \end{pmatrix} (I^\bullet + z^\dagger z)^{-1} \begin{pmatrix} I^\bullet & z^\dagger \end{pmatrix} + \begin{pmatrix} -z^\dagger \\ I^\circ \end{pmatrix} (I^\circ + z z^\dagger)^{-1} \begin{pmatrix} -z & I^\circ \end{pmatrix} \quad (5.24)$$

where the first term in the sum correspond to the contributions due to the occupied space and the second term the contributions due to the the virtual space. An

operator F represented in a basis $\{\psi\}$ would have its projection in the occupied space given by

$$F^\bullet = \begin{pmatrix} I^\bullet \\ z \end{pmatrix} \langle \psi | F | \psi \rangle \begin{pmatrix} I^\bullet & z^\dagger \end{pmatrix} \quad (5.25)$$

with an equivalent expression for the virtual space.

5.2.3 Basis Set Transformations

The purpose of this section is to find out how the z coefficients transform when the basis $\{\psi\}$ is transformed by a unitary transformation \mathbf{U} or by a transformation that diagonalizes \mathbf{S} . We saw in Section 5.2.1 that basis creation operators transform with the basis. From Equation 5.16 one can infer that the \mathbf{z} matrix will transform with the inverse of the transformation of the basis. Let us consider explicitly the case where there is a non-orthonormal basis set $\{\phi\}$ related to $\{\psi\}$ by a transformation W

$$\psi = \phi W. \quad (5.26)$$

This is important, for example, if we want to transform from a basis of atomic orbitals to a basis of molecular orbitals. By considering the direct product $\langle \psi | \psi \rangle$ one can readily see that the transformation W satisfies (S is the overlap matrix for the new basis ϕ)

$$W^\dagger S W = I. \quad (5.27)$$

One way of constructing the transformation W is by considering the product $W = S^{-\frac{1}{2}} U$, where U is unitary and $S^{-\frac{1}{2}} S^{-\frac{1}{2}} = S^{-1}$. In order for this transformation to hold the eigenvalues of S have to be greater than 0, i.e., there cannot be linear dependence among the functions in the basis. Using the identity

$$I = S^{\frac{1}{2}}UU^{\dagger}S^{-\frac{1}{2}} = WW^{-1} \quad (5.28)$$

the orbitals can be expressed in terms of the new basis and a modified state vector as

$$\begin{aligned} \begin{pmatrix} \chi^{\bullet} & \chi^{\circ} \end{pmatrix} &= \begin{pmatrix} \psi^{\bullet} & \psi^{\circ} \end{pmatrix} W^{-1} W \begin{pmatrix} I^{\bullet} & -z^{\dagger} \\ z & I^{\circ} \end{pmatrix} \\ &= \begin{pmatrix} \phi^{\bullet} & \phi^{\circ} \end{pmatrix} W \begin{pmatrix} I^{\bullet} & -z^{\dagger} \\ z & I^{\circ} \end{pmatrix} \end{aligned} \quad (5.29)$$

Note, however, that by transforming the state array, one would produce a determinant with a parametrization scheme distinct from the one we started with, i.e., the Thouless parametrization scheme would be lost. We will come back to this topic later. An interesting fact is that we can also define a Thouless determinant in terms of a non-orthonormal basis set $\{\phi\}$. As in the orthonormal case the orbitals would be defined as a function of the state vector as

$$\begin{pmatrix} \chi^{\bullet} & \chi^{\circ} \end{pmatrix} = \begin{pmatrix} \phi^{\bullet} & \phi^{\circ} \end{pmatrix} \begin{pmatrix} I^{\bullet} & -z_{no}^{\dagger} \\ z_{no} & I^{\circ} \end{pmatrix} \quad (5.30)$$

and the the orthonormal and non-orthonormal state vectors would be related by

$$\begin{pmatrix} I^{\bullet} & -z^{\dagger} \\ z & I^{\circ} \end{pmatrix} = W^{-1} \begin{pmatrix} I^{\bullet} & -z_{no}^{\dagger} \\ z_{no} & I^{\circ} \end{pmatrix} \quad (5.31)$$

if we impose some constrains on the transformation W . The existence of such a transformation guarantees the same unique properties of the Thouless parametrization when dealing with determinants of non-orthogonal orbitals. If W is a transformation obtained from, e.g., a Hartree-Fock calculation, then Equation 5.31 does not hold. We can still use a relationship like the one given by 5.31 to generate

a state vector in terms of a transformation W and z parameters expressed in a non-orthogonal basis. However, a state vector produced this way would not have a parametrization according to Thouless and is not suitable for a dynamical state.

5.2.4 Final State Analysis

If we consider a special case as the final or asymptotic state of a reaction with products a and b we can say that its orbitals are given by

$$\begin{aligned} \begin{pmatrix} \chi_a^\bullet & \chi_a^\circ & \chi_b^\bullet & \chi_b^\circ \end{pmatrix} &= \begin{pmatrix} \phi_a^\bullet & \phi_a^\circ & \phi_b^\bullet & \phi_b^\circ \end{pmatrix} \begin{pmatrix} I_a^\bullet & -\mathbf{z}_a^\dagger & 0 & -\mathbf{z}_{ba}^\dagger \\ \mathbf{z}_a & I_a^\circ & \mathbf{z}_{ba} & 0 \\ 0 & -\mathbf{z}_{ab}^\dagger & I_b^\bullet & -\mathbf{z}_b^\dagger \\ \mathbf{z}_{ab} & 0 & \mathbf{z}_b & I_b^\circ \end{pmatrix} \\ &= \begin{pmatrix} \psi_a^\bullet & \psi_a^\circ & \psi_b^\bullet & \psi_b^\circ \end{pmatrix} \mathbf{W}^{-1} \mathbf{Z} \end{aligned} \quad (5.32)$$

where the basis set $\{\phi\}$ is local, e.g. atomic orbitals, on the product fragments a and b respectively. For the asymptotic case the matrix W that defines a molecular spin orbital (MSO) basis in terms of the non-orthonormal local basis $\{\phi\}$ can be blocked as

$$\mathbf{W} = \begin{pmatrix} W_a & 0 \\ 0 & W_b \end{pmatrix} \quad (5.33)$$

that when introduced in Equation 5.32 gives

$$\begin{pmatrix} \chi_a^\bullet & \chi_a^\circ & \chi_b^\bullet & \chi_b^\circ \end{pmatrix} = \begin{pmatrix} \psi_a^\bullet & \psi_a^\circ & \psi_b^\bullet & \psi_b^\circ \\ \mathbf{W}_a^{-1} \begin{pmatrix} I_a^\bullet & -\mathbf{z}_a^\dagger \\ \mathbf{z}_a & I_a^\circ \end{pmatrix} & \mathbf{W}_a^{-1} \begin{pmatrix} 0 & -\mathbf{z}_{ba}^\dagger \\ \mathbf{z}_{ba} & 0 \end{pmatrix} \\ \mathbf{W}_b^{-1} \begin{pmatrix} 0 & -\mathbf{z}_{ba}^\dagger \\ \mathbf{z}_{ba} & 0 \end{pmatrix} & \mathbf{W}_b^{-1} \begin{pmatrix} I_b^\bullet & -\mathbf{z}_b^\dagger \\ \mathbf{z}_b & I_b^\circ \end{pmatrix} \end{pmatrix} \quad (5.34)$$

For computational convenience END as implemented in the program ENDDyne [25] uses a Thouless determinant over non-orthonormal spin orbitals basis, more specifically over atomic spin orbitals (ASO) centered at the nuclear positions.

Given an arbitrary state parametrized as in Equation 5.16 one can consider the configuration interaction (CI) expansion of $|z\rangle$

$$\begin{aligned} |z\rangle &= \langle \Psi_0 | z \rangle | \Psi_0 \rangle + \sum_{h=1; p=N+1}^{N,K} \langle \Psi_0 | b_h b_p^\dagger | z \rangle | \Psi_0^{\{hp\}} \rangle \\ &+ \sum_{g,h=1; p,q=N+1}^{N,K} \langle \Psi_0 | b_h b_p^\dagger b_g b_q^\dagger | z \rangle | \Psi_0^{\{hp\}\{gq\}} \rangle + \dots \end{aligned} \quad (5.35)$$

where the expansion is continued up to the N^{th} excitation order .

There are advantages of an energy ordered molecular spin orbital basis (MSO), e.g. Hartree-Fock MSO, when one needs to resolve a dynamical state as given in Equation 5.16 into reference and excited determinants (eqn. 5.35). For a state $|z\rangle$ with moderate levels of excitation content one should be able to limit the expansion to the first few terms. In an extreme case, if $|z\rangle$ is a Hartree-Fock ground state (GS) represented in the MSO solution of the HF problem the expansion is limited to the first term only. This is so because the Hartree-Fock GS represented in a HF basis has by definition all $\{z\}$ parameters equal to zero. Excited determinants will have nonzero z parameters that mix in excited configurations.

The overlap integral between two general determinantal wavefunctions can be obtained considering the commutation relations for basis creation operators in a non-orthogonal basis

$$\begin{aligned} [b_r, b_s^\dagger]_+ &= S_{rs} \\ [b_r^\dagger, b_s^\dagger]_+ &= 0 \\ [b_r, b_s]_+ &= 0. \end{aligned} \tag{5.36}$$

where $S_{rs} = \langle \phi_r | \phi_s \rangle$. Using Equation 5.36 is not hard to show that the overlap between two determinantal states is given by

$$\mathbf{S} = \langle \Psi_2 | \Psi_1 \rangle = \det(S). \tag{5.37}$$

Considering our Thouless determinantal state and its spin orbitals as in Equation 5.19 we can calculate the expansion terms in Equation 5.35. The overlap between spin orbitals appearing in expansion 5.35 are given by (making use of the Kroeneker delta function)

$$S_{ih} = \sum_{g=1}^N S_{ig} \delta_{gh} + \sum_{p=N+1}^K z_{ph} S_{ip}. \tag{5.38}$$

Here again using an orthonormal basis would simplify the calculation of the expansion terms in Equation 5.35. For an orthonormal basis, Equation 5.38 reads

$$S_{ih} = \sum_{g=1}^N \delta_{gh} + \sum_{p=N+1}^K z_{ph} \delta_{ip}. \tag{5.39}$$

Note that in Equation 5.39 the elements of the overlap matrix S are elements of the state array (see Equations 5.20 and 5.34). There are two possibilities for the evaluation of S_{ih} in Equation 5.39. If index i belongs to the occupied range then $S_{ih} = \delta_{ih}$. On the other hand if i belongs to the unoccupied range then $S_{ih} = z_{ij}$. In other words, for the orthonormal case, the determinant of the overlap matrix occurring in the full CI expansion of $|z\rangle$ is just the determinant of a piece of the

state array corresponding to the set of occupied orbitals in the determinant on which the projection is being calculated.

For the goals of this work we use the expansion 5.35 under the conditions for Equations 5.32-5.34, i.e., the conditions that the reference MSO basis can be localized to fragments. Although a determinantal state with orbitals given by Equation 5.34 cannot be expressed as a product of determinants due to mixing terms in matrix $\mathbf{z}_{\mathbf{ab}}$, one can certainly expand this class of states over determinants containing orbitals belonging only to distinct fragments.

The expansion given by Equation 5.35 in terms of determinants with fragment orbitals is given by

$$|z\rangle = \sum_i \sum_j \sum_k \langle \Psi_0 | \Lambda_k | z \rangle \Lambda_k^\dagger | \Psi_0 \rangle \quad (5.40)$$

where Λ^k defined as the fragment CI excitation operator, e.g., for singles:

$$\Lambda_k = 1 + \sum_{h=1; p=N+1; h, p \in i}^{N, K} b_h^\dagger b_p. \quad (5.41)$$

and the i, j, k indexes run over charge, spin and fragment number configurations. For expansion 5.40 to be complete we have to consider all possible combinations of the number of electrons (charge), the total S_z (spin) and all possible excitations per fragment. To have a complete expansion, combinatorial procedures are necessary to generate charge, spin and excitation configurations.

Equation 5.40 is just Equation 5.35 when used with a $|z\rangle$ state represented in a fragment orbital basis and with terms regrouped according to the number and spin type (α or β) of electrons present on each fragment. Final state analysis is the real motivation behind rewriting Equation 5.35. As an example of an application, we could square and sum all wave function amplitude terms in Equation 5.40 that have a particular number of electrons per fragment in their configuration and calculate the charge transfer probabilities for a final state. The practical implementation

and application of the theory developed in this section will be the focus of the following sections.

5.3 Simple Application

The quantities we are interested in calculating for performing a final state analysis are the expansion coefficients (or wave function amplitude terms) appearing in Equation 5.40. By themselves or grouped in some coherent manner the expansion coefficients can give the information needed for the computation of final state resolved quantities.

As a practical example consider for now the simple case of scattering of H by H. There are two electrons in the system and only one charge transfer channel. Consider the collision case where there is no H_2 formation. The initial state orbitals of the system are given by (using a $1s2s$ basis for each H)

$$\begin{pmatrix} \chi_a^\bullet & \chi_b^\bullet \end{pmatrix} = \begin{pmatrix} \phi_{1sH_1}^\bullet & \phi_{2sH_1}^\circ & \phi_{3sH_2}^\bullet & \phi_{4sH_2}^\circ \end{pmatrix} \begin{pmatrix} 1 & 0 \\ z_{31}^i & 0 \\ 0 & 1 \\ 0 & z_{42}^i \end{pmatrix}_{no}. \quad (5.42)$$

After the scattering takes place, the final state orbitals have the form:

$$Gen_Next_Config \begin{pmatrix} \chi_a^\bullet & \chi_b^\bullet \end{pmatrix} = \begin{pmatrix} \phi_{1s}^\bullet & \phi_{2s}^\circ & \phi_{3s}^\bullet & \phi_{4s}^\circ \end{pmatrix} \begin{pmatrix} 1 & 0 \\ z_{31}^f & z_{32}^f \\ 0 & 1 \\ z_{41}^f & z_{42}^f \end{pmatrix}_{no}. \quad (5.43)$$

For the presented particular case we do not need the transformation matrix W to go to an orthogonal MSO basis as the final fragments are atomic (the raw

atomic basis is orthogonal in atomic fragments). The expansion of $|z\rangle$ in terms of determinants is given by

$$\begin{aligned}
|z\rangle &= \langle\phi_{1s}\phi_{3s}|z\rangle|\phi_{1s}\phi_{3s}\rangle + \langle\phi_{1s}\phi_{2s}|z\rangle|\phi_{1s}\phi_{2s}\rangle + \langle\phi_{3s}\phi_{4s}|z\rangle|\phi_{3s}\phi_{4s}\rangle \\
&+ \langle\phi_{1s}\phi_{4s}|z\rangle|\phi_{1s}\phi_{4s}\rangle + \langle\phi_{2s}\phi_{3s}|z\rangle|\phi_{2s}\phi_{3s}\rangle \\
&+ \langle\phi_{2s}\phi_{4s}|z\rangle|\phi_{2s}\phi_{4s}\rangle, \tag{5.44}
\end{aligned}$$

which, when evaluated reduces to

$$\begin{aligned}
|z^f\rangle &= |\phi_{1s}\phi_{3s}\rangle + z_{32}^f|\phi_{1s}\phi_{2s}\rangle - z_{41}^f|\phi_{3s}\phi_{4s}\rangle \\
&+ z_{42}^f|\phi_{1s}\phi_{4s}\rangle + z_{31}^f|\phi_{2s}\phi_{3s}\rangle + (z_{31}^f z_{42}^f - z_{32}^f z_{41}^f)|\phi_{2s}\phi_{4s}\rangle. \tag{5.45}
\end{aligned}$$

The determinantal states of expansion 5.45 can be classified according to the charge configuration and degree of excitation they represent. Configurations $|\phi_{1s}\phi_{3s}\rangle$ and $|\phi_{2s}\phi_{4s}\rangle$ represent the neutral channels $H+H \rightarrow H+H$ and $H+H \rightarrow H^*+H^*$ respectively (H^* refers to an excited state of atomic hydrogen). There is a total of four neutral configurations on expansion 5.45.

Configurations $|\phi_{1s}\phi_{2s}\rangle$ and $|\phi_{3s}\phi_{4s}\rangle$ represent the same charge transfer channel $H+H \rightarrow H^+ + H^-$.

We can calculate the probability of the charge transfer channel for an individual trajectory by summing the squares of the amplitudes referring to configurations $|\phi_{1s}\phi_{2s}\rangle$ and $|\phi_{3s}\phi_{4s}\rangle$ in Equation 5.45 by using 5.37.

The probability for a charge transfer channel is (dropping the superscript f)

$$P_{ct} = \frac{(|z_{32}|^2 + |z_{41}|^2)}{(\mathbf{I}^\bullet + \mathbf{z}^\dagger \mathbf{z})}. \tag{5.46}$$

Analogously the cumulative probability to find the system in any excited state is

$$P_{ex} = \frac{(|z_{42}|^2 + |z_{31}|^2 + |z_{31}z_{42} - z_{32}z_{41}|^2)}{(\mathbf{I}^\bullet + \mathbf{z}^\dagger \mathbf{z})}. \tag{5.47}$$

The procedure for calculating probabilities by summing projections on a family of states with desired charge or spin for a general system is in all ways similar to what we just developed in this section. The only difference being that in a general case we need a MSO basis to generate the expansion given by 5.40.

The procedures to generate all relevant configurations and to compute probabilities for all possible charge transfer channels for an arbitrary system is implemented in a computer code as an extension to the program EVOLVE. EVOLVE is an auxiliary program to ENDyne that has as its main focus to extract and manipulate quantities computed by ENDyne during the time evolution. Details of the current implementation are presented on the following section.

5.4 Implementation

5.4.1 Design

In this section we describe the details of the current implementation of the computer code used to calculate projections over determinants using a Hartree-Fock MSO basis of an arbitrary END single determinantal wave function.

The unified modeling language (UML) [104, 105] has been used in figure 5.1 to give a pictorial representation of the code's structure and functionality. UML is mostly a notation language used for modeling systems using object oriented concepts. Figure 5.1 is an example of a class diagram. Class diagrams are best suited to describe the structure and concepts of a software package.

Each UML class has attributes and methods. Attributes are an abstract generalization of class data while methods are an abstraction to class member functions. Member functions among other things can operate on class data and are usually the only functions allowed to change class attributes. UML syntax allows for the inclusion of an arbitrary set of member functions actually present in the code. We

have used this flexibility and the member functions mentioned in figure 5.1 are not a representation of the whole set of functions in the code. In the following paragraphs we give a brief description of the most important member functions.

Without getting too much into the details of the UML language, there is a lot of information one can obtain from figure 5.1. Foremost in figure 5.1 one finds three classes: `basis`, `cluster` and a template class `Gen_Config`. The `cluster` class has a dependency on the `basis` class through the `overlap` attribute. Configuration generation classes share a great deal of code through similar methods, so they inherit from the template class `Gen_Config`. This is true for the classes responsible for the generation of the charge, spin and excitation configurations namely `Charge_State`, `Spin_State` and `Config_State`. The `Charge_State` class also contains (aggregates) a `cluster` class.

The classes `Charge_State`, `Spin_State` and `Config_State` are related through a generalization concept with `Charge_State` being the most general. This hierarchy has a physical counterpart as we specify a fragment configuration by specifying the number of electrons per fragment, the fragment spin and the excitation configuration in a fragment in that order. It also suggests that the order for generating configurations follow a sequence. First we generate a charge state by assigning electrons to fragments, then for that charge state we generate all possible spin states and for each spin state we consider all possible excitation configurations.

`SD_State` is a class that specifies a single determinantal state and aggregates several classes pictured in figure 5.1, namely classes `basis`, `Charge_State`, `Spin_State` and `Config_State`. As a practical illustration of class instantiation consider a SCF state for the whole system. This state would be specified with all centers belonging to a fragment and with this single fragment having canonical configurations for spin and excitation configuration (canonical occupation and low spin configuration).

The class responsible for the actual computation of the projections is the Product class. The Product class can have a 2 to 1 composition relation to the SD_State class. This 2 to 1 relationship relates to the definition of a product between two states and is natural to the problem. When used to compute projections over classes of states the Product class has a one-to-many composition relation with the SD_Class. This is the class we use when computing charge transfer probabilities.

5.4.2 Algorithms

The last section discussed the code organization and relationships of code elements. In this section I will outline the algorithms used for the member functions discussed in the last section.

We make use of another kind of diagram of the UML language: the interaction diagram. Interaction diagrams are used to depict the flow of messages between object for a single, usually typical, use of the program.

The SD_State class contains several member functions. A few functions have implementations that are trivial translations of equations presented in this chapter. More explicitly Orth_Sim and Orth_HF implement a basis set transformation for the atomic \mathbf{z} coefficients with the transformation \mathbf{W} in Equations 5.28 and 5.34 corresponding to Löwdin ($\mathbf{U} = \mathbf{I}$) and canonical Hartree-Fock respectively. In the current implementation the dynamical projected Fock operator is diagonalized to obtain the \mathbf{W} transformation. The modulus function implements Equation 5.37 for the case where $|\Psi_2\rangle = |\Psi_1\rangle$.

The cluster class has a Find_Cluster member function. This function is responsible for, given an overlap matrix, finding the fragment structure for a given nuclear arrangement. Special care was taken to develop an algorithm that maintains

a fragment assignment for each nucleus as continuous as possible. The algorithm assigns nuclei to fragments in a self-consistent manner and takes into account the previous fragment assignment. Changes are made to the prior assignment only for the nuclei that change fragments or are moved away from their previously assigned fragment. Continuous fragment assignment is important for interpretation purposes as it makes the differentiation of rearrangements and reactions clear.

The template class `Gen_Config` has three member functions, namely `Gen_Init_State`, `Gen_Final_State`, `Gen_Next_Config`. `Gen_Init_State` and `Gen_Final_State` generates the initial and final configurations used in the sum of expansion 5.40. A restricted set of ordered configurations can be generated by starting and ending at arbitrary configurations. The generation of the initial and final configurations follows heuristic rules and depends on what kind of configuration is being generated. For class `Charge_State` implementation the initial and final configurations are controlled by two input parameters: `NMEL`, the number of electrons allowed to move between fragments, and `MXCHRG`, the maximum negative charge allowed per fragment. `Spin_State` has a similar implementation with the difference that the generation of initial and final states is constrained by the maximum S_z allowed per fragment. Finally `Config_State` final configuration generation is constrained by an excitation level parameter `NEX`.

`Gen_Next_Config` is at the heart of the functionality of the configuration generation classes and is responsible for generating the next valid configuration of either charge, spin or excitation in lexicographical order. If the last configuration is given, `Gen_Next_Config` returns the initial configuration. The algorithm used by all `Gen_Next_Config` implements a combinatorial generation of all $\binom{M}{P}$ configurations for a combination of M items over P containers. In all cases a string of numbers defining a map labels a configuration.

In the case of the charge, the string of numbers contains an electron fragment map (regardless of the spin) with the initial configuration having most electrons on the largest (highest atomic number) fragment. Subsequent configurations are generated by “moving” electrons to other fragments ordered by atomic charge. The last configuration is reached when the last fragment reaches the maximum number of electrons allowed by the input parameters MXCHRG.

For the spin state a string in Gen_Next_Config contains an alpha or beta electron fragment map. In this case the initial configuration has an alpha or beta electron excess equal to the input parameter defining the maximum S_z on the largest fragment. Subsequent configurations are generated by “moving” electrons of a certain spin over to other fragments ordered by atomic charge. The last configuration is reached when the last fragment reaches the maximum allowed spin S_z .

An overview of the algorithm for charge and spin configuration generation is given in figure 5.2.

Figure 5.2 should be read as

1. Create a base configuration. This assigns the non dynamical electrons.
2. Create the first and last configurations.
3. Call the subsequent (lower rank) configuration generation method, i.e., the charge configuration method would call the spin configuration method, with a valid configuration, and so on.
4. When the lower rank configuration generation method returns with a probability, generate a new configuration.

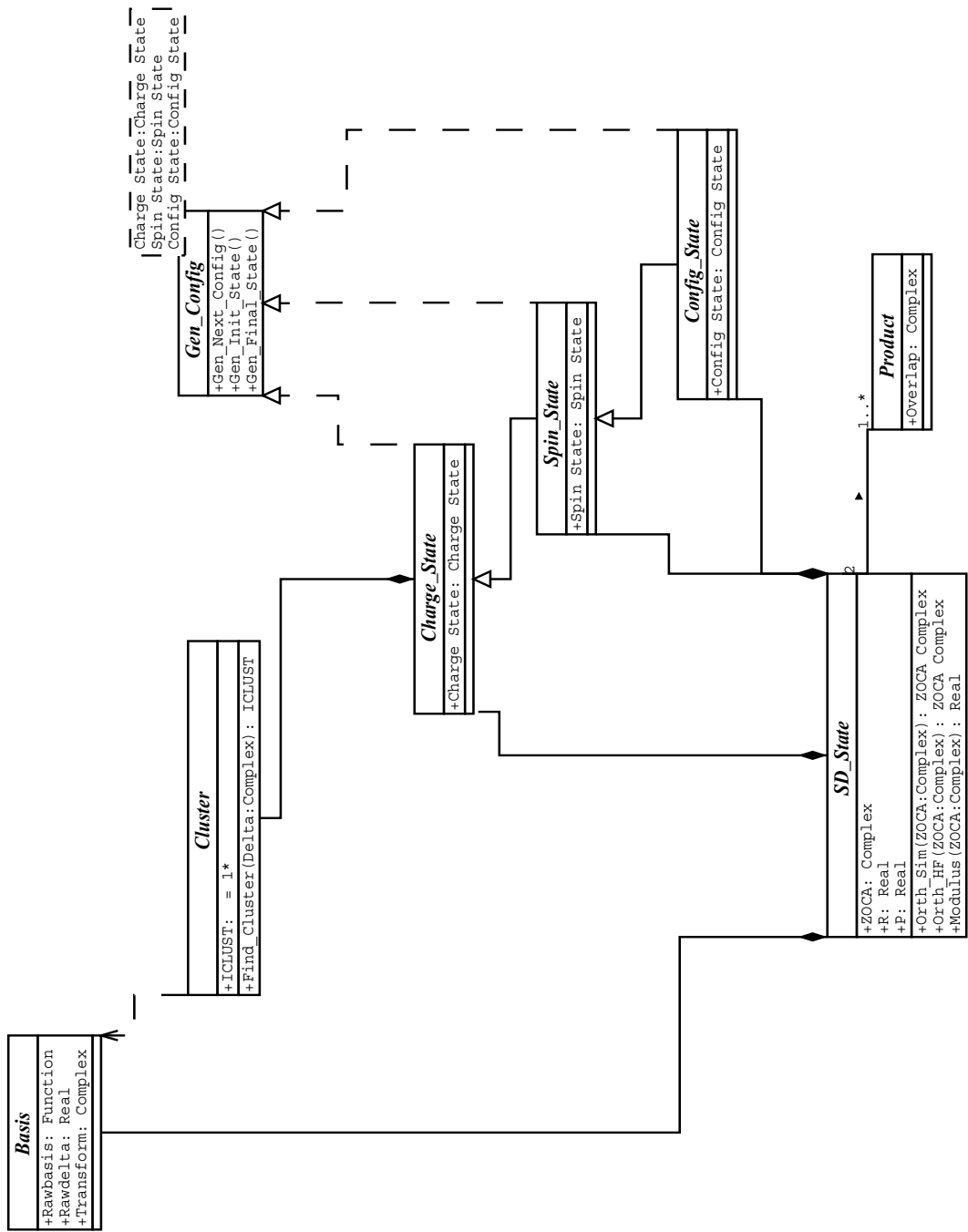


Figure 5.1: Class diagram for the project code.

The algorithm stops when we reach the last configuration. Note that steps 1 and 2 use heuristic rules based on input parameters. The algorithm for generating excitation configurations over an unrestricted spin determinant is a little more involved. An overview of the algorithm is given in figure 5.3.

Figure 5.3 should be read as

1. Create a base configuration. This assigns the non dynamical electrons.
2. Create a valid configuration for beta spin electrons.
3. For the beta configuration generate the overlap matrix and its determinant. See Equation 5.37 with S defined by Equation 5.39.
4. Create a valid configuration for alpha spin electrons.
5. For the alpha configuration generate the overlap matrix and its determinant.
6. Square amplitudes and add to the probability.
7. Generate next alpha configuration.

The excitations are generated by fragments and the algorithm only terminates when all excitations over all fragments are generated.

A description of the excitation algorithm has been given below for the case of two fragments and only one spin type:

1. From base configuration excite first fragment.
2. Excite second fragment over all possible internal (to the fragment) excitations.
3. Excite first fragment by one excitation.
4. Excite fragment two over all possible excitations.
5. ... and so on until the first fragment exhaust the allowed excitations.

The excitations in each fragment are generated with a combinatorial algorithm similar to the one used for generating charge and spin configurations. In this case M is the number of electrons and P is the number of orbitals in the fragment.

The generalization of the previous algorithm for a general alpha-beta configuration is not hard and has been implemented. One only needs to consider that for each excitation configuration of one kind (beta/alpha), all possible excitation configurations for the other kind (alpha/beta) are generated.

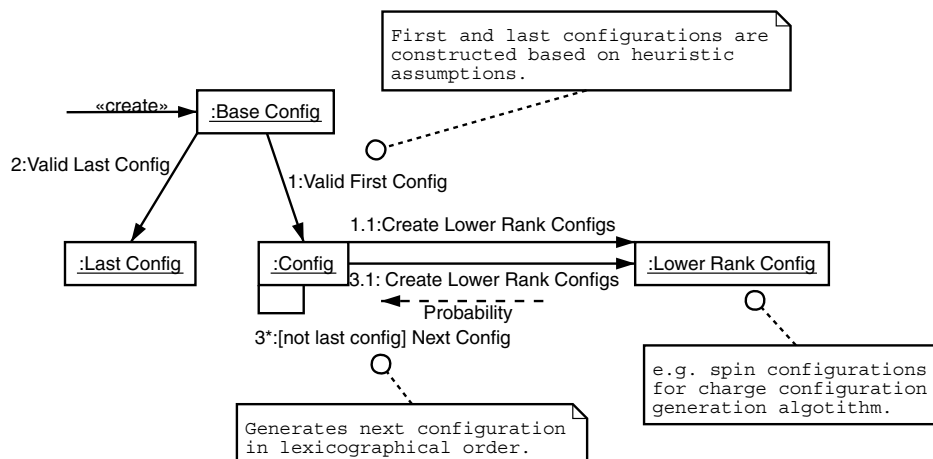


Figure 5.2: Configuration generation algorithm for spin and charge.

5.4.3 Numerical Examples

In this section we demonstrate in detail an application of the algorithms implemented to the $He^{++} + Ne$ collision system. The $He^+ + Ne$ system was investigated by Cabrera-Trujillo [106]. Total as well as charge transfer cross section were calculated. Because of the uncertainty related to the initial charge of the projectile ion (He^0 and He^+ also occur on the incoming beam) direct comparison with experimental results for stopping cross section was not possible.

Calculation of charge transfer transfer cross section for alternative charge transfer channels originating from the projectiles He^0 and He^{++} require the use of a more general scheme for the calculation of transfer probabilities. For example, Mulliken population analysis does not allow for a separation of the one and two electron transfer probabilities for the charge transfer reaction $He^{++} + Ne$.

In Figure 5.4 we present the output of a final state analysis calculation for the $He^{++} + Ne$ system at a collision energy of 1 KeV/amu using an impact parameter of 1.0 a.u. The output reflects the code structure outlined in 5.1. The output is organized per fragment, with charge, excess alpha electrons (defined as $N^\alpha - N^\beta$), and multiplicity calculated per fragment for each configuration generated.

For this calculation we considered up to quadruple excitations. It lasted about 90 seconds on a Ultra SPARC 5. This amounts for a substantial savings (> 500) when compared to a cruder implementation that did not consider excitation restriction.

The first fragment picked by the program is the Ne atom while the second is the He atom. We asked for all configurations up to charge of ± 3 and a maximum S^2 of 3. The first configuration considered is the no transfer channel, i.e., with charge plus 2 on the He and it has a weight of 0.51229 on the final END wavefunction. This is equivalent to the no-transfer probability for this particular trajectory. The program generates all other configurations according to the input parameters. The second most important channel is the one electron charge transfer channel, with a probability of $2 \times 0.19160 = 0.3832$ of occurring. The two electron charge transfer channel has a probability of only 0.092273 of occurring, with an even smaller contribution coming from the three electron charge transfer channel. The completeness of the states considered for the projection calculations can be evaluated by the total sum of probabilities, which in this case is 0.99552, very close to the maximum value of 1.

Next we considered a case with a much higher collision energy: 100 KeV/amu. The output of the program is given in Figure 5.5. As expected in order to get convergence for the total probability we need to include up to the 7th excitation degree on expansion 5.35. In this case the savings are not as dramatic but are still

substantial as convergence is archived at the 7th out of a total of 24 excitations allowed for the basis.

At this much higher collision energy the probability for the non transfer channel is much smaller, only around 10% or 0.10999. The interesting difference from the lower energy collision is that the one electron charge transfer channel stays around the same value, specifically at 0.39898, while the two electron charge transfer channel has a much larger contribution at 0.40436. These differences would not be apparent on a Mulliken population analysis. Again, the completeness of the states used on the projection calculation can be assured by the value for the final cumulative probability of 0.99136.

5.5 Conclusions

The final state analysis based on the procedure outlined in this chapter enables one to obtain information from the final dynamical state that can be useful for comparison with experiments. As demonstrated in Section 5.4.3 a much more detailed picture of charge transfer reactions can be obtained with the use of the scheme discussed in this chapter.

State to state probabilities can also be calculate by considering the proper electronic basis. If the transformation \mathbf{W} from Equation 5.33 is obtained from an SCF calculation then values for the projection from individual configurations can be useful for interpretation purposes. In this case the projection tools developed in this chapter can be used to, e.g., interpret photo-dissociation reactions or photo-induced electron transfer reactions by following important electronic configurations as the dynamics proceeds.

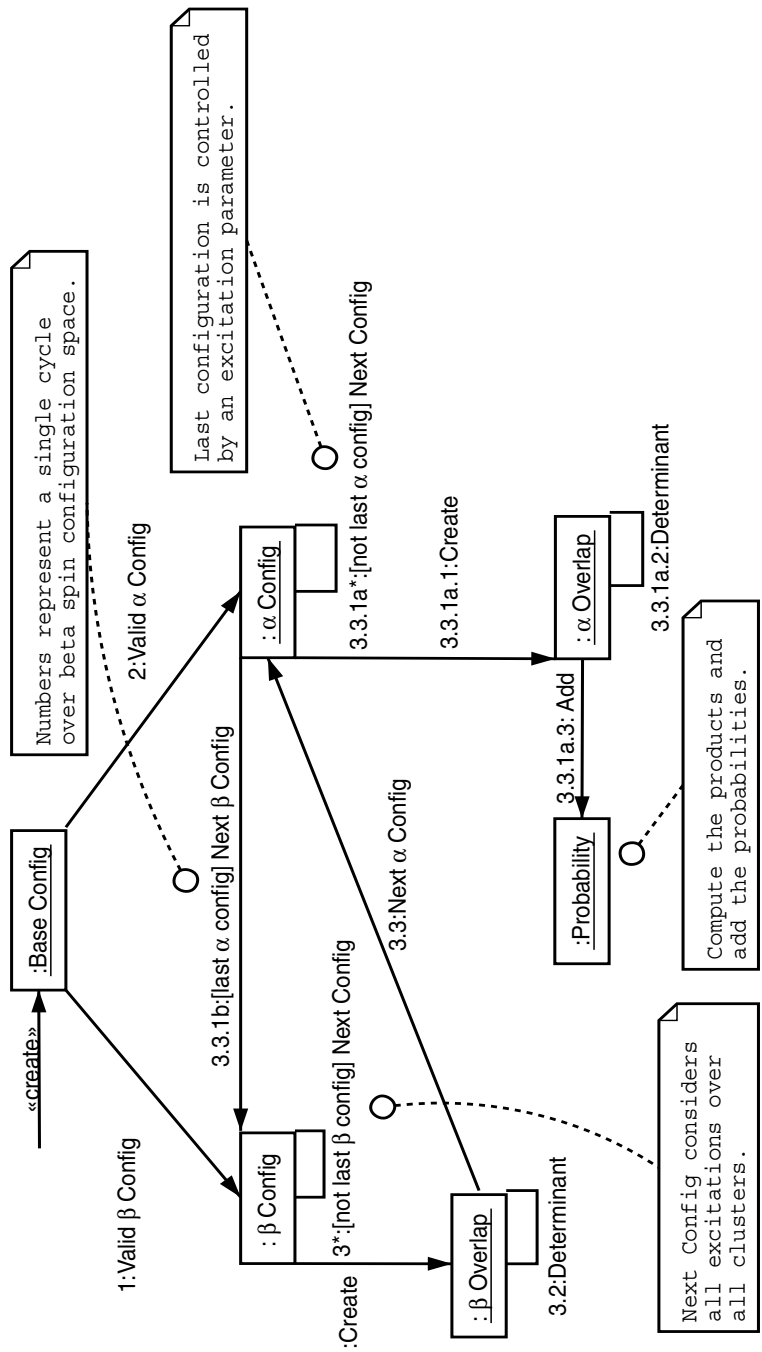


Figure 5.3: Configuration generation algorithm for excitations.

```

evolve> p 0.1 4 1 0 0 300 3
# Restart #
-----

@PROJDRV-I, Using input file endyne.inp
Fragment:          1          2
Charges:           0.0000000  2.0000000
Fragment:          1          2
Excess alfa:       0          0
Multiplicity:      1          1
Probability for the spin state:                                .51229D+00
-----
Probability for the charged state:                             .51229D+00
Cumulative probability:                                       .51229D+00
-----
Fragment:          1          2
Charges:           1.0000000  1.0000000
Fragment:          1          2
Excess alfa:       1          -1
Multiplicity:      2          2
Probability for the spin state:                                .19160D+00
-----
Fragment:          1          2
Excess alfa:      -1          1
Multiplicity:      2          2
Probability for the spin state:                                .19160D+00
-----
Probability for the charged state:                             .38321D+00
Cumulative probability:                                       .89550D+00
-----
Fragment:          1          2
Charges:           2.0000000  0.0000000
Fragment:          1          2
Excess alfa:       2          -2
Multiplicity:      3          3
Probability for the spin state:                                .10305D-01
-----
Fragment:          1          2
Excess alfa:       0          0
Multiplicity:      1          1
Probability for the spin state:                                .71662D-01
-----
Fragment:          1          2
Excess alfa:      -2          2
Multiplicity:      3          3
Probability for the spin state:                                .10305D-01
-----
Probability for the charged state:                             .92273D-01
Cumulative probability:                                       .98777D+00
-----

```

Figure 5.4: Project output for the $He^{++} + Ne$ system at a collision energy of 1 KeV/amu using an impact parameter of 1.0 a.u.

```

Fragment:          1          2
Charges:          3.0000000  -1.0000000
Fragment:          1          2
Excess alfa:      3          -3
Multiplicity:     4          4
Probability for the spin state:                                .19833D-04
-----
Fragment:          1          2
Excess alfa:      1          -1
Multiplicity:     2          2
Probability for the spin state:                                .38543D-02
-----
Fragment:          1          2
Excess alfa:     -1          1
Multiplicity:     2          2
Probability for the spin state:                                .38543D-02
-----
Fragment:          1          2
Excess alfa:     -3          3
Multiplicity:     4          4
Probability for the spin state:                                .19833D-04
-----
Probability for the charged sate:                              .77483D-02
Cumulative probability:                                       .99552D+00
-----
      0      48381
evolve>

```

Figure 5.4: continued.

```

evolve> p 0.1 7 1 0 30 30 3 2 2
# Restart #
-----

@PROJDRV-I, Using input file endyne.inp
Fragment:          1          2
Charges:           0.0000000  2.0000000
Fragment:          1          2
Excess alfa:       0          0
Multiplicity:      1          1
Probability for the spin state:                                .10999D+00
-----
Probability for the charged state:                             .10999D+00
Cumulative probability:                                       .10999D+00
-----
Fragment:          1          2
Charges:           1.0000000  1.0000000
Fragment:          1          2
Excess alfa:       1          -1
Multiplicity:      2          2
Probability for the spin state:                                .19949D+00
-----
Fragment:          1          2
Excess alfa:      -1          1
Multiplicity:      2          2
Probability for the spin state:                                .19949D+00
-----
Probability for the charged state:                             .39898D+00
Cumulative probability:                                       .50897D+00
-----
Fragment:          1          2
Charges:           2.0000000  0.0000000
Fragment:          1          2
Excess alfa:       2          -2
Multiplicity:      3          3
Probability for the spin state:                                .21284D-01
-----
Fragment:          1          2
Excess alfa:       0          0
Multiplicity:      1          1
Probability for the spin state:                                .36180D+00
-----
Fragment:          1          2
Excess alfa:      -2          2
Multiplicity:      3          3
Probability for the spin state:                                .21284D-01
-----
Probability for the charged state:                             .40436D+00
Cumulative probability:                                       .91334D+00
-----

```

Figure 5.5: Project output for the $He^{++} + Ne$ system at a collision energy of 100 KeV/amu using an impact parameter of 1.0 a.u.

Fragment:	1	2	
Charges:	3.0000000	-1.0000000	
Fragment:	1	2	
Excess alfa:	3	-3	
Multiplicity:	4	4	
Probability for the spin state:			.41331D-03

Fragment:	1	2	
Excess alfa:	1	-1	
Multiplicity:	2	2	
Probability for the spin state:			.38601D-01

Fragment:	1	2	
Excess alfa:	-1	1	
Multiplicity:	2	2	
Probability for the spin state:			.38601D-01

Fragment:	1	2	
Excess alfa:	-3	3	
Multiplicity:	4	4	
Probability for the spin state:			.41331D-03

Probability for the charged state:			.78029D-01
Cumulative probability:			.99136D+00

0	3534		

Figure 5.5: continued.

CHAPTER 6 CONCLUSION

The purpose of this work is to apply the minimal END method to areas in which its unique qualities can give new insight into the relevant dynamics of a chemical or physical process. Minimal END is a method for direct non adiabatic dynamics. It describes the electrons with a family of complex determinantal wave-functions in terms of non-orthogonal spin orbitals and treats the nuclei as classical particles.

In the first two studies, we apply the END method to hydrogen abstraction and exchange reactions at hyper-thermal collision energies. Hydrogen abstraction reactions are relatively simple and yet fundamental for detailed experimental investigations. From a theory perspective these reactions provide a wealth of information for testing methods and opportunities for aiding in the interpretation of results, when comparisons to experiment are appropriate. We investigate the $D_2 + NH_3^+$ reaction at collision energies ranging from 6 to 16 eV and the $H + HOD$ reaction at a collision energy of 1.575 eV. Collision energies refer to center of mass energies. Emphasis is put on the details of the abstraction and exchange reaction mechanisms for ground state reactants.

In the $D_2 + NH_3^+$ reaction our calculations suggests a mechanism that explains the apparent discordant experimental findings by Eisele [46], Winniczek [47], Zare [44] and Morisson at al. [45]. A complex two step mechanism with a dissociative step forming the exchange product NH_2D^+ is observed along with a direct exchange mechanism for the collision energies studied. Also, our calculations estimate the collision energy necessary for the opening of the dissociative channel.

We found that non-adiabatic effects are important for the correct description of dynamics for this system at the collision energies considered.

The cross section ratio $\frac{\sigma_{OD}}{\sigma_{OH}}$ results for the $H + HOD$ reaction with the ground state reactant reproduced the anisotropy found in the reactivity between the OD and OH bonds at the minimal basis level. However, when starting with HOD in a vibrationally excited state our results overestimate the absolute cross sections and failed to show the experimental cross section enhancement with vibrational excitation. As we did not observe non-adiabatic effects present in the dynamics, the overestimation of the HOD reactivity is the result of an incorrect description of the ground state potential. An attempt to improve the basis was successful in reproducing several quantitative features of high quality potentials used for dynamics of the $H + HOD$ reaction. However, the resulting Hartree-Fock potential produced with the optimized basis exhibit an inaccessible transition state for the energy considered. Correlation effects are believed to be important for the correct description of the topology of the potential. An extension of the END formalism with a multi-reference wavefunction would enhance the description of the ground electronic state necessary for the correct description of the dynamics on this system.

In a final application we use minimal END to study the interaction of a strong laser field with diatomic molecules, namely HF and LiH . Effects of the polarization of the electronic potential on the dynamics are investigated. Our results indicate that for the range of intensities considered the electronic polarization effect with the field is very important for the correct description of the dynamics. Non-adiabatic effects were found not to be important for the conditions considered. The polarization effects are more pronounced for the HF molecule than for LiH . Further applications of the NPMD method on larger system with large polarizabilities, e.g. 6-amino-nitrohexene-1,3,5-triene, can reveal interesting new non-linear

absorption behaviors. The interplay between nuclear degrees of freedom and the electronic polarizability in more complex systems can reveal even more important effects of the correct description of the electronic polarization for energy absorption under strong field conditions.

In the last chapter we present a method to extract information from the final END dynamical state. The method generalizes the concept of Mulliken population for the calculation charge transfer probabilities. The algorithms used in the calculations are outlined and their implementation discussed. The procedure can also be used for analyzing the electronic states that participate in the electronic dynamics. This new capability can be useful, e.g. for investigating the effect of excited states on the reactivity of photo induced reactions.

The END method in its present form proved to be very useful for the description of physical processes ranging from reactive scattering to laser-molecule interaction. The ability to tackle such a diverse set of problems is a consequence of the flexibility of the theoretical framework used in the derivation of the END equations of motion. Particularly the method (i) does not use stationary electronic states (PES) and (ii) treats electrons and nuclei on the same footing with the correct description of electron-nuclear couplings. The difficulties presented in the description of the $H + HOD$ reaction are a limitation of the present END implementation. Further development should improve the description of the wavefunction through the use of a multi-reference states and quantum description of the nuclei.

REFERENCES

- [1] J. Linderberg and Y. Öhrn, *Propagators in Quantum Chemistry* (Academic, New York, 1973).
- [2] M. Born and R. Oppenheimer, *Ann. d. Phys.* **84**, 457 (1927).
- [3] M. Born and K. Huang, *Dynamical Theory of Crystal Lattices* (Clarendon Press, Oxford, 1954).
- [4] J. C. Tully, in *Dynamics of Molecular Collisions* (Plenum, New York, 1976), Chap. 5, pp. 217–267.
- [5] M. Baer, in *State to State and State Selected Ion Molecular Dynamics* (Wiley, New York, 1992), Vol. LXXXII, Chap. 4.
- [6] V. Sidis, in *State to State and State Selected Ion Molecular Dynamics* (Wiley, New York, 1992), Vol. LXXXII, Chap. 2.
- [7] M. Kimura and W. R. Thorson, *Phys. Rev. A* **24**, 1780 (1981).
- [8] M. Kimura and N. F. Lane, in *Advances in Atomic, Molecular and Optical Physics*, edited by D. Bates and B. Bederson (Academic, New York, 1990), p. 79.
- [9] N. F. Mott, *Proc. Cambridge. Philos. Soc.* **27**, 553 (1931).
- [10] J. C. Tully and R. K. Preston, *J. Chem. Phys.* **55**, 562 (1971).
- [11] S. Chapman, in *State to State and State Selected Ion Molecular Dynamics* (Wiley, New York, 1992), Vol. LXXXII, Chap. 7.
- [12] R. Car and M. Parrinello, *Phys. Rev. Lett.* **55**, 2471 (1985).
- [13] R. G. Parr and W. Yang, *Density-Functional Theory of Atoms and Molecules, International Series of Monographs on Chemistry* (Oxford University Press, Clarendon Press, New York, Oxford, 1989).
- [14] S. Kirkpatrick, C. D. Gelatt Jr., and M. V. Vecchi, *Science* **220**, 617 (1983).
- [15] E. Deumens and Y. Öhrn, *Int. J. Quant. Chem.: Quant. Chem. Symp.* **23**, 31 (1989).

- [16] P. A. M. Dirac, Proc. Cambridge Philos. Soc. **26**, 376 (1930).
- [17] K. R. S. Devi and S. E. Koonin, Phys. Rev. Lett. **47**, 27 (1981).
- [18] K. C. Kulander, K. R. S. Devi, and S. E. Koonin, Phys. Rev. A **25**, 2968 (1982).
- [19] E. Deumens, B. Weiner, and Y. Öhrn, Nucl. Phys. **A466**, 85 (1987).
- [20] E. Deumens and Y. Öhrn, J. Phys. Chem. **92**, 3181 (1988).
- [21] E. Deumens and Y. Öhrn, J. Mol. Struct. (THEOCHEM) **199**, 23 (1989).
- [22] M. J. Field, J. Chem. Phys. **96**, 4583 (1992).
- [23] K. Runge, D. A. Micha, and E. Q. Feng, Int. J. Quantum Chem.: Quant. Chem. Symp. **24**, 781 (1990).
- [24] P. Kramer and M. Saraceno, *Geometry of the Time-Dependent Variational Principle in Quantum Mechanics* (Springer, New York, 1981).
- [25] E. Deumens, A. Diz, R. Longo, and Y. Öhrn, Rev. Mod. Phys **66**, 917 (1994).
- [26] E. Deumens and Y. Öhrn, J. Chem. Soc., Faraday Trans. **93**, 919 (1997).
- [27] Y. Öhrn and E. Deumens, J. Phys. Chem. **103**, 9545 (1999).
- [28] P. A. M. Dirac, *The Principles of Quantum Mechanics*, No. 27 in *The International Series of Monographs on Physics* (Oxford University Press, ADDRESS, 1930).
- [29] R. Longo, A. Diz, E. Deumens, and Y. Öhrn, Chem. Phys. Lett. **220**, 305 (1994).
- [30] E. J. Heller, J. Chem. Phys. **62**, 1544 (1975).
- [31] E. J. Heller, Acc. Chem. Res. **14**, 386 (1981).
- [32] L. I. Schiff, Phys. Rev. **103**, 443 (1956).
- [33] R. Cabrera-Trujillo, J. R. Sabin, Y. Öhrn, and E. Deumens, Phys. Rev. A **61**, 032719 1 (2000).
- [34] M. V. Berry, Proc. Phys. Soc. (London) **89**, 479 (1966).

- [35] J. A. Morales, A. C. Diz, E. Deumens, and Y. Öhrn, *J. Chem. Phys.* **103**, 9968 (1995).
- [36] M. Hedström, J. A. Morales, E. Deumens, and Y. Öhrn, *Chem. Phys. Lett.* **279**, 241 (1997).
- [37] H. Goldstein, *Classical Mechanics*, 2nd ed. (Addison-Wesley, Reading, MA, 1980).
- [38] M. S. Child, *Molecular Collision Theory* (Academic Press, London and New York, 1974).
- [39] C. Cohen-Tannoudji, B. Diu, and F. Laloë, *Quantum Mechanics* (Wiley Interscience, New York, 1977), Vol. 1.
- [40] S. L. Anderson, F. A. Houle, D. Gerlich, and Y. T. Lee, *J. Chem. Phys.* **75**, 2153 (1981).
- [41] R. A. Dresseler, R. H. Salter, and E. Murad, *J. Chem. Phys.* **99**, 1159 (1993).
- [42] R. A. Dresseler and E. Murad, in *Unimolecular and Bimolecular Ion-Molecule Reaction Dynamics* (Wiley, New York, 1994), Chap. 8.
- [43] R. D. Levine and R. B. Bernstein, *Molecular Reaction Dynamics and Chemical Reactivity* (Oxford University, New York, 1987).
- [44] J. C. Poutsma, M. A. Everest, J. E. Flad, G. C. Jones Jr., and R. N. Zare, *Chem. Phys. Lett.* **305**, 343 (1999).
- [45] R. J. S. Morisson, W. E. Conaway, T. Ebata, and R. N. Zare, *J. Chem. Phys.* **84**, 5527 (1986).
- [46] G. Eisele, A. Henglein, P. Botschwina, and W. Meyer, *Ber. Bunsenges. Phys. Chem.* **78**, 1090 (1974).
- [47] J. W. Winniczek, A. L. Braveman, M. H. Shen, S. G. Kelley, and J. M. Farrar, *J. Chem. Phys.* **86**, 2818 (1986).
- [48] J. Ischtwan, B. J. Smith, M. A. Collins, and L. Radom, *J. Chem. Phys.* **97**, 1191 (1992).
- [49] J. Ischtwan and M. A. Collins, *J. Chem. Phys.* **94**, 7084 (1991).
- [50] P. R. Kemper and M. T. Bowers, *J. Phys. Chem.* **90**, 477 (1986).

- [51] F. C. Fehsenfeld, W. Lindinger, A. L. Schmeltekopf, D. L. Albritton, and E. E. Ferguson, *J. Chem. Phys.* **62**, 2001 (1975).
- [52] O. P. Bugaets and D. A. Zhogolev, *Chem. Phys. Lett.* **45**, 462 (1977).
- [53] E. Kassab, J. Fouquet, and E. M. Evleth, *Chem. Phys. Lett.* **153**, 522 (1988).
- [54] R. J. S. Morrison, W. E. Conway, T. Ebata, and R. N. Zare, *J. Chem. Phys.* **84**, 5527 (1986).
- [55] J. C. Poutsma, M. A. Everest, J. E. Flad, G. C. Jones Jr., and R. N. Zare, *Chem. Phys. Lett.* **305**, 343 (1999).
- [56] M. J. Bronikowski, W. R. Simpson, B. Girard, and R. N. Zare, *J. Chem. Phys.* **95**, 8647 (1991).
- [57] M. J. Bronikowski, W. R. Simpson, and R. N. Zare, *J. Phys. Chem.* **97**, 2194 (1993).
- [58] M. J. Bronikowski, W. R. Simpson, and R. N. Zare, *J. Phys. Chem.* **97**, 2204 (1993).
- [59] A. Sinha, M. C. Hsiao, and F. F. Crim, *J. Chem. Phys.* **94**, 4928 (1991).
- [60] R. B. Metz, J. D. Thoemke, J. M. Pfeiffer, and F. F. Crim, *J. Chem. Phys.* **99**, 1744 (1993).
- [61] K. Kessler and K. Kleinermanns, *Chem. Phys. Lett.* **190**, 145 (1992).
- [62] H. Elgersma and G. C. Schatz, *Intern. J. Quantum Chem.* **S15**, 611 (1981).
- [63] S. P. Walch and T. H. Dunning, *J. Chem. Phys.* **72**, 1303 (1980).
- [64] G. C. Schatz, M. C. Colton, and J. L. Grant, *J. Chem. Phys.* **88**, 2971 (1984).
- [65] D. H. Zhang and J. C. Light, *J. Chem. Phys.* **93**, 691 (1997).
- [66] D. Wang and J. M. Bowman, *J. Chem. Phys.* **98**, 6235 (1993).
- [67] D. C. Clary, *Chem. Phys. Lett.* **192**, 34 (1992).
- [68] M. Hedström, E. Deumens, and Y. Öhrn, *Phys. Rev. A* **57**, 2625 (1998).
- [69] R. M. Porter and L. M. Raff, in *Molecular Collisions*, edited by R. B. Bernstein (Plenum, New York, 1976).

- [70] L. M. Raff and D. L. Thompson, in *The Theory of Chemical Reaction Dynamics*, edited by M. Baer (CRC, Boca Raton, FL, 1985), pp. 1–121.
- [71] R. L. Vander Wal, J. L. Scott, and F. F. Crim, *J. Chem. Phys.* **94**, 3548 (1991).
- [72] D. F. Plusquellic, O. Votava, and D. Nesbitt, *J. Chem. Phys.* **109**, 6631 (1998).
- [73] A. Szabo and N. S. Ostlund, *Modern Quantum Chemistry. Introduction to Advanced Electronic Structure Theory* (McGraw-Hill, New York, 1989).
- [74] K. Kudla and G. C. Schatz, *Chem. Phys. Lett.* **193**, 507 (1992).
- [75] R. A. Brownsword, M. Hillenkamp, T. Laurent, R. K. Vatsa, H. Volpand, and J. Wolfrum, *Chem. Phys. Lett.* **259**, 375 (1996).
- [76] A. D. Isaacson, *J. Chem. Phys.* **107**, 3832 (1997).
- [77] G. O. de Aspuru and D. C. Clary, *J. Phys. Chem. A* **102**, 9631 (1998).
- [78] M. W. Schmidt, K. K. Baldridge, J. A. Boatz, J. H. Jensen, S. Koseki, M. S. Gordon, K. A. Nguyen, T. L. Windus, and S. T. Elbert, *QCPE Bulletin* **10**, 52 (1990).
- [79] R. B. Walker and R. K. Preston, *J. Chem. Phys.* **67**, 2017 (1977).
- [80] P. S. Dardi and S. K. Gray, *J. Chem. Phys.* **77**, 1345 (1982).
- [81] J. Broeckhove, B. Feynen, and P. Van Leuven, *Int. J. Quantum Chem.* **26**, 435 (1992).
- [82] R. Marquardt and M. Quack, *J. Chem. Phys.* **90**, 6320 (1989).
- [83] F. J. Lin and J. T. Muckerman, *Comp. Phys. Comm.* **63**, 538 (1991).
- [84] J. R. Stine and D. W. Noid, *Opt. Comm.* **31**, 161 (1979).
- [85] G. Jolicard and G. D. Billing, *J. Chem. Phys.* **90**, 346 (1989).
- [86] A. Guldberg and G. D. Billing, *Chem. Phys. Lett.* **186**, 229 (1991).
- [87] S. Chelkowski, A. D. Bandrauk, and P. B. Corkum, *Phys. Rev. Lett.* **65**, 2355 (1990).
- [88] B. G. Dibble and R. B. Shirts, *J. Chem. Phys.* **94**, 3451 (1991).

- [89] M. Kaluza, J. T. Muckerman, P. Gross, and H. Rabitz, *J. Chem. Phys.* **100**, 4211 (1994).
- [90] A. Bastida and F. X. Gadéa, *Z. Physik D* **39**, 325 (1997).
- [91] R. J. Glauber, *Phys. Rev. Lett.* **10**, 84 (1963).
- [92] Y. Öhrn, J. Oreiro, and E. Deumens, *Int. J. Quantum Chem.* **58**, 583 (1996).
- [93] W. T. Zemke, W. C. Stwalley, S. R. Langhoff, G. L. V. aldemara, and M. Berry, *J. Chem. Phys.* **95**, 7846 (1991).
- [94] A. Butalib and F. X. Gadéa, *J. Chem. Phys.* **97**, 1144 (1992).
- [95] B. R. Johnson, *J. Chem. Phys.* **67**, 4086 (1977).
- [96] J. Lin, P. Jones, J. Guckert, and E. I. Solomon, *J. Am. Chem. Soc.* **113**, 8312 (1991).
- [97] M. E. Goggin and P. W. Milonni, *Phys. Rev. A* **37**, 796 (1988).
- [98] H. Sekino and R. J. Bartlett, *J. Chem. Phys.* **84**, 2726 (1986).
- [99] L. D. Landau and E. M. Lifshitz, *Mechanics* (Pergamon, New York, 1976).
- [100] A. D. Hammerich, R. Kosloff, and M. A. Ratner, *J. Chem. Phys.* **97**, 6410 (1992).
- [101] M. Perisco and P. V. Leuven, *Phys. Rev. A* **53**, 366 (1995).
- [102] A. Blass, E. Deumens, and Y. Öhrn, *J. Chem. Phys.* **115**, 8366 (2001).
- [103] D. J. Thouless, *Nucl. Phys.* **21**, 225 (1960).
- [104] G. Booch, I. Jacobson, and J. Rumbaugh, *The UML Specification Documents* (Rational Software Corporation, Palo Alto, 1997).
- [105] C. Larman, *Applying UML and Patterns* (Prentice Hall, New York, 1998).
- [106] R. Cabrera-Trujillo, J. R. Sabin, E. Deumens, and Y. Ö. n, in *Application of Accelerators in Research and Industry, Sixteen th International Conference*, edited by J. L. Duggan and I. L. Morgan (American Institute of Physics, ADDRESS, 2001), p. 3.

BIOGRAPHICAL SKETCH

Maurício Domingues Coutinho Neto was born in Recife (the capital city of the state of Pernambuco, Brazil) on January 18, 1970. He is the son of Maurício D. Coutinho Filho, a physicist; and Maria da Conceição D. P. de Lyra, a psychologist. When he was four he quickly picked up interest in a human anatomy book from his mother's library. His parents were sure he was going for a career in biology. However, the search for a more universal source of knowledge brought him to a career in physical chemistry.

As an undergraduate student Maurício D. Coutinho Neto received a scientific fellowship for QSAR drug design study in the chemistry department at the Universidade Federal de Pernambuco (UFPE). After graduating, he enrolled in the masters program in the Chemistry department at UFPE and continued and continued his studies in theoretical chemistry. His master's thesis was concerned with matrix element calculation for electron transfer reactions.

After getting his master's degree, he was granted a fellowship from the Coordenadoria de Aperfeiçoamento de Pessoal de Nível Superior (CAPES) in 1995 to come to the Quantum Theory Project at The University of Florida. Later that year he joined the Öhrn-Deumens group and started his research working on the electron nuclear dynamics method.